DESIGN OF OUTRUNNER ELECTRIC MACHINES FOR GREEN ENERGY APPLICATIONS

A Dissertation

by

BAHAREH ANVARI ROSTAMKOLAEI

Submitted to the Office of Graduate and Professional Studies of
Texas A&M University
in partial fulfillment of the requirements for the degree of

DOCTOR OF PHILOSOPHY

Chair of Committee,	Hamid A. Toliyat
Committee Members,	Prasad Enjeti
	Shankar P. Bhattacharyya
	Alan B. Palazzolo
Head of Department,	Miroslav M. Begovic

December 2017

Major Subject: Electrical Engineering

ABSTRACT

Interests in using rare-earth free motors such as switched reluctance motors (SRMs) for electric and hybrid electric vehicles (EV/HEVs) continue to gain popularity, owing to their low cost and robustness. Optimal design of an SRM, to meet specific characteristics for an application, should involve simultaneous optimization of the motor geometry and control in order to achieve the highest performance with the lowest cost. This dissertation firstly presents a constrained multi-objective optimization framework for design and control of a SRM based on a non-dominated sorting genetic algorithm II (NSGA-II). The proposed methodology optimizes SRM operation for high volume traction applications by considering multiple criteria including efficiency, average torque, and torque ripple. Several constraints are defined by the application considered, such as the motor stack length, minimum desired efficiency, etc. The outcome of this optimization includes an optimal geometry, outlining variables such as air gap length, rotor inner diameter, stator pole arc angle, etc as well as optimal turn-on and turn-off firing angles. Then the machine is manufactured according to the obtained optimal specifications. Finite element analysis (FEA) and experimental results are provided to validate the theoretical findings.

A solution for exploring optimal firing angles of nonlinear current-controlled SRMs is proposed in order to minimize the torque ripple. Motor torque ripple for a certain electrical load requirement is minimized using a surrogate-based optimization of firing angles by adjusting the motor geometry, reference current, rotor speed and dc bus voltage. Surrogate-based optimization is facilitated via Neural Networks (NN) which are

regression tools capable of learning complex multi-variate functions. Flux and torque of the nonlinear SRM is learned as a function of input parameters, and consequently the computation time of design, which is crucial in any micro controller unit, is expedited by replacing the look-up tables of flux and torque with the surrogate NN model.

This dissertation then proposes a framework for the design and analysis of a coreless permanent magnet (PM) machine for a 100 kWh shaft-less high strength steel flywheel energy storage system (SHFES). The PM motor/generator is designed to meet the required specs in terms of torque-speed and power-speed characteristics given by the application. The design challenges of a motor/generator for this architecture include: the poor flux paths due to a large scale solid carbon steel rotor and zero-thermal convection of the airgap due to operation of the machine in vacuum. Magnetic flux in this architecture tends to be 3-D rather than constrained due to lack of core in the stator. In order to tackle these challenges, several other parameters such as a proper number of magnets and slots combination, number of turns in each coil, magnets with high saturated flux density and magnets size are carefully considered in the proposed design framework. Magnetic levitation allows the use of a coreless stator that is placed on a supporting structure. The proposed PM motor/generator comprehensive geometry, electromagnetic and mechanical dimensioning are followed by detailed 3-D FEA. The torque, power, and speed determined by the FEA electromagnetic analysis are met by the application design requirements and constraints for both the charging and discharging modes of operation. Finally, the motor/generator static thermal analysis is discussed in order to validate the proposed cooling system functionality.

To My Beautiful Parents

ACKNOWLEDGEMENTS

I would like to deeply thank my committee chair, Dr. Hamid A. Toliyat. I would like to extend to you my warmest appreciation for being a great adviser to me.

I also would like to thank my committee members, Dr. Palazzolo, Dr. Enjeti, and Dr. Bhattacharyya for their guidance and support throughout the course of this research. Thanks go to my friends and colleagues, especially Farzam Mortazavi, Edgar Galvan, and Yongqi Li for their help with my dissertation. Many thanks to the department faculty and staff for making my time at Texas A&M University a great experience.

I thank Dr. Hajirmirza and her student, Mine Kaya, for helping me with neural network modeling of my motor.

I also would like to thank Dr. Babak Fahimi for his help with my paper on Switched Reluctance Motor Design.

Finally, special thanks to my kindest family and my dear uncle, Arde, and his dearest wife, Patricia, for their encouragement and endless support.

CONTRIBUTORS AND FUNDING SOURCES

This work was supervised by a dissertation committee consisting of Professors Toliyat, Enjeti, and Bhattacharyya of the Department of Electrical and Computer Engineering and Professor Palazzolo of the Department of Mechanical Engineering.

All work for the dissertation was completed by the student, under the advisement of Professor Toliyat of the Department of Electrical and Computer Engineering.

There are no outside funding contributions to acknowledge related to the research and compilation of this document.

NOMENCLATURE

B	Coefficient of friction torque
g	Air gap thickness
J	Motor inertia
l_e	Motor stack length
$L(\theta, i)$	Phase inductance, function of rotor angle and current
m	Number of phases
N_r	Number of rotor poles
N_s	Number of stator poles
R_s	Phase resistance
S	Number of strokes per revolution
T_e	Electromagnetic torque
T_l	Load torque
T_m	Mechanical time constant
W_c	Co-energy
W_e	Electrical energy input
W_f	Magnetic stored energy
W_m	Mechanical energy output
β_r	Rotor pole arc
β_s	Stator pole arc
θ	Rotor position

θ_a	Aligned position
θ_u	Unaligned position
θ_{off}	Turn-off angle
θ_{on}	Turn-on angle
θ_{sk}	Stroke angle
τ_r	Rotor pole pitch
τ_s	Stator pole pitch
ω	Motor speed

TABLE OF CONTENTS

LIST OF FIGURES

LIST OF TABLES

1 INTRODUCTION*

1.1 Background

The Switched Reluctance Motor (SRM) has been gaining more popularity and a variety of researches have been done in the past several decades [1-3]. Researches can be mainly categorized into several areas, such as inductance and flux linkage measurements [4-7], mathematical model of SRM especially inductance and torque [8, 9], motor design and optimization [10-12], drive and control [13-17]. SRM shows the advantages of simple structure, cost-effectiveness and robustness [18,19]. Because windings only exist on the stator side and no windings or magnets on the rotor, SRM proves to be reliable in harsh environment since there is no rotor winding failure and demagnetization or flying off of the magnets [20]. In addition, because of absence of magnets, the motor price won't be bound by rare earth magnet materials which makes SRM a cost-effective candidate in many applications.

Energy conversion in SRM is closely related with power electronics devices. Each phase of the SRM is controlled independently and identical converter topology can be utilized for every phase. Several topologies are introduced and compared in [17]. Due to the simple structure of no magnet or winding on rotor, there is no conventional north and south poles on stator. So the stator excitation current is unidirectional. This not only simplifies the converter control, also provides more possibility for topologies to minimize the number of switched required.

---

* Part of this section is reprinted with permission from Yongqi Li, "Real-Time Torque Ripple Minimization of Outer Rotor Switched Reluctance Motor," Thesis, Texas A&M University, 2016.

Despites all the aforementioned advantages, SRMs suffer a major disadvantage which is high torque ripple. This is inherited from the phase commutation. To reduce the torque ripple at phase transition period, either optimized design of the motor or optimized control can be applied. Since the transition period is decided by the turn-on angle θ_{on} and turn-off angle θ_{off} of phases, good control with small torque ripple requires proper turn-on and turn-off angles, or also referred to as firing angles, so that transition is smooth. The details of determining firing angles is included in this dissertation.

1.2 Applications of SRM

The Switched Reluctance Machine can be used in many variable speed applications. A lot of literatures explore the design and control issues of SRM for Electric Vehicle (EV) and Hybrid Electric Vehicle (HEV) [19, 21, 22]. Some research has been done for wind turbine applications [23-25]. Other kinds of applications such as mining, hard disk drive, home appliances, aerospace, etc. are also investigated in the past.

The SRM studied in this dissertation is designed for hub-mounted or in-wheel electric vehicle application with an exterior rotor structure. Vehicle operation consists of three main segments, namely initial acceleration, cruising at the rated speed and cruising at the maximum speed. These three operation regions provide the basis design constrains for EV/HEV. The motor should be able to meet these constrains so that it can also function properly in other operational regimes.

2 FUNDAMENTAL OF SWITCHED RELUCTANCE MOTOR

2.1 Structure and Working Principles

The SRM has a double salience structure and only stator phases have windings which is the most notable feature of its simple structure. Stator windings are concentric coils on each pole. The motor can be either conventional inner rotor or outer rotor, as shown in Fig.1 and Fig. 2. Fig. 1 shows a four-phase inner rotor SRM with 8 stator poles and 6 rotor poles. This is a very common structure. Fig. 2 shows the outer rotor SRM studied in this dissertation, which has 4 phases 16 stator poles and 20 rotor poles. Assume the positive sign represents a north pole and negative sign represents a south pole.

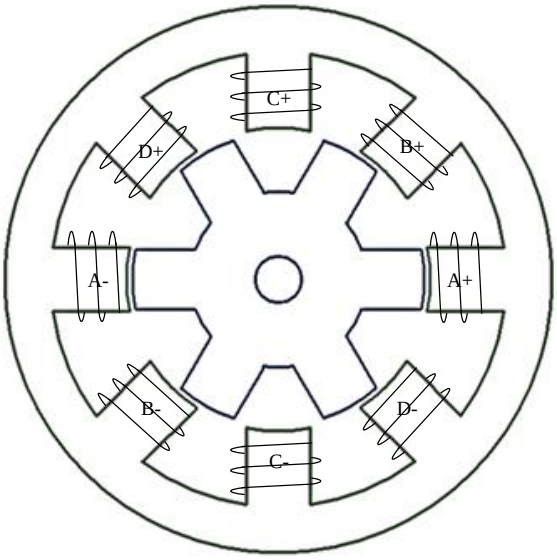

Fig. 1 An inner rotor SRM example.

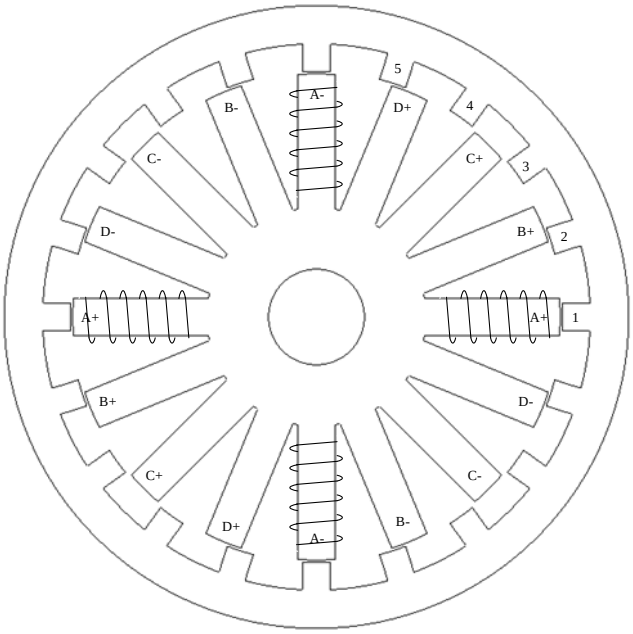

Fig. 2 The SRM studied in this dissertation.

The operation of Switched Reluctance Motor is based on the minimal reluctance path principle, which means the rotor always tends to move to the position at which the reluctance path is minimized. There are two important positions: the aligned position θ_a and unaligned position θ_u. The aligned position corresponds to the center of the stator and rotor pole facing each other, while the unaligned position indicates the center of the stator pole and center of the rotor interpolar gap coinciding. As shown in Fig. 2, phase A is aligned and phase C is unaligned.

The flux path reluctance is given by:

$$R = \frac{l}{\mu A} \tag{1}$$

where R is reluctance, l is flux path length, μ is permeability and A is cross section area of flux path. The relation between reluctance and inductance is

$$L = \frac{N^2}{R} \tag{2}$$

It can be seen that the reluctance is proportional to path length and the inductance is inversely proportional to path length. When the motor is at the aligned position, inductance is maximal while at the unaligned position it is minimal. Thus, the motor inductance is a function of position. Fig. 3 shows an idealized inductance and current profile. If current is applied during the inductance increasing period, meaning the rotor is moving toward the aligned position, torque will be produced and the switched reluctance machine will work as a motor. On the contrary, if current is applied when inductance is decreasing, the machine will work as a generator.

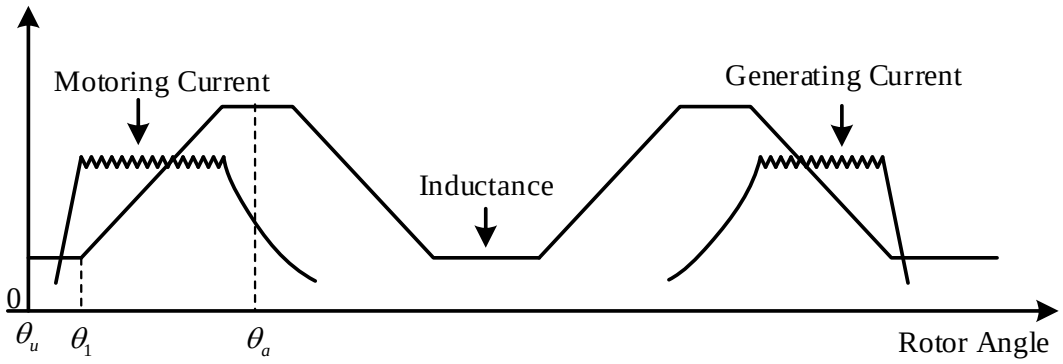

Fig. 3 Idealized inductance and current profile.

By energizing stator phases sequentially, the rotor poles will try to align with the nearest energized stator pole and the motor can rotate. Take the motor in Fig. as an example. Phase A is first energized and rotor pole 1 is aligned with pole A+. Next energize phase B and pole 2 will be aligned with pole B+. Finally phase A is energized again and pole 5 will be aligned with pole A-. So far one electrical cycle passes, and rotor rotates by one rotor pitch β_{rp}. From this analysis it can be seen, by rotating one rotor pitch, 4 strokes or 4 times of phase commutation have happened. To rotate one revolution, it required Nr electrical cycles. In general, the stroke angle can be defined as

$$\theta_{sk} = \frac{360°}{m \cdot N_r} \tag{3}$$

where m is the number phases and the number of strokes per revolution is

$$S = m \cdot N_r \tag{4}$$

It should be pointed out that the north and south polarity of each stator pole doesn not change, in other words, the magnetic flux direction of a certain pole does not change, unlike in induction or PM motor where north pole and south pole change alternatively. Thus the phase current is always unidirectional.

2.2 Comparison

A: Synchronous Reluctance Motor

As the name shows a great resemblance, it is a good idea to compare SRM with synchronous reluctance motor (SynRM). Since windings or magnets are eliminated from the rotor, SynRM has the aforementioned advantages similar to SRM. The SynRM have equal number of stator and rotor poles. The projections on the rotor are arranged to

introduce internal flux “barriers”, holes which direct the magnetic flux along the polar axis (d-axis). Table lists the summary and comparison of switched reluctance motor and synchronous reluctance motor [2].

Table 1 Comparison of SRM and SynRM

SRM	SynRM
1. Double salient poles	1. Smooth surface on both stator and rotor
2. Each stator winding is wound on one pole	2. Multiphase winding with sine distribution
3. Sequential current pulses excitation to each phase	3. Sinusoidal excitation
4. Triangular or sawtooth flux waveform	4. Sinusoidal self-inductance waveform

B: Stepper Motor

The stepper motor experience similarity to SRM in the topology and working strategy. However the differences lie in the design, control algorithm, performance and application. The stepper motor is usually run open loop and is designed to maintain step accuracy in position controls applications.

2.3 Selection of Phase and Pole Numbers

Number of stator phase and motor poles are important design parameters. Proper configuration can increase torque density, smooth the phase transition process and reduce torque ripple.

A: Number of Phases

To determine the number of phases, the following factors can be considered [1].

1. Cost. Since stator phases are controlled independently, each phase requires a set of hardware, such as power converter, drive, current sensor, etc. Increasing phase number will increase the system cost correspondingly.
2. Reliability. A higher number of phase can lead to more capability of fault tolerance. When one or more phases fail, the motor can still operate without additional special control.
3. Power density. With more number of phases, power density tends to increase.
4. Efficiency. With more number of phase, switching frequency has to increase thus increase the core loss and switching loss. As a result the efficiency is reduced.

Other factors like starting capability and directional capability can also be taken into consideration. At the meantime, the number of stator and rotor poles affect these factors together with the phase number.

B: Number of Stator and Rotor Pole

Some of the common combinations of stator and rotor poles are listed in Tabel 2 [2]. From the table, it can be concluded that stator and rotor poles are always even numbers; the ratio of stator pole over rotor pole is usually a non-integer. For the common combinations listed in the table, the pole number relationship can be represented by,

$$N_r = N_s \pm 2 \cdot \frac{N_s}{2m} \tag{5}$$

It should be pointed out there are other available combinations not agreeing with this equation.

Table 2 Common combinations of stator and rotor pole numbers.

m	N_s	N_r	θ_{sk}	S
2	4	2	90°	4
	8	4	45°	8
3	6	4	30°	12
	6	8	15°	24
	12	8	15°	24
4	8	6	15°	24
5	10	8	9°	40
6	12	10	6°	60

After choosing the pole numbers, stator and rotor pole pitches (β_{sp} and β_{rp}) can be determined. But the ratio of pole arc to pole pitch is still feasible to be a design variable. This ratio can be defined as pole enclosure. Reference [26] discusses the effect of stator and rotor pole enclosure on average torque. By analyzing the difference combination of pole enclosures and current levels, it is concluded that the stator pole enclosure should be in the range of 0.35 to 0.5 and the rotor pole enclosure in the range of 0.3 to 0.45.

2.4 Inductance Measurement

The equivalent circuit of SRM is shown in Fig. 4 as a series *R*-*L* circuit. Although it seems simple, what makes the problem complicated is that the inductance is a function of both rotor position and stator phase current. When the motor is saturated, current influence comes into the picture and inductance becomes non-linear.

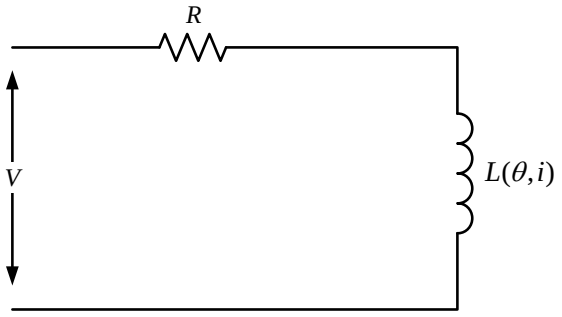

Fig. 4 Equivalent circuit of one phase.

The phase equation can be expressed as (6) and further expanded to (7).

$$v = R_s i + \frac{d\lambda}{dt} \tag{6}$$

$$v = R_s i + \frac{d(L(\theta, i) \cdot i)}{d\theta}$$

$$= R_s i + L(\theta, i)\frac{di}{dt} + i\frac{dL(\theta, i)}{d\theta}\frac{d\theta}{dt} + i\frac{\left(dL(\theta, i)\right)}{di}\frac{di}{dt} \tag{7}$$

$$= R_s i + L(\theta, i)\frac{di}{dt} + i\omega\frac{dL(\theta, i)}{d\theta} + i\frac{\left(dL(\theta, i)\right)}{di}\frac{di}{dt}$$

where v is the phase voltage and i is the current. If the inductance variation in terms of current is neglected, the last term in (7) will be eliminated and it reduces to a more common form:

$$v = R_s i + L(\theta, i)\frac{di}{dt} + i\omega\frac{dL(\theta, i)}{d\theta} \tag{8}$$

This is true because current is regulated at an almost constant value so the inductance variation caused by current can be ignored.

As a very important parameter, inductance and its measurement always gain attentions. With knowing the actual inductance profile, one can better analyze the motor performance and predict the torque produced which is important for direct torque control of SRM. Reference [6] investigated several measurement methods and they are summarized below:

1. Utilizing the *R-L* circuit response to a step input, applying a DC voltage to the motor phase and measuring the current transient response during energizing period. Based on (6), voltage and current can be integrated from the initial values to the steady state so that flux linkage can be calculated.

Dividing the flux by steady state current gives the inductance. Integration process can be done by some advanced oscilloscope easily.

2. Applying AC voltage to the phase then measuring the voltage and current. Impedance can be calculated from the RMS values. Knowing the value of phase resistance, the inductance can be obtained. If phase resistance cannot be accurately determined, then the phase shift between current and voltage waveform together with impedance may be used to calculate the inductance.
3. There is also a DC+AC method, in which a small AC voltage is imposed on the DC one. The magnetic circuit operation point is set by the DC voltage, while the AC voltage introduces sinusoidal current which works similarly to the second method. The advantage of this is that current will not be distorted too much at saturation status, compared to the pure AC method, so that it gives more accurate results at high current levels.
4. Measurements with a search coil where a search coil is used to estimate the value of phase inductance.

2.5 Energy Conversion

The Switched Reluctance Motor is an electromechanical energy conversion device that converts the input electrical energy to mechanical energy. During this energy conversion, part of the input energy is stored in the magnetic field. Fig. 5 shows the definition of stored field energy W_f and co-energy W_c. Their mathematical expressions are given by

$$W_f = \int_0^{\lambda_0} i(\lambda)\, d\lambda \tag{9}$$

$$W_c = \int_0^{i_0} \lambda(i)\, di \tag{10}$$

In Fig., AB represents a position displacement $\Delta\theta$. When moving from A to B, the input energy change is

$$\Delta W_e = \int ei\, dt = \int i\, d\lambda = ABCD \tag{11}$$

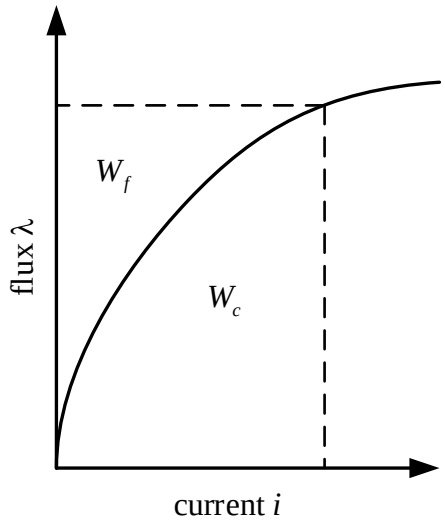

Fig. 5 Definition of stored magnetic energy W_f and co-energy W_c.

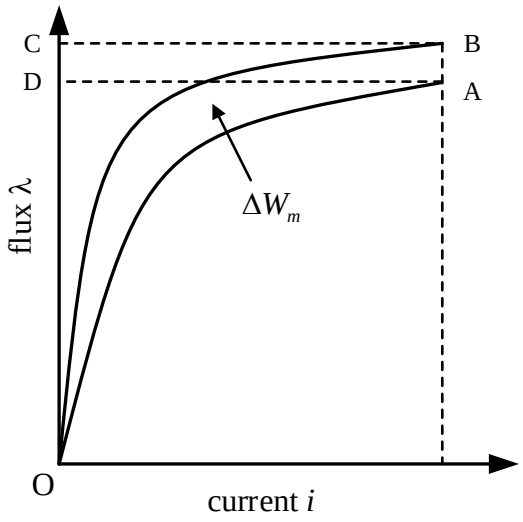

Fig. 6 Energy conversion.

The mechanical energy ΔW_m is the area of OAB and is equal to the co-energy change in this case. Torque can be calculated by,

$$T = \frac{\partial W_c}{\partial \theta} = \frac{\partial}{\partial \theta} \int_0^{i_0} [L(\theta, i) \cdot i]\, di \tag{12}$$

When the motor is saturated, the λ-i relation is a straight line so energy and co-energy are always equal. The torque equation reduces to:

$$T = \frac{d}{d\theta} \int_0^{i_0} L(\theta) \cdot i\, di = \frac{1}{2} i_0^2 \frac{dL(\theta)}{d\theta} \tag{13}$$

which is referred to as the linear torque equation since the inductance is not saturated and its value is not relying on current. Correspondingly, (12) is the non-linear torque expression.

2.6 Converter Topology and Control Strategy

The most commonly used converter topology is the asymmetric full bridge converter which consists of two switches and two diode in each phase. This topology allows fully independent control of every individual phase but the drawback is also evident that it requires a large number of devices. The cost will be challenging in multiphase system. Fig. 7 shows this topology for one phase and it is identical for the other phases.

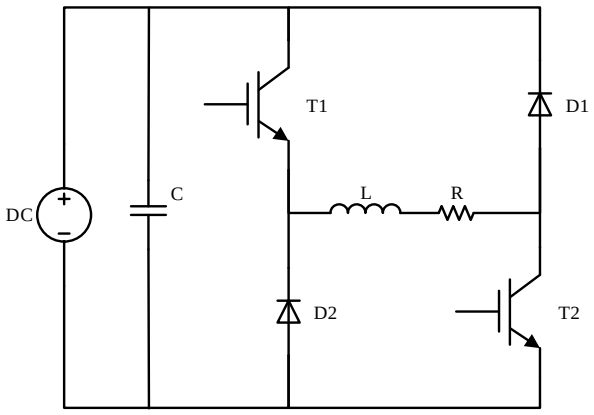

Fig. 7 Asymmetric full bridge converter.

Two strategies to control the phase current are hysteresis control and PWM control. Hysteresis controller has the advantages of simple implementation, fast response and motor independence [17]. However, the switching frequency is variable which leads to larger acoustic noise compared to the fixed frequency PWM controller. Moreover, in digital implementation, because of the current sampling rate limitation and the time delay between sampling and switch action, the hysteresis controller usually leads to higher

current ripple. In the hysteresis control, current error directly controls switches while in the PWM control the error first processed by a proportional-integral (PI) controller then the output of PI works as the compared value of PWM. This difference makes the hysteresis controller more sensitive to the noise of sampled signal inherently and further results in the higher current ripple again. Thus PWM controller is utilized in this dissertation.

The aim of current controller is regulating the current to follow the reference by turning on and off switches. No matter which kind of controller is adopted, for the full bridge converter, there are two switching strategies, namely hard chopping and soft chopping [27]. Fig. 8 illustrates the different switch status. Solid lines represent the current flowing path and the rest of paths are shown as dash lines. At the beginning of phase conduction, both two switches, T1 and T2 are on as shown in Fig. (8-a) and current rises from zero to its reference. Positive voltage is applied to the phase at this stage. When the phase is about to shut off at the last stage, both switches are turned off and current freewheels through the two diodes, shown in Fig. (8-c). Negative voltage is applied so phase current quickly drops to zero. Between this two stages, current is chopped. In hard chopping mode, switch status change between (a) and (c) while in soft chopping mode, status change between (a) and (b). With soft chopping, switch T2 is always on during the whole phase conduction period. When T1 is off, current can freewheel through switch T2 and diode D2. Voltage on the phase is almost zero.

During the second stage, current is usually desired to be smooth and maintain a flat-top shape, like in Fig. 3. When current is freewheeling in soft chopping mode, zero voltage

is applied so the current drops slower than hard chopping, which can give smaller current ripple at a given switching frequency. Thus, in this dissertation soft chopping strategy is employed.

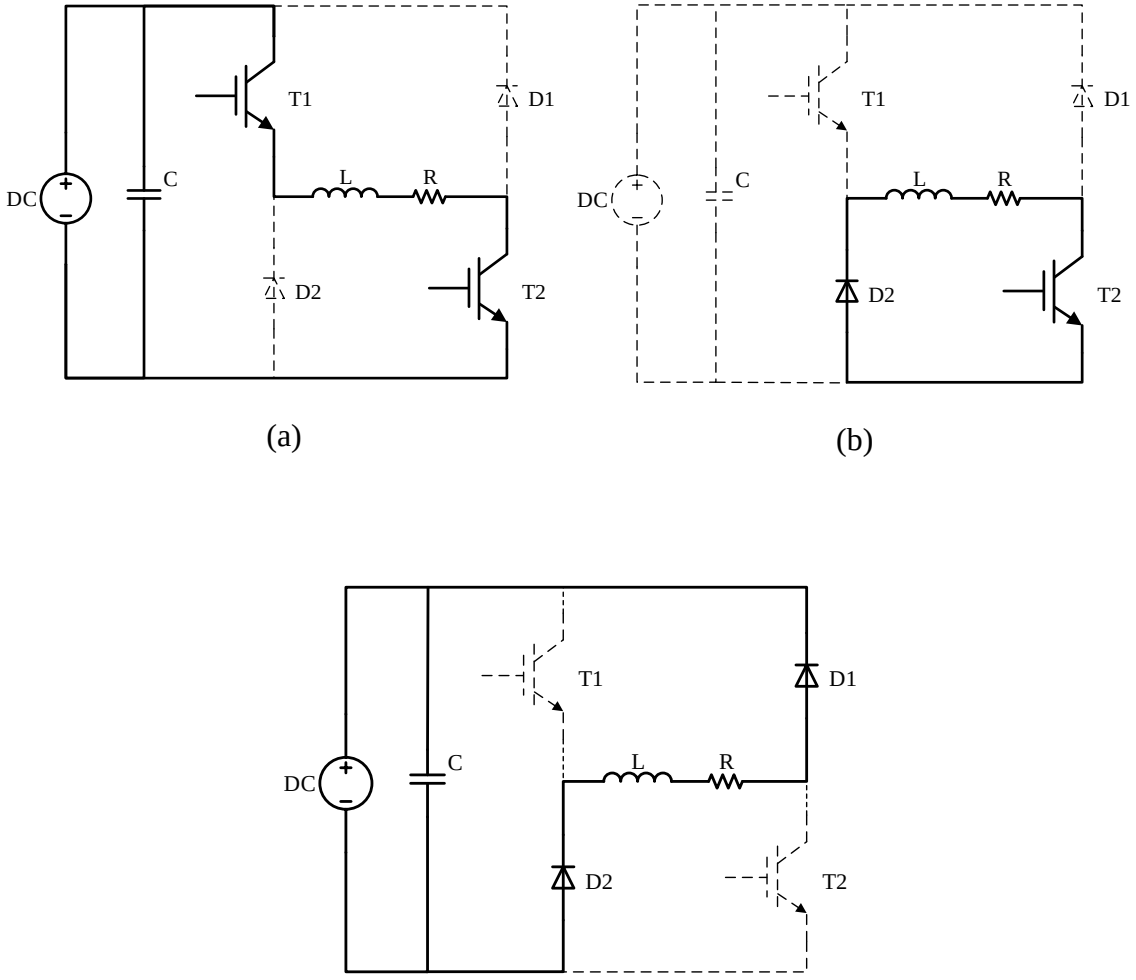

Fig. 8 Switching strategies.

Besides the aforementioned fundamental operating condition, there is another condition that current loses control which is called single pulse mode [28]. In this condition, positive voltage is always applied to the phase but current may still not be able to reach the reference value. Thus the current is not chopped and regulated. There are several reasons leading to this operation condition all together. By looking at (8), the third term containing speed and current is referred as the back-EMF. When motor is running at high speed, the back-EMF may be bigger than the supply voltage then current cannot increase anymore. In addition, when moving from the unaligned position to the aligned position, inductance value increases. This will increase the second term in (8) and make the right hand side of the equation greater than the supply voltage. Also at high speed, the rotor passes the inductance positive slope very quick and current does not have enough time to build up. Fig. 9 illustrates this condition.

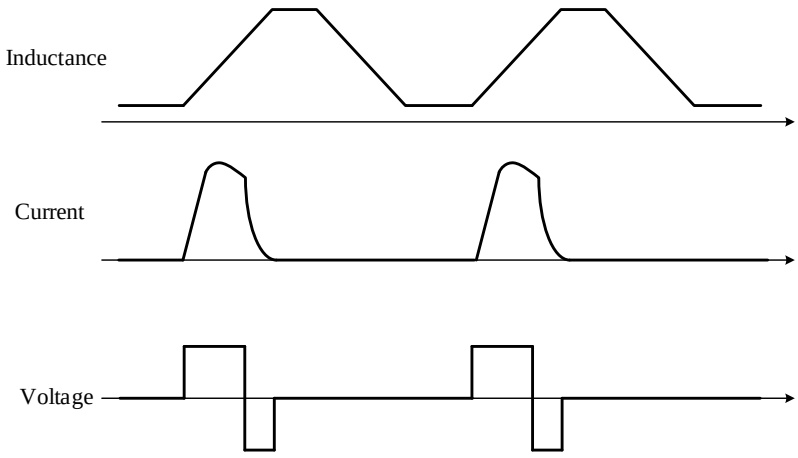

Fig. 9 Single pulse mode operation.

3 SIMULTANEOUS OPTIMIZATION OF GEOMETRY AND FIRING ANGLES FOR IN-WHEEL SWITCHED RELUCTANCE MOTOR DRIVE[1]

3.1 Introduction and Motivation

Interests in using rare-earth free motors such as switched reluctance motors (SRMs) for electric and hybrid electric vehicles (EV/HEVs) continue to gain popularity, owing to their low cost and robustness. Optimal design of an SRM, to meet specific characteristics for an application, should involve simultaneous optimization of the motor geometry and control in order to achieve the highest performance with the lowest cost. This work presents a constrained multi-objective optimization framework for design and control of a SRM based on a non-dominated sorting genetic algorithm II (NSGA-II). The proposed methodology optimizes SRM operation for high volume traction applications by considering multiple criteria including efficiency, average torque, and torque ripple. Several constraints are defined by the considered application, such as the motor stack length, outer diameter, minimum operating power, minimum desired efficiency, rated speed, rated current, and supply voltage. The outcome of this optimization includes an optimal geometry, outlining variables such as air gap length, rotor inner diameter, stator pole arc angle, rotor pole arc angle, rotor back iron, stator pole height, and stator inner diameter as well as optimal turn-on and turn-off firing angles. Then the machine is

[1] Part of this section is reprinted with permission from B. Anvari, H. A. Toliyat, and Babak Fahimi, " Simultaneous Optimization of Geometry and Firing Angles for In-Wheel Switched Reluctance Motor Drive," in IEEE Transactions on Transportation Electrification, vol. PP, no. 99, pp. 1-1.

manufactured according to the obtained optimal specifications. Comprehensive finite element analysis (FEA) and experimental results are provided to validate the theoretical findings.

The SRM converts electrical energy to mechanical energy via generation of reluctance torque and has been gaining popularity in various applications due to the following characteristics [29-31]:

a) It does not require bidirectional currents,
b) The major losses appear on the stator thus easier cooling and ventilation can be accomplished,
c) There are individual stator phases that do not stop drive operation in the case of fault in one or more phases,
d) It generates high torque with relatively low inertia,
e) It can generate constant power over a wide range of speed,
f) It enjoys a low cost and simple geometry.

By applying current to the stator windings, the closest rotor pole will align with the excited stator phase to minimize the magnetic reluctance. In pursuance of maintaining the motor rotation, the stator phases are energized sequentially [32, 33].

The idealized phase inductance and stator phase current are illustrated in Fig. 1; where θ_a and θ_u represent aligned and unaligned positions, respectively. According to (1), the torque is positive and electrical power is converted to mechanical power if the current is applied when the slope of the inductance is positive. On the contrary, if current is supplied while the inductance decreases, the resulting torque will be negative, thereby braking the rotor. In this case, the mechanical power will be converted to electrical power.

The electromagnetic torque, in the absence of magnetic saturation, can be expressed as [34]:

$$T = \frac{d}{d\theta}\int L(\theta)\cdot i di = \frac{1}{2} i^2 \frac{dL(\theta)}{d\theta} \tag{14}$$

The SRM phase voltage equation can be expressed by,

$$V_{dc} = R_s i + L(\theta,i)\frac{di}{dt} + i\omega\frac{d(dL(\theta,i),i)}{d\theta} = R_s i + L(\theta,i)\frac{di}{dt} + i\omega\frac{dL(\theta,i)}{d\theta} + i\frac{d(dL(\theta,i)}{d\theta}\frac{di}{dt} \tag{15}$$

which indicates the motor phase current (i) depends highly on the motor speed (ω) and inductance (L(θ,i)). V_{dc} represents the dc bus voltage that is applied to the phases when the phase is turned on. As demonstrated in Fig. 3, it is desired to reach the reference current at θ_1. Because the motor is highly inductive, the current cannot reach the reference value immediately; thus it is required to excite the phase prior to θ_1 that is called turn-on angle (θ_{on}). The same concept is true during turn-off process. It is desired that the current goes to zero once the inductance starts to exhibit negative slope to avoid any negative torque; hence it is required to turn off the phase before reaching the aligned position: this rotor position is called turn-off angle (θ_{off}). By appropriately adjusting θ_{on} and θ_{off}, a commutation overlap between outgoing and incoming phases occurs which could reduce the torque ripple [35,36].

Many optimization techniques for SRMs have been proposed in the literature. An optimal design of a high-speed three-phase SRM for a fuel-cell air compressor is proposed in [37]. The authors in [37] used a genetic algorithm to define the stator and rotor dimensions in order to minimize the copper and iron losses. Multi-objective optimization of a four-phase SRM for an electric vehicle (EV) application is presented in [38]. The

authors adopted NSGA-II in order to maximize torque factor, torque density, and quality factor while minimizing torque ripple where the considered optimization variables include the rotor and stator pole arc and taper angles. A new multi-objective design optimization method for an in-wheel outer rotor SRM for an EV application is developed in [39]. The proposed optimization algorithm in [39] is a function of maximum average values of torque per copper loss, torque, and torque per motor lamination volume where the rotor and stator pole arc angles are defined as the optimization variables.

All the aforementioned existing works consider only the motor geometries as optimization variables in order to optimally design the SRM. The work presented in [40] considers five sets of designs and applies genetic algorithm (GA) optimization for finding the optimal firing angles in order to minimize the torque ripple and maximize the average torque. However, this dissertation proposes a multi-objective optimization framework for SRM that simultaneously optimizes the geometry and commutation angles at the rated operating point. The sets of optimal designs which have the minimum torque ripple, maximum average torque and maximum efficiency have been investigated by the proposed optimization technique. In other types of machines, it is desired to align the phase current with the motional back-emf, whereas, in the SRM, this is done explicitly by literal tuning of turn-on and turn-off times. Inappropriate firing angles can lead to non-optimal operation of the SRM due to their significant effect on the motor output characteristics, especially average torque and torque ripple. As an example, if the firing angles are not set appropriately, the average torque could be low due to high torque ripple.

The proposed simultaneous optimization in this work will optimally select the firing angles to avoid oversizing the motor for specific torque-speed characteristics.

3.2 Initial Design of Switched Reluctance Motor

Fig. 10 illustrates the EV in-wheel mounted motor assembly. Hence, an outer rotor SRM is designed for this application. Using an outer rotor configuration along with a direct drive system allows the elimination of gears and other mechanical parts that are usually required in an indirect drive system [41].

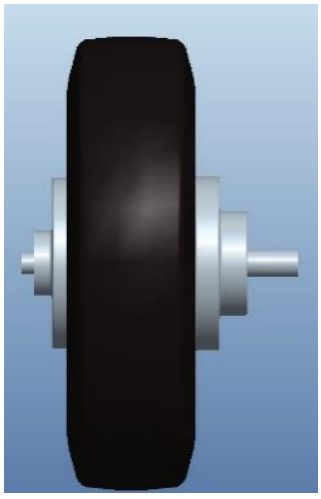

Fig. 10 Hub mounted motor assembly.

The appropriate engineering trade-off between objectives depends on the considered application, the preferences for decision making can be set according to the considered application. In such scenarios, it is beneficial to visualize the optimal set of solutions for the optimization objectives as a form of “Pareto Frontier” [42]. In this work, Pareto

Frontier is used as a visualization tool to choose the unique design from the set of feasible designs based on particular preferences for the application under study.

Table 3 gives a sample application requirements and constraints provided by a Vehicle Manufacturer Company that should be met by the optimally designed motor drive system. By considering the application requirements, the SRM initial dimensions are obtained from SRM traditional design method that is presented in [43]. The transient and the heuristic technique are used to expedite the optimization process time. The firing angles are optimized for this design by trying 100 different combinations of turn-on and turn-off angles to get the highest average torque and efficiency while concurrently minimizing the torque ripple. Table 4 gives the initial dimensions of the SRM design that is established by analytical calculation in conjunction with heuristic technique. Having higher number of phases with the relatively small saliency ratio along with increasing the number of rotor poles are the primary objectives of the torque ripple minimization [44]. Four-phase, five-phase, and six-phase SRMs with exterior rotor are examined successfully. Considering the motor and converter sizes, the four-phase SRM with 16 poles on the stator and 20 poles on the rotor has been selected for this application. According to Table 4, the rotor has higher numbers of poles than the stator in order to achieve higher torque per volume [45]. Table 5 demonstrates the designed motor output characteristics at rated speed i.e. 400 rpm. The average torque is 57.5 N.m, which is lower than the minimum torque required by the application i.e. 60 N.m. The achieved efficiency of 80% is significantly lower than the desired efficiency of 85%. Furthermore, the motor output power does not even meet the minimum desired power. Torque ripple is 10 N.m,

that is 17% of the average torque, which is relatively high although torque ripple has not been identified as an objective in the application. The motor mechanical aspects such as weight and rotor inertia are fairly acceptable.

Table 3 The SRM design requirements

Motor specification	Value	Unit	Motor specification	Value	Unit
Rated speed	400	rpm	Stack length	150	mm
Operating voltage	60	V	Outer diameter	220	mm
Operating current	50	A	Maximum operating temp	+70	°C
Output power	>2.5	kW	Weight	<50	kg
Efficiency at rated condition	>85	%	Cooling system	Air cooling	-

Table 4 The SRM initial design dimensions and specifications

Motor specification	Value	Unit	Motor specification	Value	Unit
Number of stator poles (N_s)	**16**	**-**	**Number of turns/ pole (N_p)**	**45**	**-**
Number of rotor poles (N_r)	**20**	**-**	**Number of phases (m)**	**4**	degree
Stator inner diameter (D_{is})	20	mm	Stator pole arc angle (B_s)	6°	degree
Stator outer diameter (D_{os})	178.6	mm	Rotor pole arc angle (B_r)	5°	degree
Rotor inner diameter (D_{ir})	179	mm	Stator pole height (h_s)	43	mm

Table 4 Continued

Motor specification	Value	Unit	Motor specification	Value	Unit
Rotor outer diameter (D_{or})	**220**	mm	Rotor pole height (h_r)	12.5	mm
Air gap length (g)	0.2	mm	Turn-on angle (θ_{on})	40°	degree
Rotor back iron (b_{ry})	8	mm	Turn-off angle (θ_{off})	50°	degree
Stator back iron (b_{sy})	36.3	mm	**Stack length (L)**	**150**	mm

Table 5 The initial SRM electrical and mechanical specifications

Quantity	value	Unit	Quantity	value	Unit
Rotor core mass	9.46	kg	Winding phase resistance	0.0244	Ω
Stator core mass	18.9	kg	Winding turn length	357	mm
Stator winding mass	6.48	kg	Output average torque	57.5	N.m
Motor total mass	34.84	kg	Torque ripple	10	N.m
Rotor moment of inertia	0.108	kg/m^2	Output power	2.4	kW
Slot fill factor	50	%	Efficiency	80	%

The bold entries in Table 4 illustrate the motor dimensions and specifications that are determined to be fixed. The geometry and control variables are: stator inner diameter (D_{is}), rotor inner diameter (D_{ir}), stator pole arc angle (B_s), rotor pole arc angle (B_r), air gap length (g), stator pole height (h_s), rotor back iron (b_{ry}), turn-on angle (θ_{on}), electrical degree before the rotor reaches the unaligned position, and turn-off angle (θ_{off}), electrical degree before the rotor reaches the aligned position. Fig. 11 illustrates the proposed four-phase 16/20 SRM with winding configuration and labeled optimization variables. The rotor pole height (h_r) and the stator outer diameter (D_{os}) can be obtained from the following equations:

$$h_r = \frac{1}{2}(D_{or} - D_{ir} - 2b_{yr}) \tag{16}$$

$$D_{os} = D_{ir} - 2g \tag{17}$$

Considering the fixed operating voltage and current by the application, (18) is used to calculate the number of turns per pole (N_p) [43].

$$2H_g g = N_p I_{\max} \; ; \; H_g = \frac{B_m}{\mu_0} \tag{18}$$

Where H_g is the maximum field strength in the air gap, g is the air gap length that is considered to be 0.2 mm, and B_m is the saturated flux density in the air gap which is presumed to be 1.7 T. $I_{\max}$ is the maximum current per coil which is 12.5 A in this case due to paralleling coils of each phase.

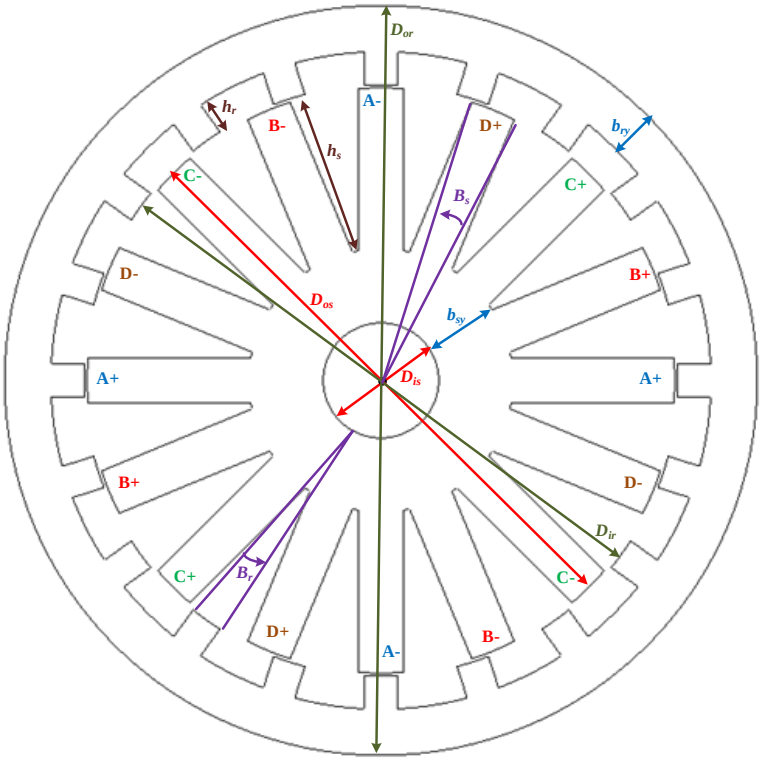

Fig. 11 The four-phase outer rotor 16/20 SRM.

3.3 Optimal Design of Switched Reluctance Motor

A common method to optimize the SRM design and operation is to determine the optimum motor geometry using static analysis. After determination of optimum geometry, the SRM will be derived at its full speed rating with optimal firing angles to find out if the design meets the required features and constraints such as torque ripple, average torque, etc. If the designed SRM does not meet the required characteristics, another design/firing angles should be considered. There exists a distinct set of firing angles for optimal operation of a particular geometry. In some cases the geometry optimization should be re-

done due to possible changes in design constraints. Thus a design-build-test cycle needs to be iterated, often at substantial cost and time. This dissertation proposes an optimization method using transient analysis to find the optimal geometry and firing angles simultaneously. Thus, the optimum design can be achieved without changing the motor size and constraints.

There are alternative methods that can be implemented to optimize the proposed system. In this work, the focus was on the accurate problem formulation which is the most important part of any optimization work, hence a well-known tool, NSGA-II, is used to visualize the set of optimal solutions as a form of Pareto Frontier [46]. NSGA-II is a general-purpose multi-objective genetic algorithm for locating solutions on the Pareto frontier [47]. Genetic algorithms (GAs) are population-based metaheuristic optimization algorithms [48]. A GA uses concepts inspired by biological evolution, such as selection, reproduction, mutation, and recombination [48]. A fitness function determines the quality of the solutions (i.e., the current population). The aim is to bias the subsequent generation towards the desirable region of the search space.

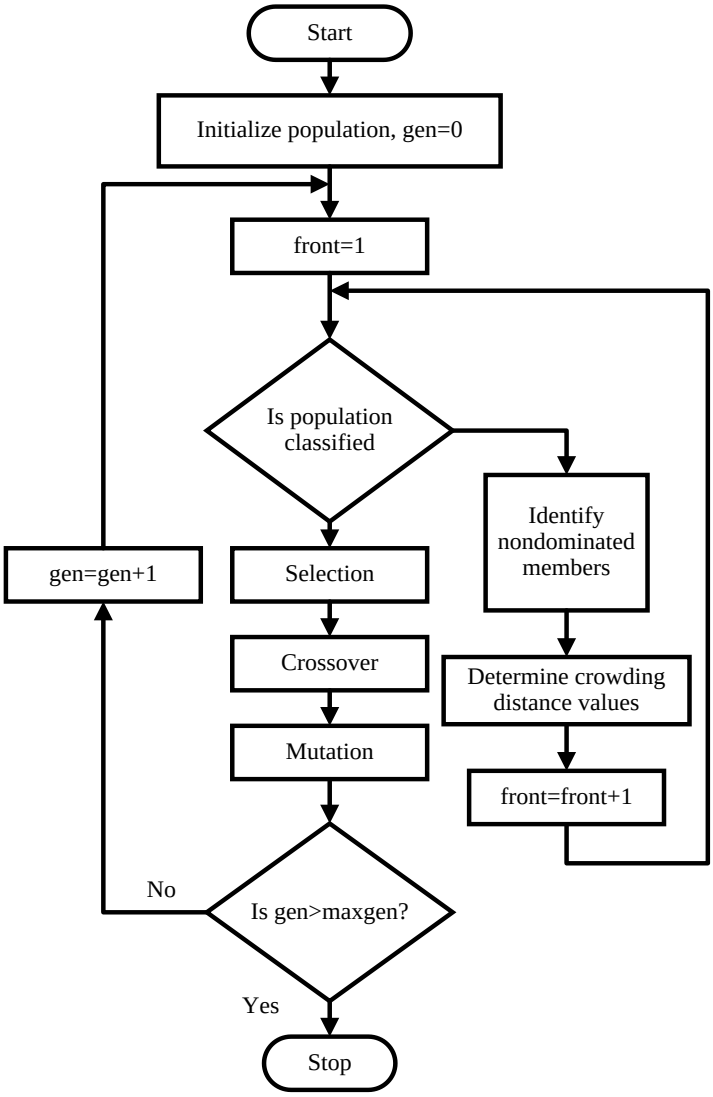

Fig. 12 The NSGA-II algorithm flowchart.

The advantage of the NSGA-II approach to multi-objective optimization is that by iterating over a population of solutions rather than one single point, the algorithm is able to find a set of solutions in a single run [46]. Furthermore, via the recombination operator,

a type of "knowledge sharing" among solutions is achieved by combining promising features to create new solutions in unexplored parts of the search space. A high-level flow-chart of the NSGA-II algorithm applied to the problem at hand is presented in Fig. 12 [46]. In order to assign fitness to the population members, NSGA-II incorporates the non-dominated sorting method. In this method, before the selection operation is performed, the population is ranked on the basis of a member's "non-domination". To define non-domination, suppose designer preferences are monotonically decreasing in each objective y_i for $i = 1, \dots, M$. If $y = (y_1, y_2, \dots, y_M)$ denotes a vector objective space and $Y \subseteq \mathbb{R}^M$ is the set of all feasible objective values, then Pareto dominance is defined as follows [49]:

An alternative having attributes $y"$ is Pareto dominated by one with attributes y' if and only if, $y_i' \leq y_i"$ $\forall i = 1, \dots, M$ and $y_i' < y_i"$ $\exists i = 1, \dots M$. With this definition of Pareto dominance, the pseudo code for the non-dominated sorting procedure is as follows:

1. Set all non-dominated sets P_j, for $i = 1,2, \dots$ as empty sets,
2. Set non-domination rank counter $j = 1$,
3. Find the non-dominated set P' of population P,
4. Update $P_j = P'$, $P = P/P'$, and counter $j = j + 1$,
5. Return to step 3 if termination criteria is not met.

The non-dominated sorting technique is widely used and has been shown to promote population diversity and improve convergence [46, 50, 51].

In addition to being converged closely to the non-dominated frontier, solutions must also be sparsely spaced along the non-dominated frontier. Since predictive parameterized Pareto Genetic Algorithm (P3GA) deals with two spaces, decision variable space and

performance space, ‘diversity’ among solutions can be defined in either of these spaces. Because the interest is in accurately representing the performance space, the focus is on diversity in that space. The diversity preservation operator assigns higher fitness to members that lie in less “crowded” regions of the space. Several crowding distance metrics have been proposed in the literature. The crowding distance technique used in NSGA-II sorts the set of solutions according to each objective function. The solutions are assigned distance values equal to the absolute difference of the objective values of the two adjacent solutions; an example is illustrated in Fig. 13.

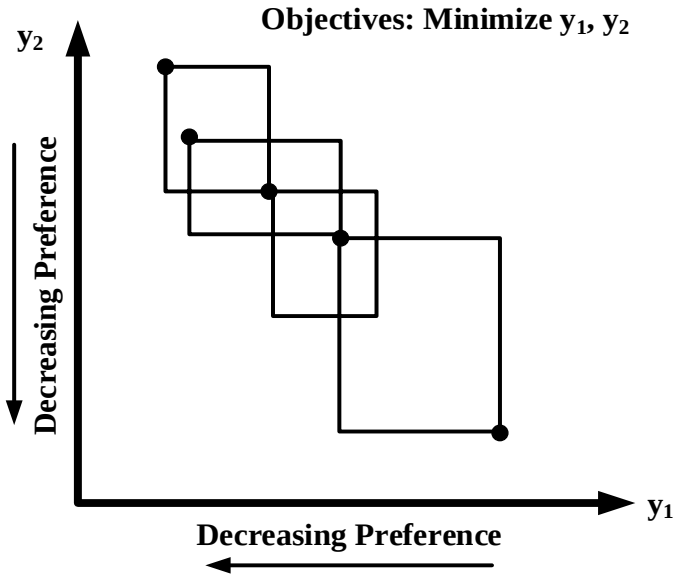

Fig.13 An example of NSGA-II crowding distance metric.

Once the population has been sorted into non-dominated ranks, each rank is arranged in descending order of magnitude of the crowding distance values. Then the Crowded

Tournament Selection operator proposed in [52] is used to determine the parents for the offspring. The Crowded Tournament Selection operator is defined as follows. A solution i wins a tournament with another solution j if any of the following conditions are true:

a) If solution i has higher rank than j,

b) If solution i and j have equal rank but solution i has better crowding distance than j.

The first condition ensures that the chosen solution lies on the better non-dominated frontier. The second condition resolves the tie that occurs when both solutions are on the same non-dominated frontier. The solution in the less crowded area wins. Once the parents have been selected, the usual recombination and mutation operators are used to create offspring.

The developed motor design and control optimization flowchart is illustrated in Fig. 14. According to the initial parameters set developed in Matlab, which are the initial design geometry and firing angles, the motor lamination will be plotted in FEA, MotorSolve package is used in this study. The motor will be simulated at rated condition with reference current of 50 A and reference speed of 400 rpm using a current regulated voltage source inverter. The output characteristics will be saved into the optimization program which is established in Matlab. Afterward, NSGA-II finds a new set of parameters and the procedure continues until the number of populations and generations reaches the defined targets which makes the stopping criteria satisfied.

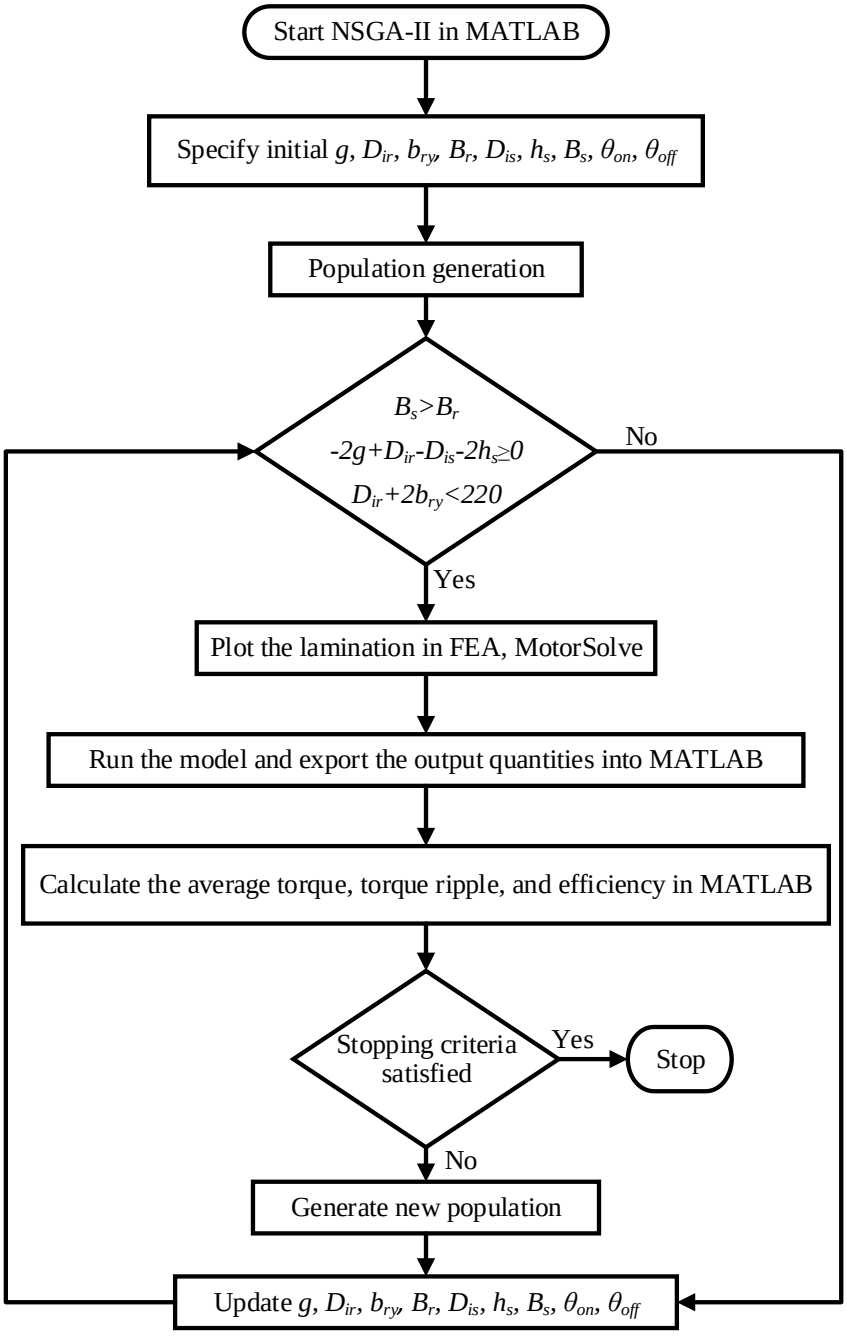

Fig. 14 Multi-objective design optimization procedure of the SRM.

In this dissertation, it is assumed that the designer of the motor has control over 9 common design variables, denoted by,

$$x = \left(g, D_{ir}, b_{ry}, B_r, D_{is}, h_s, B_s, \theta_{on}, \theta_{off}\right) \tag{19}$$

The design variables are constrained by reasonable lower and upper bounds as required by the application and accomplished by the heuristic technique:

$$\begin{aligned} lower-bound &= (0.15, 175, 7, 5, 15, 40, 6, 20, 10) \\ upper-bound &= (0.3, 200, 11, 9, 35, 50, 10, 80, 80). \end{aligned} \tag{20}$$

The air gap length varies in a small range of 0.15 mm to 0.3 mm which is a known requirement of SRM comparing to other types of motors [45, 52]. The rotor and the stator pole arc angles should approximately be the same. If the stator pole arc angle is greater than the rotor pole arc angle ($B_s > B_r$) the inductance will be constant until the rotor moves to a position where (B_s-B_r) deviates from the aligned position. In other words, there would be a torque dead zone centered on the aligned position. The same condition exists when ($B_r > B_s$). The dead zone increases the available time for the flux to drop to zero after commutation, before the torque moves to the negative zone. Hence, it is an advantage that could be considered [43]. In the proposed SRM, the stator pole arc angle is preferred to be larger than the rotor pole arc angle because the stator has fewer poles than the rotor. Such considerations along with physical and geometrical considerations result in the following design constraints:

$$\begin{aligned} & B_s > B_r \\ & -2g + D_{ir} - D_{is} - 2h_s \geq 0 \\ & D_{ir} + 2b_{ry} < 220. \end{aligned} \tag{21}$$

The performance metrics of interest (torque ripple, efficiency, and mean torque) are a function of the design variables:

$$\begin{aligned} &\tau_{ripple}(x), \\ &\eta(x), \\ &\tau_{mean}(x). \end{aligned} \tag{22}$$

Which are computed using MotorSolve. With this notation, the multi-objective optimization problem can be stated as:

$$\min_x \left(\tau_{ripple}(x), -\eta(x), -\tau_{mean}(x)\right) \tag{23}$$

Subject to

$$\begin{aligned} &x_7 - x_4 < 0 \\ &2x_1 - x_2 + x_5 + 2x_6 \le 0 \\ &x_2 + 2x_3 \le 0 \\ &lb \le x \le ub \end{aligned} \tag{24}$$

where $\tau_{ripple}(x)$ in N.m is the SRM torque ripple, and the standard deviation of output torque is calculated as the indication of torque ripple. Motor efficiency is represented by $\eta(x)$, and $\tau_{mean}(x)$ is the average torque that are all obtained from FEA. Motor efficiency $\eta(x)$ is obtained by subtracting the motor total loss including core loss and copper loss from the input power using the FEA package. Note that the objectives to be maximized are negated since maximizing an objective *f* is equivalent to minimizing *-f*. Hence, the goal is to discover the set of solutions that simultaneously minimize all objectives. For this case study, the NSGA-II algorithm was run for 50 generations using a population size of 20. The typical re-combination and mutation parameters [46] were used in order to solve the optimization problem.

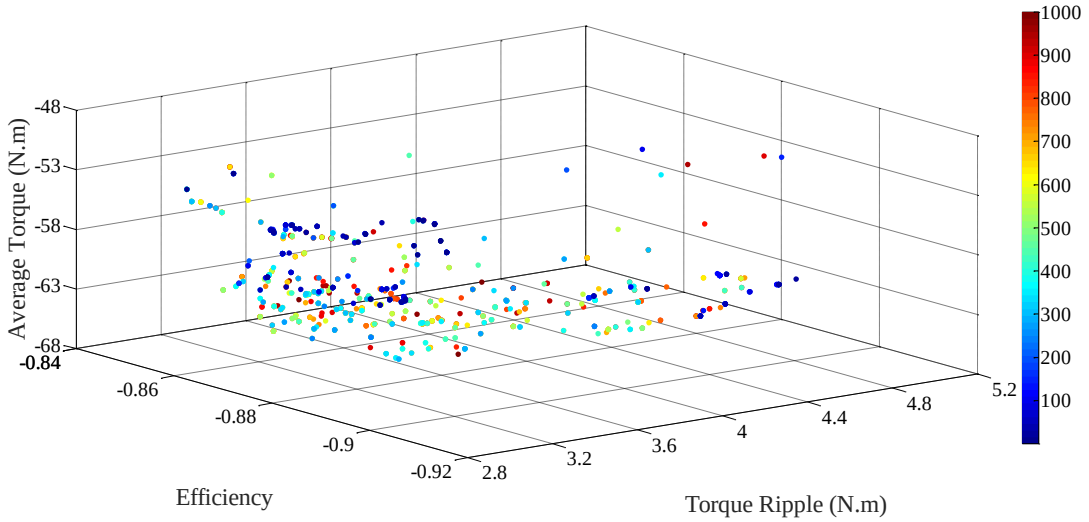

Fig. 15 The optimization objectives results for all studied points.

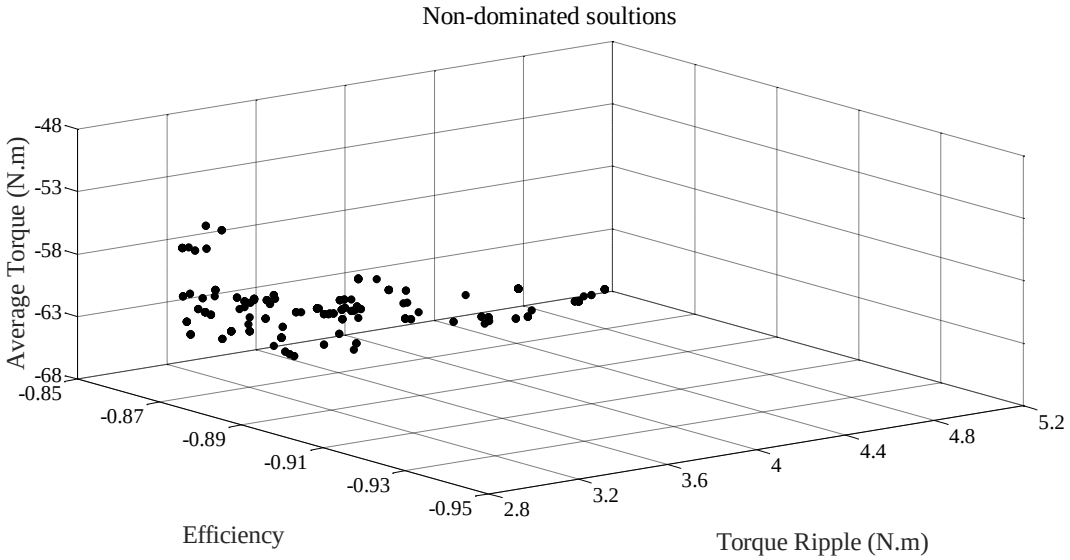

Fig. 16 Estimation of non-dominated frontier.

3.4 FEA Optimal Design Results

The results of the search are presented in Fig. 15. The figure is an illustration of every point evaluated during the search. The color map illustrates the progression of the search; the final population is illustrated in red. Fig. 16 is intended to facilitate visualization; a mesh is fit to the Pareto optimal points found. By considering the application

requirements, the candidate points that are given in Fig. 16 are studied.

In this framework, a particular decision making algorithm such as utility theory is not used to make the final decision [53, 54]. The final design parameters are chosen manually based on the design requirements by a vehicle manufacturer company and using the non-dominated solutions given by the Pareto frontier in Fig. 16. For this specific application, the average torque had the highest priority for the vehicle manufacturer company. Thus the design that leads to the closest average torque to the application required torque is selected with efficiency of 85.76%, average torque of 61.4N.m, and torque ripple of 3.88 N.m. The motor optimized geometry variables are given in Table 6. These variables are used to generate the electrical and mechanical specifications of the optimized SRM by FEA which are listed in Table 7.

Table 6 The SRM optimized design geometry

Variable	value	Unit	Variable	value	Unit
Stator inner diameter (D_{is})	25	mm	Stator pole arc angle (B_s)	9^0	degree
Stator outer diameter (D_{os})	179.5	mm	Rotor pole arc angle (B_r)	6.5^0	degree
Rotor inner diameter (D_{ir})	180	mm	Stator pole height (h_s)	45.5	mm
Air gap length (g)	0.25	mm	Rotor pole height (h_r)	10	mm
Rotor back iron (b_{ry})	10	mm	Turn-on angle(θ_{on})	50°	degree
Stator back iron (b_{sy})	31.75	mm	Turn-off angle (θ_{off})	70°	degree

Table 7 The SRM optimized electrical and mechanical specifications

Quantity	value	Unit	Quantity	value	Unit
Rotor core mass	10.1	kg	Stator teeth hysteresis loss	53.1	Watts
Stator core mass	18.2	kg	Stator teeth eddy current loss	9.8	Watts
Stator winding mass	6.46	kg	Rotor back iron hysteresis loss	37.7	Watts
Motor total mass	34.76	kg	Rotor back iron eddy current loss	8.1	Watts
Rotor moment of inertia	0.107	kg/m^2	Rotor teeth hysteresis loss	14.4	Watts
Slot fill factor	50	%	Rotor teeth eddy current loss	3.1	Watts
Winding phase resistance	0.024	Ω	Total loss	430	Watts
Winding turn length	355	mm	Output average torque	61.4	N.m
Copper loss	288	Watts	Torque ripple	3.88	N.m
Stator back iron hysteresis loss	14.4	Watts	Output power	2.57	kW
Stator back iron eddy current loss	2.2	Watts	Efficiency	85.76	%

The motor flux plot is demonstrated in Fig. 17 for the case when it is not saturated and one phase is energized. In this case, the rotor pole is aligned with the energized stator pole. Fig. 18 illustrates the flux lines at aligned position with only one phase energized at 50 A, which leads the motor into saturation. The maximum flux density at saturation

is 1.78 T, mostly in the airgap and at rotor aligned pole tips. This flux density value is well into saturation level for the non-oriented silicon steel used [43].

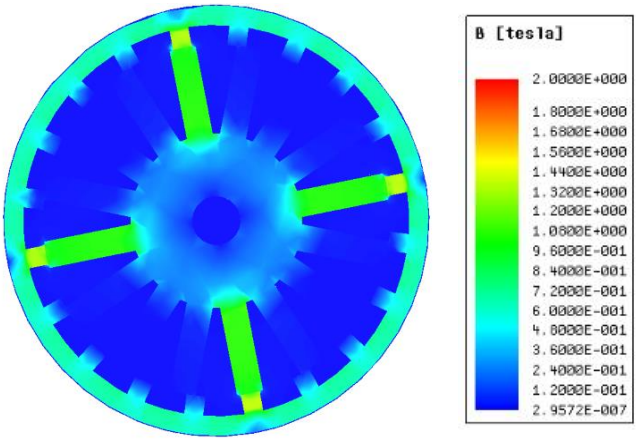

Fig. 17 Flux lines at aligned position at unsaturated condition, current at 20 A and 400 rpm.

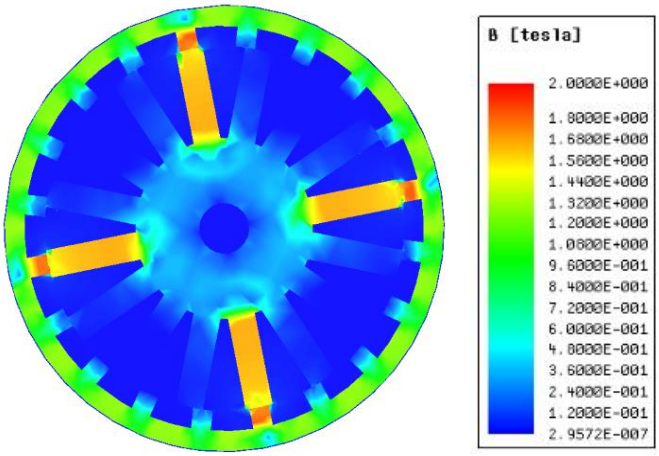

Fig. 18 Flux lines at aligned position at saturated condition, current at 50 A and 400 rpm.

3.5 Experimental Results

Fig. 19 illustrates the disassembled actual motor stator and its outer rotor that are built based on optimal geometry obtained. The motor test-bed and the H-bridge inverter

blocks are presented in Figs. 20 and 21 respectively. The Digital Signal Processor (DSP) TMS320F28335 is used in this experimental setup to control the SRM. The ABB drive DCS 800 loads the dc generator, and an interface board connects the DSP to the inverter. The sensed currents are fed into the analog to digital (ADC) channels on the DSP. The laboratory inverters used for experiments have 30 A current limits, thus for protection purposes, the experiments were limited to 25 A. The motor control block diagram is presented in Fig. 22 where inside the dashed rectangular box the DSP functions are illustrated. The rotor position and phase currents of the motor are fed into the DSP by the position sensor and current sensors on the interface board, respectively. The motor phases are modeled in the block "SRM" which includes the motor inductance-position-current look-up table imported from FEA. The motor inductance is measured at different rotor angles from aligned to unaligned positions at different currents to verify the look-up table imported from FEA. The flux-linkage measurement method is used which is described in [55]. In this method voltage applies to the motor phase directly without using an inverter, hence the inductance is measured at saturation with rated current of 50 A as well as unsaturated condition. The measured inductances are compared with the calculated inductances in FEA in Fig. 23. As it is shown, good agreement is achieved between the FEA and experiment inductances that confirms the accuracy of the SRM model in DSP code composer.

A classical PI based control in conjunction with pulse width modulation (PWM) are used to regulate the motor current while the phase is conducting. There are two switching strategies, namely hard chopping and soft chopping [56]. Soft chopping method is implemented in this work to reduce the current ripple during the regulation which affects the motor output characteristics, mostly the torque ripple. In order to

validate the proposed controller, the voltage and current for two different speeds are presented. Fig. 24 demonstrates the experimental motor phase current and voltage labeled as 1 and 2 respectively at 200 rpm. The phase voltage is either the positive dc bus voltage (V_{dc}) or 0 during conducting period. When the phase is turned off, all switches are off and the phase voltage becomes $-V_{dc}$. Fig. 25 illustrates the experimental motor phase current and voltage at rated speed i.e. 400 rpm.

As it is explained in the introduction, the most dominant objective for the proposed traction application is the motor average torque. The motor torque-speed characteristics with constant reference current, 25 A, in FEA and experiment are compared in Fig. 26. There is a negligible difference between experiment and FEA results that could be due to friction and windage losses of the system which are not included in the FEA model [57].

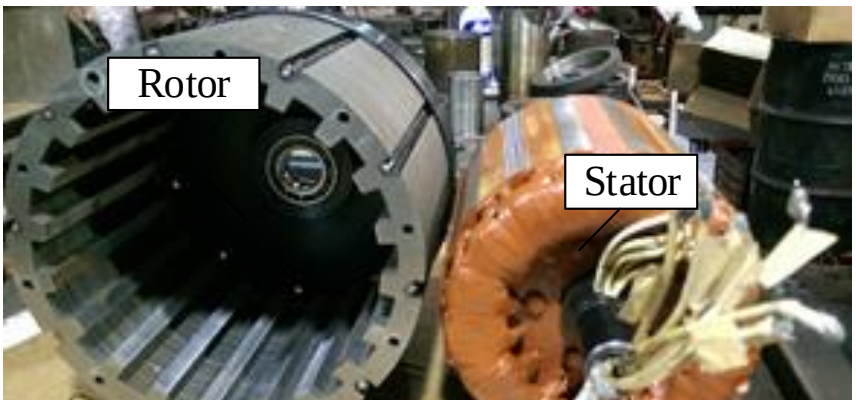

Fig. 19 The actual motor.

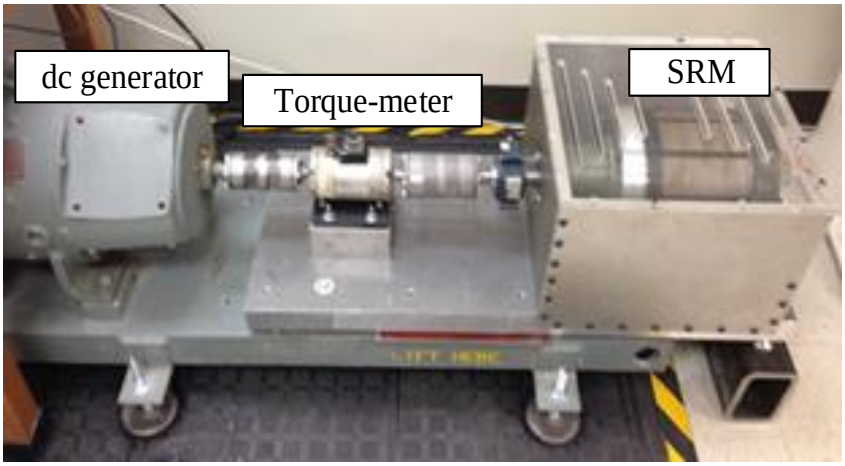

Fig. 20 The motor test bed.

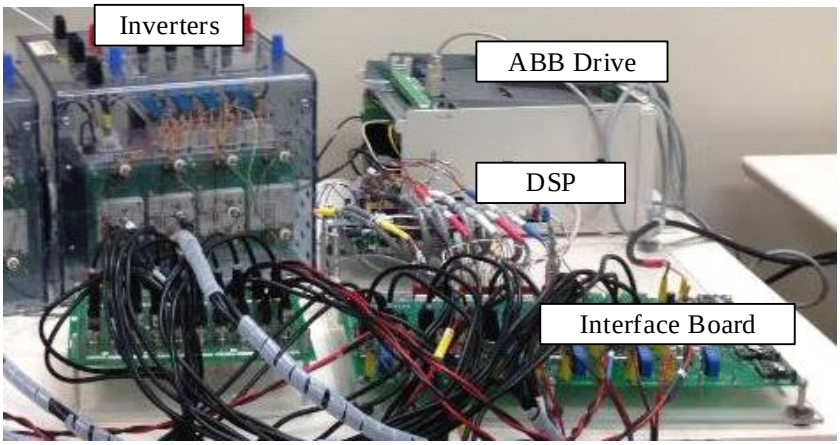

Fig. 21 Four-phase drive setup controlled by DSP.

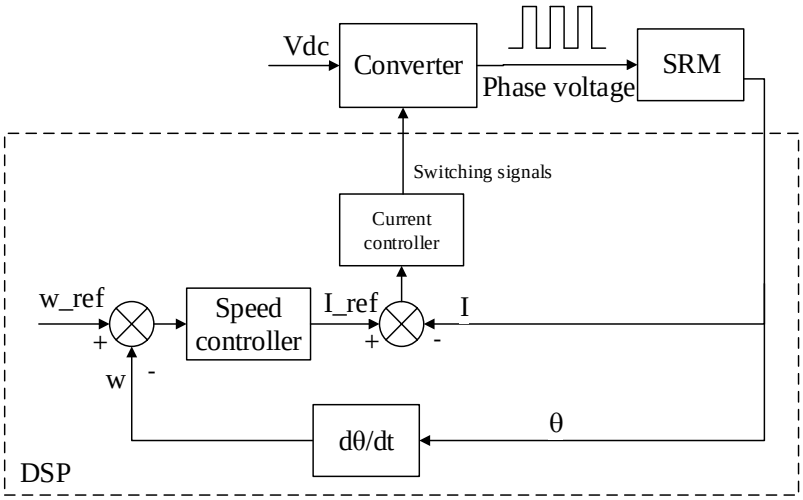

Fig. 22 Motor phase control block diagram.

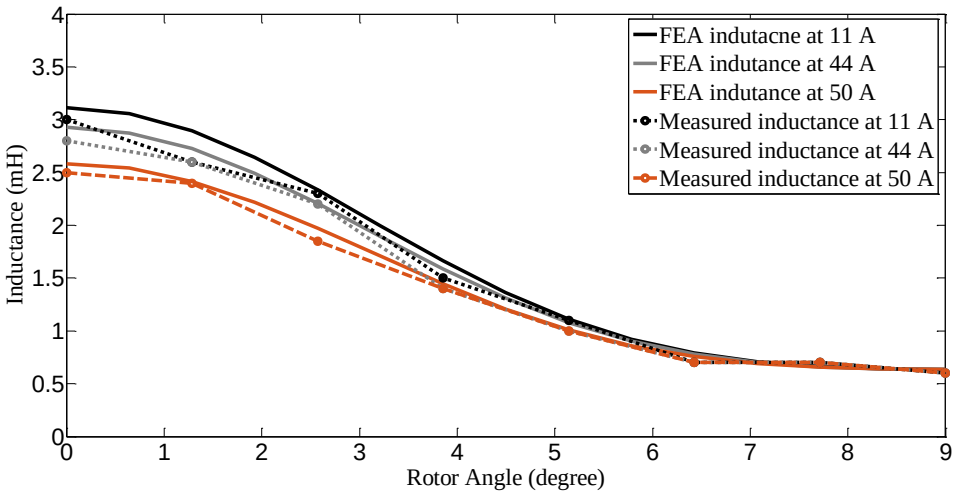

Fig. 23 Motor inductance measurements comparison in FEA with experiment from aligned position (0˚) to unaligned position (9˚).

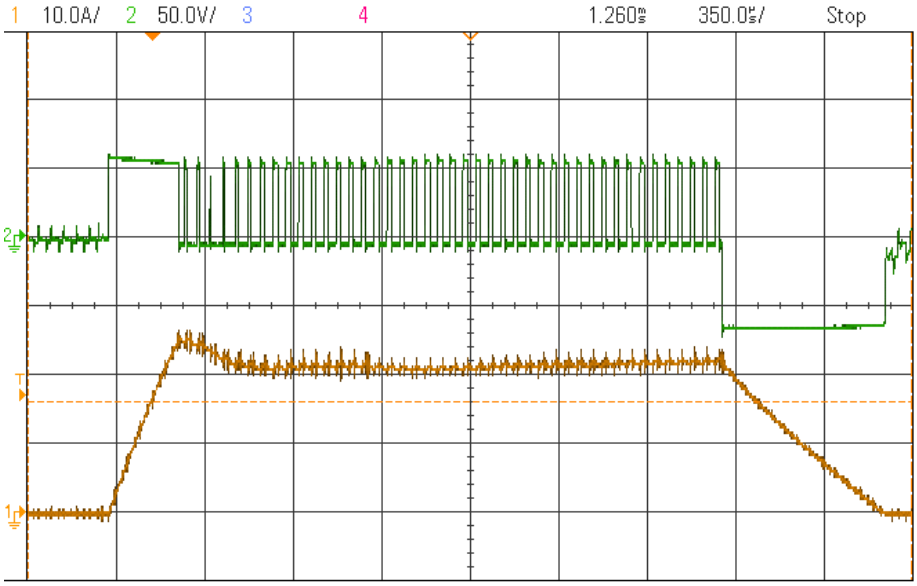

Fig. 24 The motor experimental voltage and current at 400 rpm.

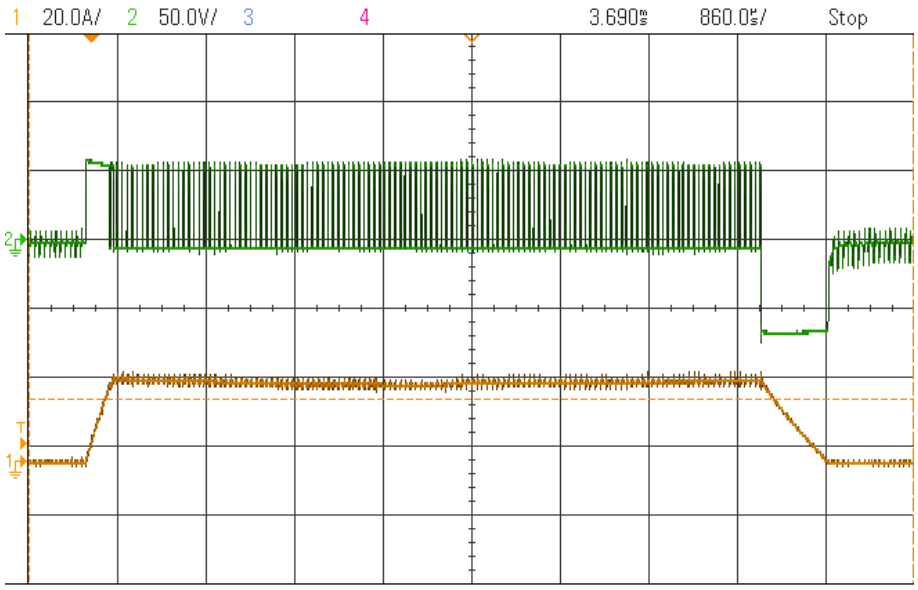

Fig. 25 The motor experimental voltage and current at 200 rpm.

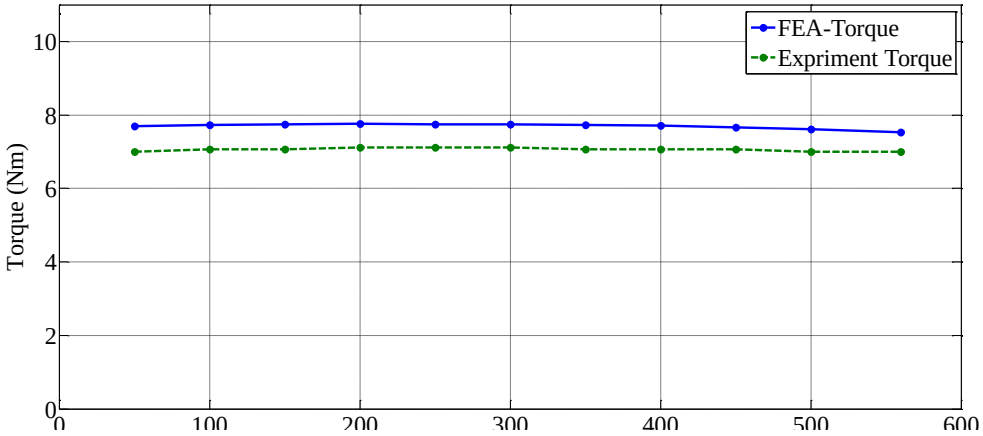

Fig. 26 Torque-Speed characteristics at 25 A, in FEA and experiment.

3.6 Discussion and Conclusion

From the aforementioned explanation, the traditional designed SRM geometry is used for initialization of the proposed optimization framework along with heuristic technique in order to achieve an optimal design parameters and firing angles simultaneously. The motor output characteristics summary is given in Table 7. This motor did not initially meet the application requirements according to Table 3 in terms of average torque and output power as well as the torque ripple which was fairly high. Due to the significant effect of the firing angles on the SRM output characteristics, therefore the transient optimization of firing angles along with the SRM geometry is considered in this chapter. The optimal motor output characteristics are listed in Table 7 that meet the requirements without changing the application constraints. Furthermore, the optimal motor has lower rotor inertia and weight although it has higher torque according to Table 5 and Table 7. Then the machine is manufactured according to the obtained optimal specifications. The optimal motor torque has been measured experimentally and the results demonstrated good agreement with the torque-speed characteristics found by FEA. Moreover, the motor inductance is measured and verified the FEA model.

4 TORQUE RIPPLE MINIMIZATION OF SWITCHED RELUCTANCE MOTOR BY SURROGATE-BASED OPTIMIZATION[2]

4.1 Introduction and Motivation

In this chapter, a solution for exploring optimal firing angles of nonlinear current-controlled Switched Reluctance Motors (SRMs) is proposed in order to minimize the torque ripple. Motor torque ripple for a certain electrical load requirement is minimized using a surrogate-based optimization of firing angles by adjusting the motor geometry, reference current, rotor speed and dc bus voltage. Surrogate-based optimization is facilitated via Neural Networks which are regression tools capable of learning complex multi-variate functions. Flux and torque of the nonlinear SRM is learned as a function of input parameters via the NN, and consequently the computation time of design, which is crucial in any micro controller unit, is expedited by replacing the look-up tables of flux and torque with the surrogate NN model. Comprehensive simulation and experimental results are provided to validate the theoretical findings. In order to minimize the SRM torque ripple, (either) the motor design should be optimized and (or) optimized input current control should be applied. Both approaches were attempted in prior work. In [58-60], the SRM design was optimized to yield low torque ripple, while in [61-63], the SRM drive current controller was optimized to achieve minimum torque ripple. Due to the dependent of the SRM phases commutation periods on θ_{on} and θ_{off}, a promising control

[2] Part of this section has been submitted for publication with B. Anvari, M. Kaya, S. Hajimirza, and H. A. Toliyat, "Surrogate-Based Optimization of Firing Angles for Switched Reluctance Motor," IEEE Transaction on Transportation and Electrification, under revision 2017.

mechanism with minimized torque ripple requires proper turn-on and turn-off angles to achieve smooth commutations. Optimal firing angles were obtained with the correct balance between the criteria of low torque ripple and high efficiency in [64], where a linear model of the SRM was used. In [65], minimum torque rippled was achieved by finding the optimum firing angles with genetic algorithm (GA), but the results were only restricted to numerical simulations. The focus of the current work is on optimizing firing angles for nonlinear model of SRM. The nonlinear SRM flux and torque can only be calculated from extensive 3D Finite Element Analysis (FEA) simulations. Therefore, optimal designs that rely on those underlying computations are extremely time-consuming and limited. Surrogate-based modeling and optimization can alleviate this challenge by modeling the underlying physical output of a system with an approximate data-driven model and use that as an efficient alternative for deriving approximately optimal parameters. Artificial Neural Networks (NN) are powerful regression tools that can learn complex multi-variate functions. We train NNs that approximate flux and torque of nonlinear SRMs as a function of design parameters, and use that to optimize firing angle. The SRM drive is simulated in MATLAB. The motor θ_{on} is obtained by an equation which depends on the motor geometry, dc bus voltage, reference current and speed of the motor. The motor θ_{off} is explored by a heuristic optimization technique with the objective of minimizing the torque ripple with dynamic loads. The obtained data from the proposed optimization as well as the reference current and speed of the motor is analyzed in the surrogate system. Consequently, θ_{off} is represented by a simple surrogate function which expedites the computation process specially in a Digital Signal Processor (DSP).

4.2 NN Modeling for SRM

Surrogate modeling can be achieved by means of regression methods, such as polynomial regression, Kriging and Neural Network (both radial basis function and multilayer perceptron). As with the present study, several previous researchers utilized surrogate modeling for studying torque and flux characteristics. Specifically, a backpropagation and a hybrid backpropagation-genetic algorithm neural network were implemented in [66] and [67] respectively for switched reluctance linear generator to model flux linkage as a function of phase current and mover position. In [68], the authors conducted a fault diagnosis study by establishing a neural network to estimate flux characteristics under faulty and healthy conditions. In [69], a hybrid trained wavelet neural network for current and static torque characteristics was proposed as functions of flux and position and current and position, respectively. The authors in [70] conducted a study for mapping thrust force and position to phase current using another machine learning tool called support vector machines. Torque ripple minimization via surrogate-based optimization has never been attempted to the best of authors' knowledge. In addition, a surrogate explicit representation of optimal θ_{off} can be used to expedite the control of nonlinear SRM in real-time, a novel approach that has not been proposed previously.

A: Mathematical Background of Neural Network

Artificial Neural Networks have the capability to closely approximate functions of arbitrary nonlinearity degree, and are widely used in data classification, pattern recognition, prediction, noisy information processing and more [71]. A Neural network consists of layers of neurons mimicking elements of human brain. Every layer processes

information using simple transform functions and passes the output to the next layer. When sufficient number of data is introduced, it can "learn" and "predict" the output of a given problem for a given input vector, assuming the input-output pair is selected from the same distribution as the training data. A generic two-layer neural network architecture with M input, N neuron in the hidden layer and single output (M-N-1) is presented in Fig. 27.

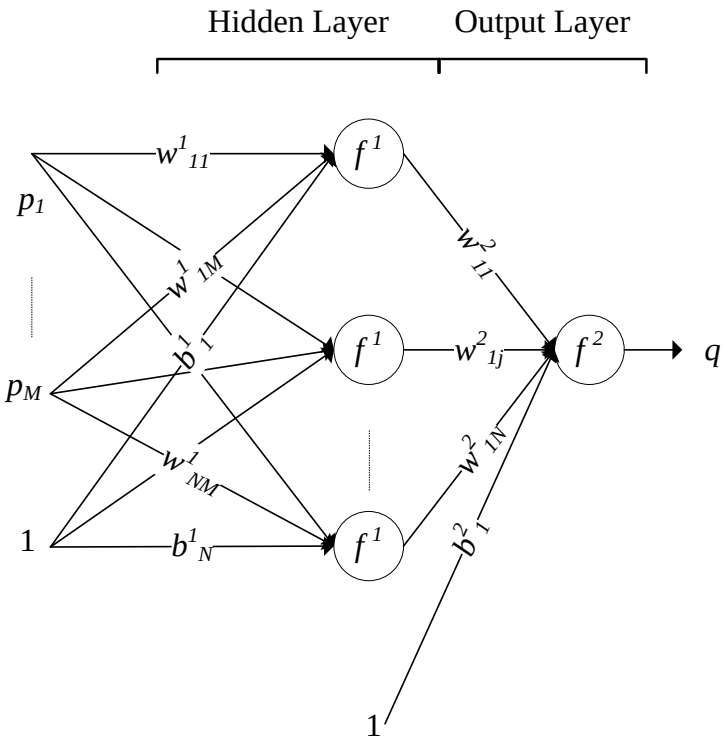

Fig. 27 Two-layer neural network architecture.

The letters on arrows are called weights and bias values (biased are those connected to constant 1 input). The output of NN is expressed as:

$$q = f^2\left(\sum_{j=1}^{N} w_{1j}^2 f^1\left(\sum_{j=1}^{N}\sum_{i=1}^{M} w_{ji}^1 p_i + b_j^1\right) + b_1^2\right) \tag{25}$$

or in matrix form:

$$\mathbf{q} = f^2(W^2 f^1(W^1\mathbf{p} + \mathbf{b^1}) + \mathbf{b^2}) \tag{26}$$

where f^k is the transfer function of the k^{th} layer. There is a variety of transfer functions to be used in NN depending on the problem nature and output space. In the present study, hyperbolic tangent (tanh) is used in both layers. $W^k$is the $R^k \times R^{k-1}$ weight matrix, $\mathbf{b^k}$ is the $R^k \times 1$ bias vector. R^k is the number of neurons in the k^{th} layer ($R^0$is the number of inputs). Number of neurons in the output layer is equal to the dimension of the output vector. NN is trained in order to find the optimum weight-bias vector, **v**:

$$\mathbf{v} = \left[w_{1,1}^1, \dots, w_{N,M}^1, \dots, b_1^1, \dots, b_N^1, \dots, w_{1,1}^2, \dots, b_1^2\right]^{\boldsymbol{T}} \tag{27}$$

Training of the neural network is usually done via a "Backpropagation" algorithm which is an efficient implementation of the gradient descent for minimizing the learning error of the neural network. In this method, the calculated output error over the in-sample (training) data is propagated backwards to adjust the weights of all layers sequentially by means of certain "sensitivity" calculations [72]. Sum of squared error is the most convenient way to express the discrepancy between the desired output (t) and NN output (q). The sensitivity is an expression of the error gradient which is derived for each layer backwards, and is given by the following equations:

$$\mathbf{s}^{\mathrm{L}} = -2\dot{f}^{L}$$
$$\mathbf{s}^{\mathrm{k}} = \dot{f}^{k}(W^{k+1})^{T}\mathbf{s}^{\mathbf{k+1}}, \forall 1 \leq k \leq L-1 \tag{28}$$

where $\mathbf{s}^{\mathrm{k}}$ is the sensitivity of the k^{th} layer, L is the total number of layers, $\dot{f}^{k}$ is the $R^{k} \times R^{k}$ diagonal derivative matrix, and W^{k} is the weight matrix at k^{th} layer. One of the drawbacks to the backpropagation scheme is the possibility of generalization error, or overfitting. This problem can be overcome by utilizing early stopping and Bayesian regularization. Early stopping provides simultaneous observations of out-sample performance of NN by calculating output and the corresponding error on additional data points and merging those with the training performance. This additional set is called the validation set, and training is stopped whenever the validation error starts increasing. Bayesian regularization on the other hand adds a sum of squares of weights regularization term to the cost function in order to force a structure on the weights and biases of the network. Imposing a presumed structure is a recognized method of dealing with the curse of dimensionality and over-fitting in machine learning. The regularized cost function then becomes:

$$F(\mathbf{v}) = \beta\ \mathbf{NMSSE} + \alpha\ \mathbf{SSW} = \beta\mathbf{e}^{\mathrm{T}}\mathbf{e} + \alpha\mathbf{v}^{\mathrm{T}}\mathbf{v} \tag{29}$$

where $\mathbf{NMSSE} = \mathbf{e}^{\mathrm{T}}\mathbf{e}$ is the sum of squared error function and $\mathbf{SSW} = \mathbf{v}^{\mathrm{T}}\mathbf{v}$ is the sum of squared weight-bias vector. α and β are regularization parameters chosen as a function of corresponding errors and number of effective parameters, γ.

$$\alpha = \frac{\gamma}{2\mathbf{SSW}}, \beta = \frac{Q-\gamma}{2\mathbf{NMSSE}} \tag{30}$$

where

$$\gamma = \sum_{m} \frac{\beta\lambda_m}{\beta\lambda_m + 2\alpha} \tag{31}$$

where λ_m is the eigenvalues of the matrix, $G = J^T J$ and $J = \partial \mathbf{e}/\partial \mathbf{v}$ is Jacobian of error. Details of the calculation of Jacobian matrix based on sensitivity values can be found in [72, 73].

Training of Neural Network is an error minimization procedure which could be done by various optimization algorithms. Levenberg-Marquardt (LM) is a Newton-like method widely used as a training algorithm. Although LM is more powerful than other gradient-based methods due to its ability to converge to Steepest Descent or Gauss-Newton [72], its drawback is the possibility of trapping in the local minima. Training for a couple of times with different initial v values and selecting the lowest error is one of the practical solutions. $\mathbf{v_{new}}$ is calculated by:

$$\boldsymbol{\nu}_{\text{new}} = \boldsymbol{\nu} + \Delta\boldsymbol{\nu} \tag{32}$$

$$[\beta J^T J + (2\alpha + \mu)I]\Delta\boldsymbol{\nu} = -J^T \boldsymbol{e} \tag{33}$$

LM algorithm coupled with Bayesian regularization and early stopping (LMB) is schematically displayed in Fig. 28. The LMB algorithm is repeated for different value of R^1 to determine the smallest most efficient network for training purposes.

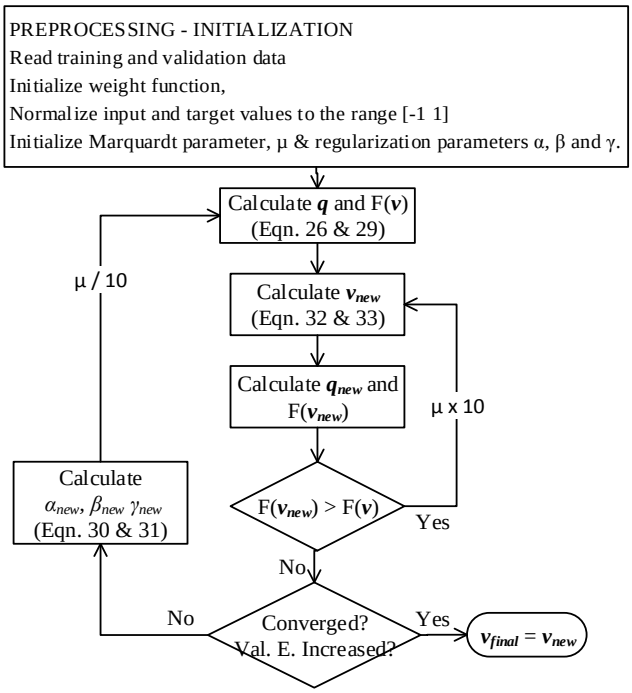

Fig. 28 Flowchart of Levenberg-Marquardt algorithm with Bayesian Regularization and Early Stopping.

B: Neural Network Model for Torque and Flux of the SRM

Following this procedure explained in the previous section, two NN models for replacing torque (T) and flux (ψ) lookup tables as a function of position (θ) and current (i) are constructed.

$$T = NN_T(\theta, i) \tag{34}$$

$$\psi = NN_\psi(\theta, i) \tag{35}$$

In both models, 4000 data vectors are randomly selected from Torque and Flux look-up tables obtained by FEA. Half of these points (2000) are used for training and the other

half for validation. As mentioned earlier, the number of neurons in the hidden layer is determined based on the sum of squared error on training and validation data. In Fig. 29 and Fig. 30, corresponding error values are plotted with respect to number of neurons for torque and flux model respectively. Both networks are selected as 2-8-1 since the decrease in NMSSE is insignificant beyond $R^1 = 8$. Therefore Torque model could be said well-trained and generalizes well $NMSSE = 5.8 \times 10^{-4}$ based on the given data. The same conclusion is applicable to the Flux model with $NMSSE = 1.1 \times 10^{-3}$.

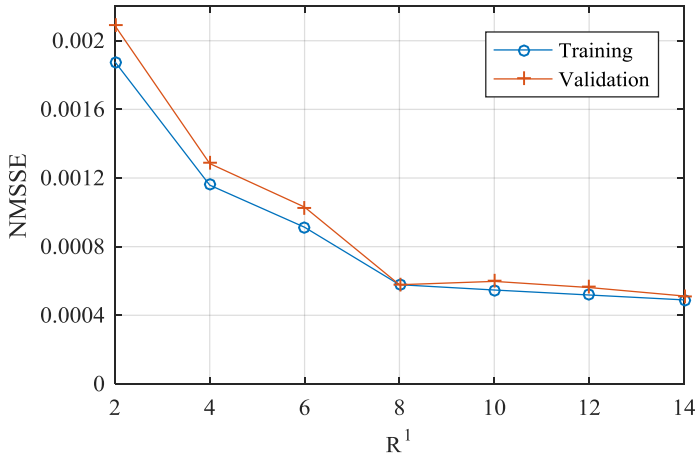

Fig. 29 Normalized mean squared error for training and validation data used for Torque Neural Network (NN_T).

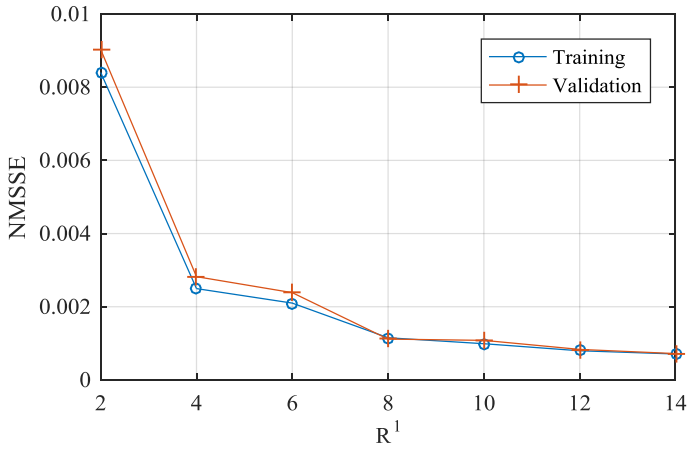

Fig. 30 Normalized mean squared error for training and validation data used for Flux Neural Network (NN_{ψ}).

In Fig. 31 and Fig. 32, the neural network responses for torque and flux characteristics of SRM are plotted with an 8A increments for 0–80A and over the entire position range, and are compared with the simulation results obtained by FEA.

The outputs obtained from NN and FEA are in a good agreement. In the Flux model, maximum percentage error between FEA and NN outputs is 8%, while and in Torque model, maximum percentage error is 10% except when θ is at its minimum and maximum values. The look-up tables can now be replaced by the proposed NN based surrogate models with acceptable accuracy for optimization, and the surrogate models can be used to minimize torque ripple by optimizing firing angles, which will be discussed in the sequel.

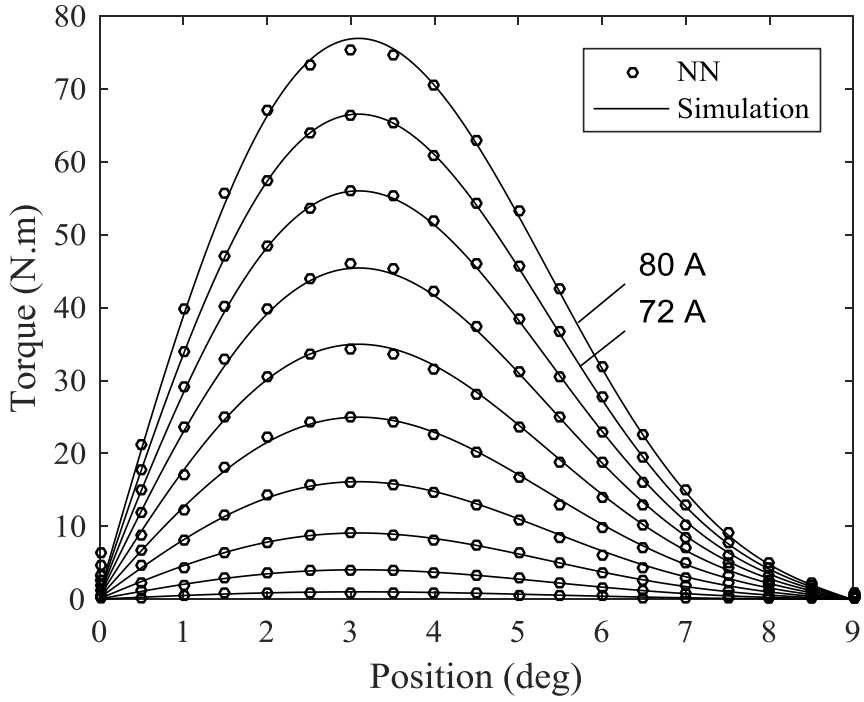

Fig. 31 Comparison of NN output and FEA results for torque for 0 – 9 degree and 0 – 80 A.

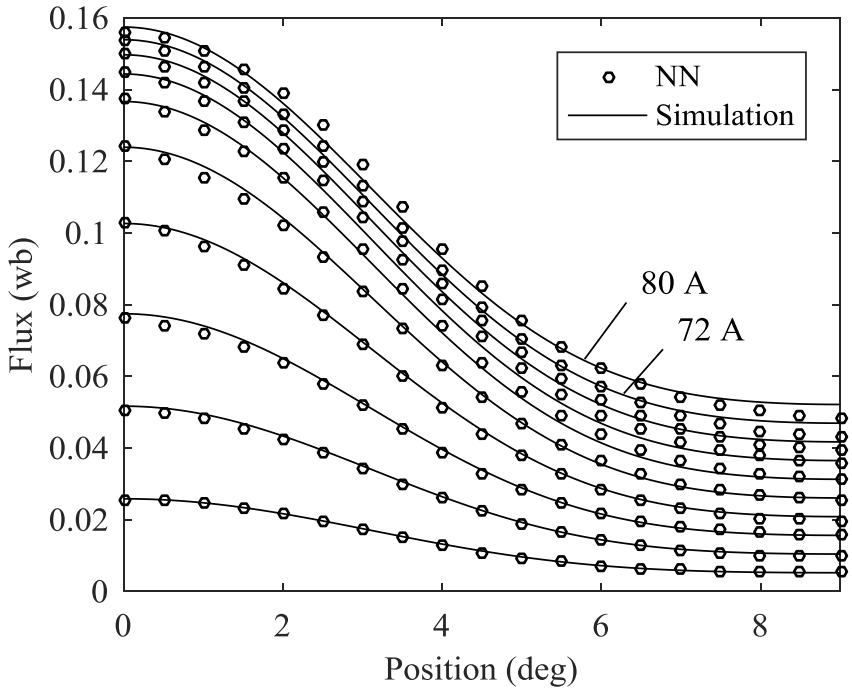

Fig. 32 Comparison of NN output and FEA results for flux for 0 – 9 degree and 8 – 80 A.

4.3 Surrogate Based Optimization Simulation

The SRM is simulated in MATLAB with trained NN models of flux and torque (NN_T and NN_ψ). θ_{on} is yielded from an equation depending on the motor geometry, dc bus voltage, reference current and motor speed, while the optimal θ_{off} is achieved by exhaustive search which will be explained in the next section. Eventually the optimal θ_{off} angles versus reference current and speed are modeled by NN to simplify and expedite the computation process in simulation, as well as on the real-time DSP.

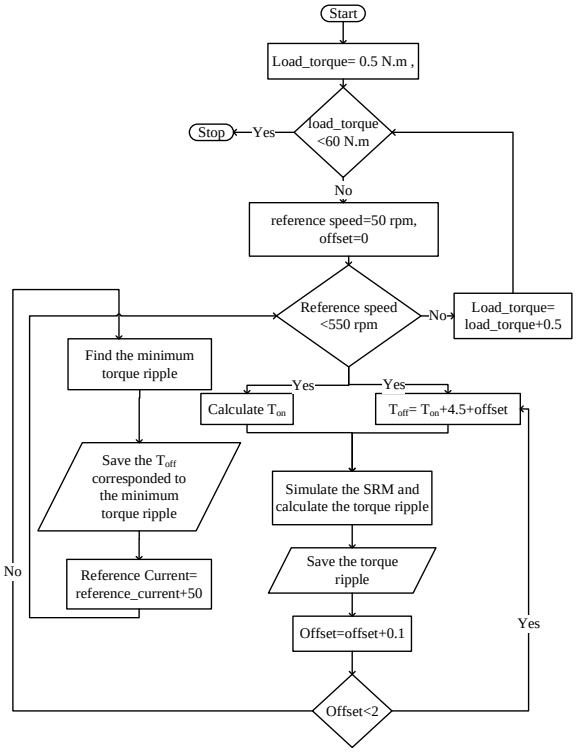

Fig. 33 The θ_{off} angle optimization algorithm.

A: Simulation and Optimization Flowchart

The simulation and optimization procedure flowchart is presented in Fig. 33. Through a two-dimensional exhaustive search, an optimal θ_{off} is explored for any load by scanning the whole load-speed space. The load torque is scanned from 0.5 N.m to 60 N.m with steps of 0.5 N.m and for each corresponded torque value, the reference speed is scanned from 50 to 550 rpm with steps of 50 rpm. For each specified load, θ_{on} is computed by:

$$\theta_{on} = \theta_1 - \frac{360\omega}{60} t_r \tag{36}$$

$$t_r = \frac{L_u I_{ref}}{V_{dc}} \tag{37}$$

where θ_1 indicates the inductance transition point from unaligned region to the positive slope region which is 1.25 ° for the proposed motor. The motor speed denoted by ω which is in rpm. Rising time, t_r, is the time that SRM phase requires to get to the reference current, I_{ref}. The inductance at unaligned position is given by $L_u = 0.63$ mH, and V_{dc} is the voltage of the dc bus. In addition:

$$\theta_{\text{off}} = \theta_{\text{on}} + \theta_{\text{sk}} + \theta_{\text{offset}} \tag{38}$$

$$\theta_{\text{sk}} = \frac{360}{mN_r} \tag{39}$$

where θ_{sk} is the stroke angle of the SRM which is 4.5˚ for the proposed motor, m is the number of motor phases and N_r is the number of rotor poles, given in Table I [74]. θ_{off} varies with the sweep of θ_{offset} from 0˚ to 2˚ with small steps of 0.1˚. θ_{off} corresponding

to the smallest torque standard variation or torque ripple is the optimal θ_{off} of the applied operation condition including load torque and reference speed. Fig. 34 depicts the θ_{off} plotted versus reference current and speed. When reference speed increase, θ_{off} gets smaller, which means the phases should be switched off much earlier than the unaligned position. The same thing is valid at higher reference current or load as well.

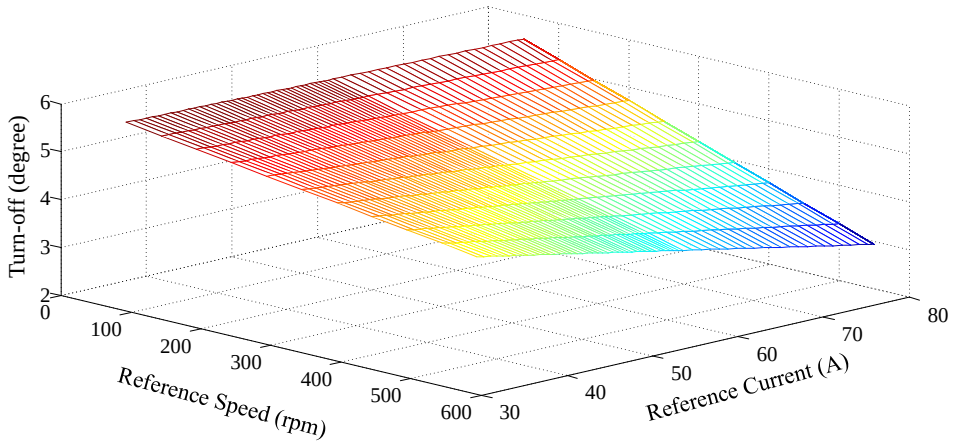

Fig. 34 The θ_{off} angle versus reference current and speed, the color changes from blue to red indicates the increase of θ_{off} angle value.

B: Neural Network model for θ_{off}

Predicting turn off angle precisely is one of the crucial steps for the control of SRM, and the previously explained optimization procedure is effective yet time consuming for real-time control. The real-time optimization procedure could be replaced by the neural network model for optimized θ_{off}, which leads to faster control of SRM. Following the

methodology in Section II-A, the neural network for optimized θ_{off} is to obtain a relationship as follows:

$$\theta_{\text{off}} = NN_T\left(I_{ref}, \omega, \theta_{on}\right) \tag{40}$$

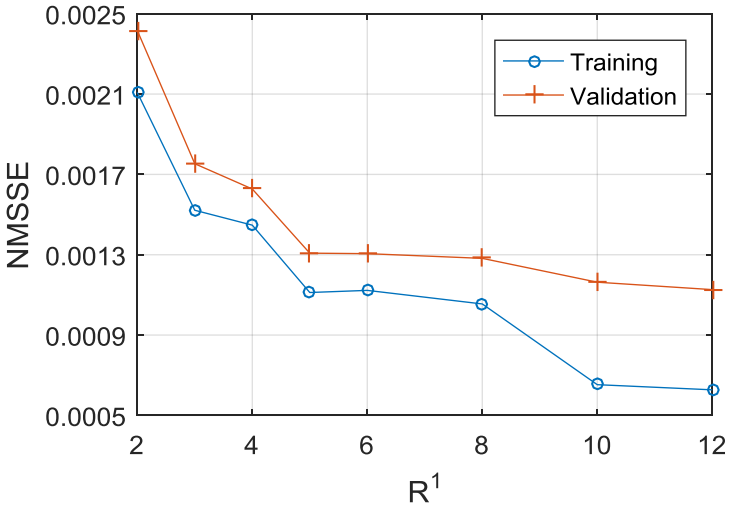

Fig. 35 Normalized mean squared error for training and validation data used for θ_{off} Neural Network.

Training of the network and validation for the future performances are done by randomly selecting 500 data points. Corresponding θ_{off} values are calculated as explained in the previous sections. Number of neurons in the hidden layer of the network, R^1, is set to 5 according to $NMSSE$ values in Fig. 35, since error values no longer decrease although the network gets bigger. Even though training error considerably decreases when R^1 is

10, validation error does not decrease at a comparable rate; therefore, smaller network is preferred per Occam's Razor principle [75].

C: Comparison of NN for θ_{off} and optimization results

The resulting network provides an accurate estimate of optimized turn off angles based on the provided input set. In Fig. 36 and Fig. 37, θ_{off} values from original data set (target) and NN are compared for training and validation sets, respectively. Correlation coefficient, R^2, is 1.00 for training set and 0.99 for validation which means the network generalizes well. The maximum percentage error in training and validation sets are 4%.

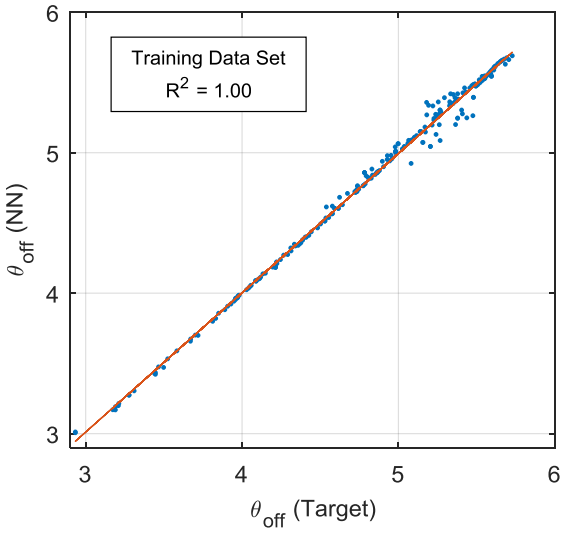

Fig. 36 Comparison of original output and NN response for training data.

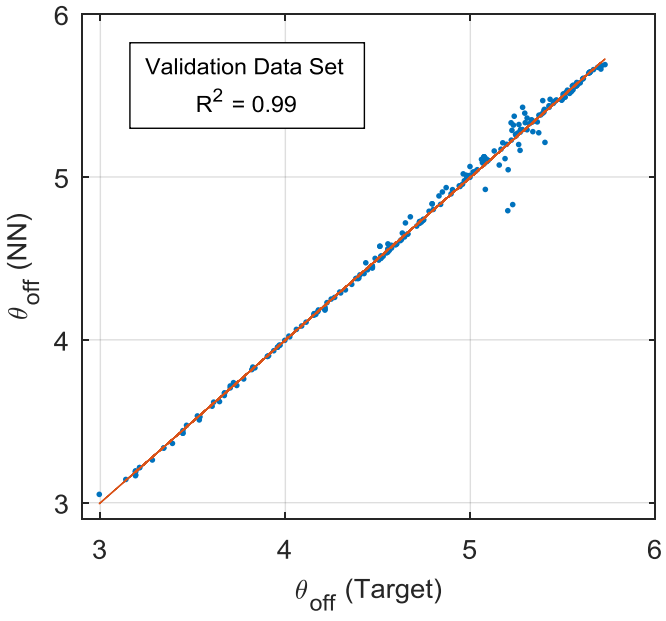

Fig. 37 Comparison of original output and NN response for validation data.

4.4 NN Model of Optimization Results

The simulation block diagram is depicted in Fig. 37. It mainly consists of the four-phase converter, SRM NN models, current controller, speed controller, and a position measurement. A classical PI based control in conjunction with pulse width modulation (PWM) are used to regulate the motor current while the phase is conducting. Soft chopping method is implemented in this paper to reduce the current ripple during the regulation which affects the motor output characteristics, mostly the torque ripple [76].

In order to validate the proposed technique of minimizing the torque ripple, a comparison between un-optimized and optimized simulations are performed. Figs. (38-a), (38-b), (38-c), and (38-d) illustrate the SRM un-optimized simulation results at 200 rpm with load torque of 2.8 Nm: the four phases SRM current, the four phases torque, the

summation of the four phases torque, and the shaft speed respectively with firing angles of θ_{on}=0.5˚ and θ_{off}=6.5˚. The SRM operation with reference speed of 200rpm and load torque of 2.8Nm is simulated with optimal firing angles of θ_{on}=1.03˚ and θ_{off}=5.53˚. Figs. (39-a), (39-b), (39-c), and (39-d) demonstrate the results of phase current, torque, total torque, and speed respectively of the optimized simulation. By having optimal firing angles, current and torque of each phase are rising and falling simultaneously which leads to a low torque ripple. Comparing the total torque with the total torque illustrated in Fig. (38-c), it can be found that torque ripple is reduced significantly. Moreover, the speed response time illustrated in Fig. (39-d) is shorter than the conventional case in Fig. (38-d).

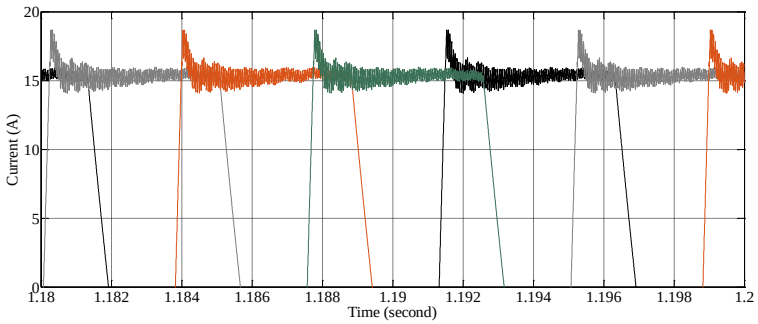

(a)

Fig. 38 The SRM simulation results with unoptimized firing angles; (a): The SRM four phases current versus time. (b): The SRM four phases torque versus time. (c): The SRM accumaltive torque versus time. (d): The SRM speed response versus time.

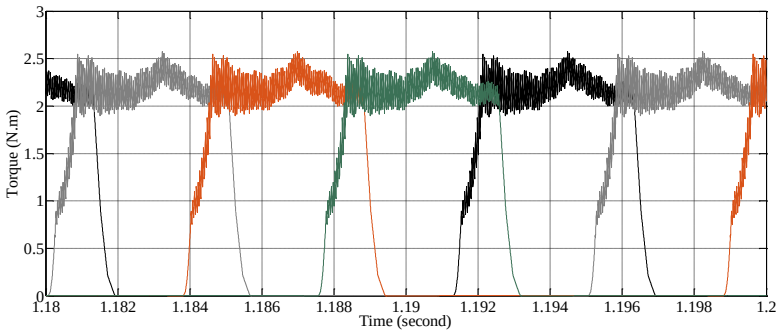

(b)

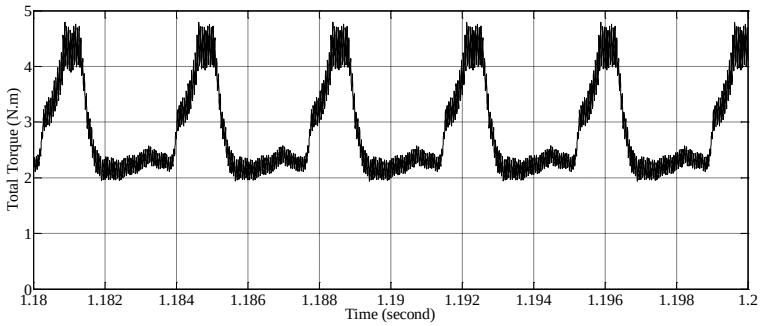

(c)

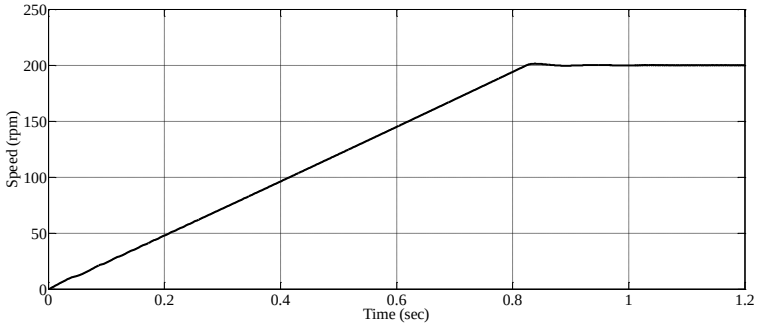

(d)

Fig. 38 Continued.

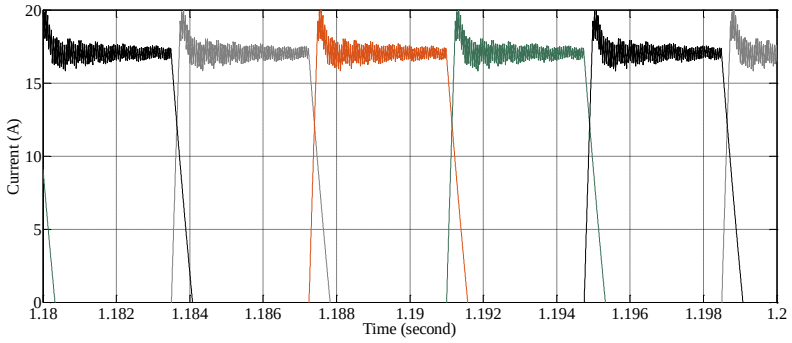

(a)

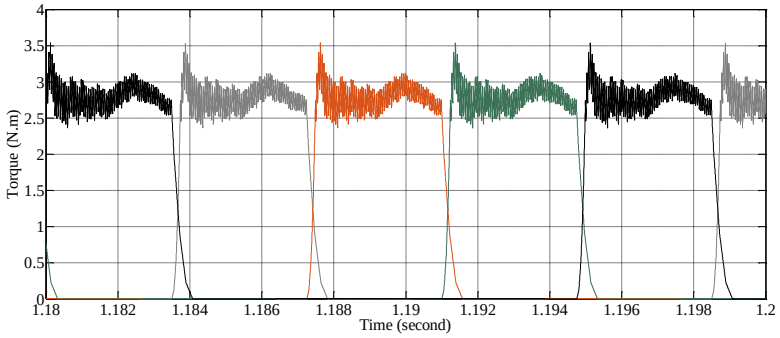

(b)

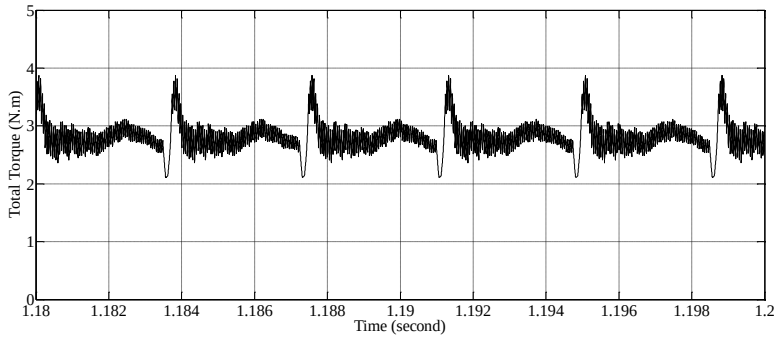

(c)

Fig. 39 The SRM simulation results with optimized firing angles; (a):The SRM four phases current versus time. (b): The SRM four phases torque versus time. (c): The SRM accumaltive torque versus time. (d): The SRM speed response versus time.

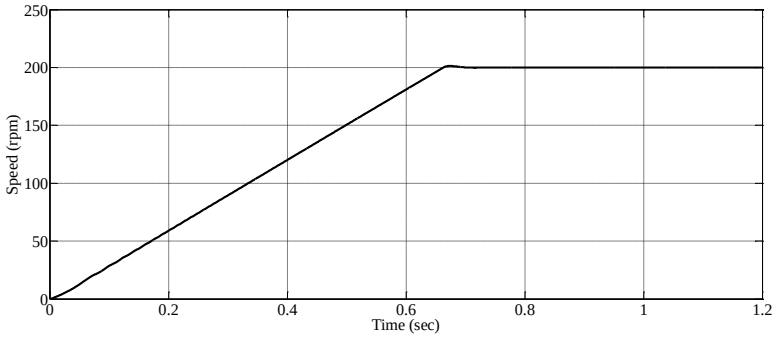

(d)

Fig. 39 Continued.

4.5 Experimental Results

The measured inductances are compared with the inductances obtained with NN analysis in Fig. 40. As shown in Fig. 40, a good agreement is accomplished between the NN model and the experimental measured inductances that confirms the accuracy of the SRM model in the DSP code composer.

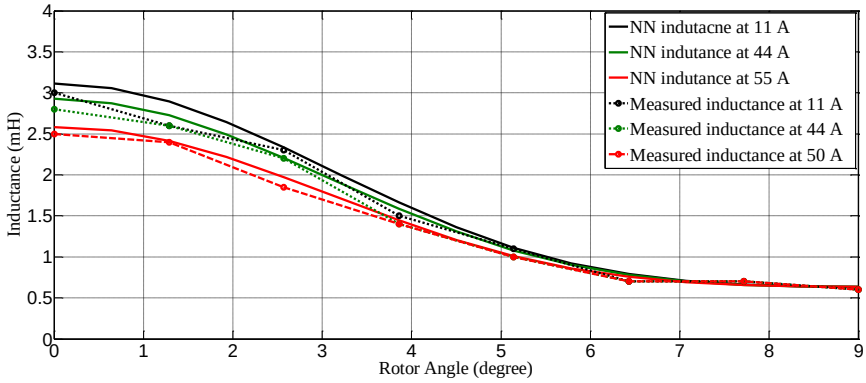

Fig. 40 Motor inductance measurements comparison in FEA with experiment from aligned position (0˚) to unaligned position (9˚).

The same control technique as used in the simulation given in Fig. 33 is implemented in the experimental setup. The instantaneous torque is estimated according to the NN model in DSP. In order to compare the optimized control with the conventional drive, the torque ripple is calculated with 5000 samples of the instantaneous torque in the DSP. To save the calculation time in DSP, instead of using standard deviation, the torque ripple, ΔT is defined as:

$$\Delta T = \sum_{i=1}^{N} \left| T_i - T_{avg} \right| \tag{41}$$

where N is the number of torque samples, T_i is the ith torque sample and T_{avg} is the average torque. To verify the proposed method, the similar operating point as in the simulation i.e. 200 rpm and with load torque of 2.8Nm is tested in the experiment. Fig. 41 demonstrates the estimated output torque when θ_{on}=0.5˚ and θ_{off}=6.5˚. As a comparison, the torque with optimized firing angles calculated by NN model, θ_{on}=1.03˚ and θ_{off}=5.53˚, is illustrated in Fig. 42. The estimated torque in both cases show a good agreement with the simulation results in Fig. (38-c) and Fig. (39-c). According to (42) and Fig. 41 and Fig. 42, the torque ripple is reduced by implementing the optimal firing angles. The average torque measured with the torque meter is 2.8 Nm in both cases that is the same as the estimated average torque in the DSP code composer. These results verify the correctness of the implemented digital control on the DSP and the reduced torque ripple by the proposed technique of exploring firing angles.

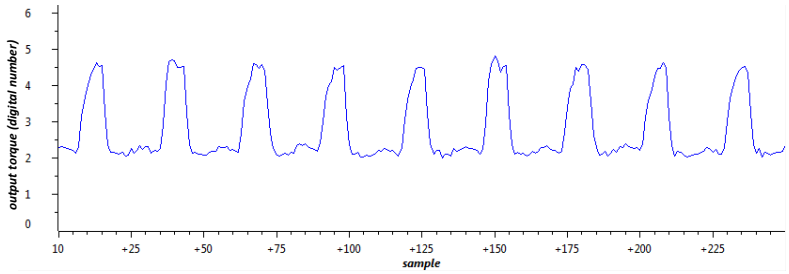

Fig. 41 Estimated output torque with non-optimized firing angles, case 1.

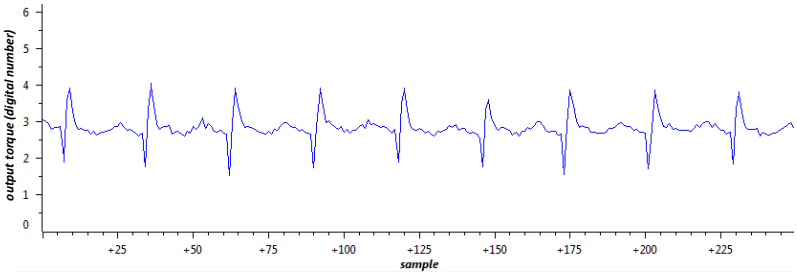

Fig. 42 Estimated output torque with optimized firing angles, case 2.

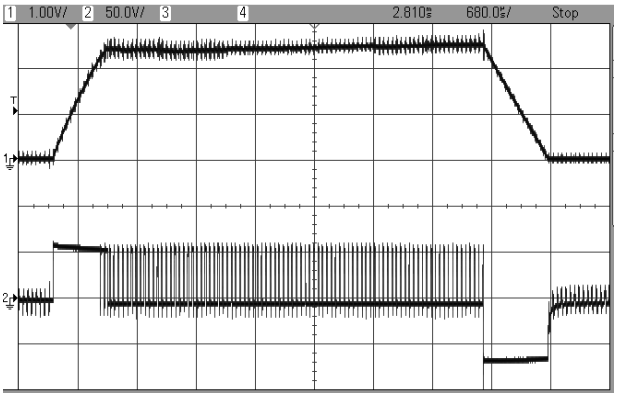

Fig. 43 The SRM phase voltage and current at 200 rpm and load torque of 2.8 Nm.

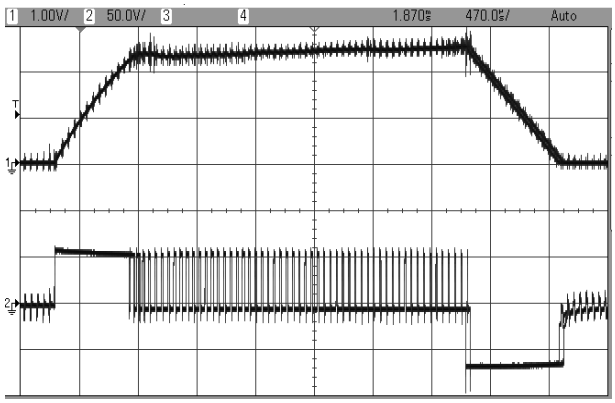

Fig. 44 The SRM phase voltage and current at 300 rpm rpm and load torque of 2.8 Nm.

In order to validate the proposed motor controller, the voltage and current at two different speeds are presented. Fig. 43 demonstrates the experimental motor phase current and voltage labeled as 1-2 respectively at 200 rpm: Voltage on the phase is either positive DC bus voltage or 0 during conducting period. During the phase turn off interval, both switches are off and the phase voltage becomes negative DC bus voltage [76]. Fig. 44 illustrates the experimental motor phase current and voltage at 300 rpm.

4.6 Conclusion and Discussion

In the present study, a surrogate based procedure for optimization of firing angles was proposed in order to minimize the torque ripple of the SRM having dynamic loads. Through a two-dimensional exhaustive search, an optimal θ_{off} was explored for any load by scanning the whole load-speed space. The explored optimized firing angles were then represented using a highly correlated neural network model to expedite and simplify the real-time control of the SRM. The theoretical analysis was verified by simulation as well as experiments.

5 SWITCHED RELUCTANCE MOTOR HEAT TRANSFER MODELING

5.1 Introduction and Motivation

The motor geometry consists of three major parts: rotor, stator and windings. For this motor, the stator is the inner cylinder and the rotor is the outer part. The winding material is copper and the stator and rotor laminations are M19 steel. The simplified geometry is shown in Fig. 45.

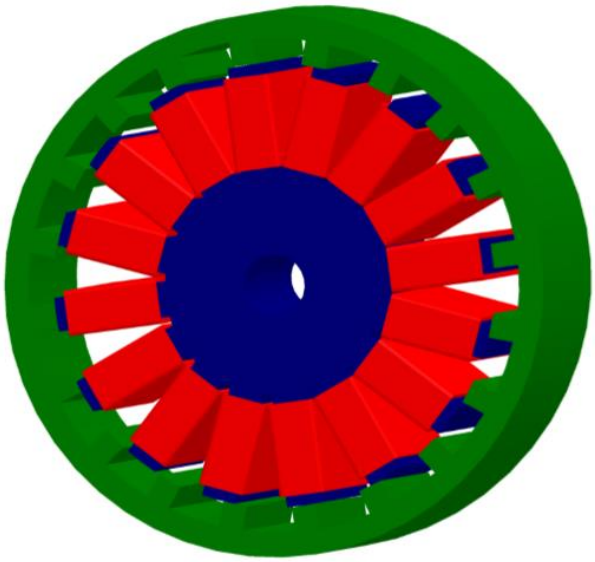

Fig. 45 The simplified model of the proposed SRM.

The governing equation to be solved in the motor is given below:

$$\rho c\frac{\partial T}{\partial \tau} = [\frac{\partial}{\partial x}(k\frac{\partial T}{\partial \tau}) + \frac{\partial}{\partial y}(k\frac{\partial T}{\partial y}) + \frac{\partial}{\partial z}(k\frac{\partial T}{\partial z})] + \frac{\eta I}{\forall} \qquad (42)$$

V

Where is the pseudo-time. It should be noted that although the problem is steady-state, the thermal conductivity k, density ρ and thermal capacity ρ are temperature-dependent and the problem is non-linear which requires for iterative solution and pseudo-time marching. Also convection and radiation introduce non-linearity to the problem through boundary conditions (BC).

Only half of the rotor is modelled since BCs on both sides are similar and by using a symmetry condition at half-length the computational domain reduces by half allowing for a denser grid. We refrain form a periodic modelling like the case done in some publications [77]. This is due to dissimilar number of poles on rotor and stator and also natural convection effects that vary with circumferential position.

A schematic of the boundary conditions used in this problem are given in Fig. 46. Since the shaft is stationary and has the same material as the stator, we merge it with the stator for the steady state heat transfer problem.

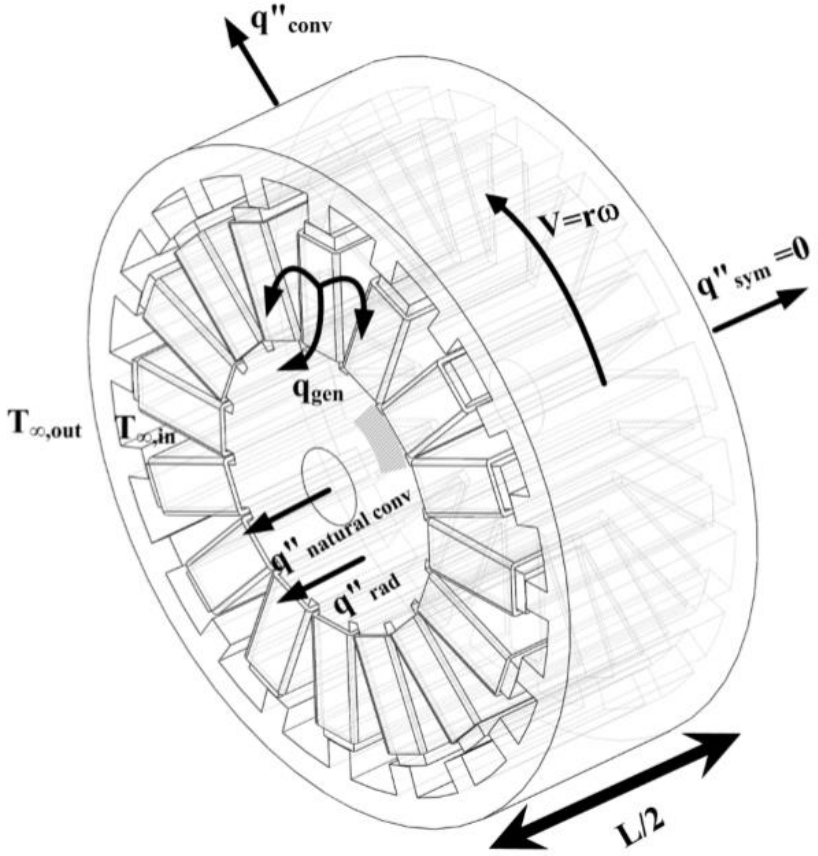

Fig. 46 Boundary conditions of the proposed SRM.

5.2 Convection

The rotor has a rotational speed of 200 rpm and therefore the convection coefficient h for rotor is larger than other parts. We assume the corresponding air convection coefficient with speed of $r\omega$ on the surface of the rotor using the chart shown in Fig. 47 [78]:

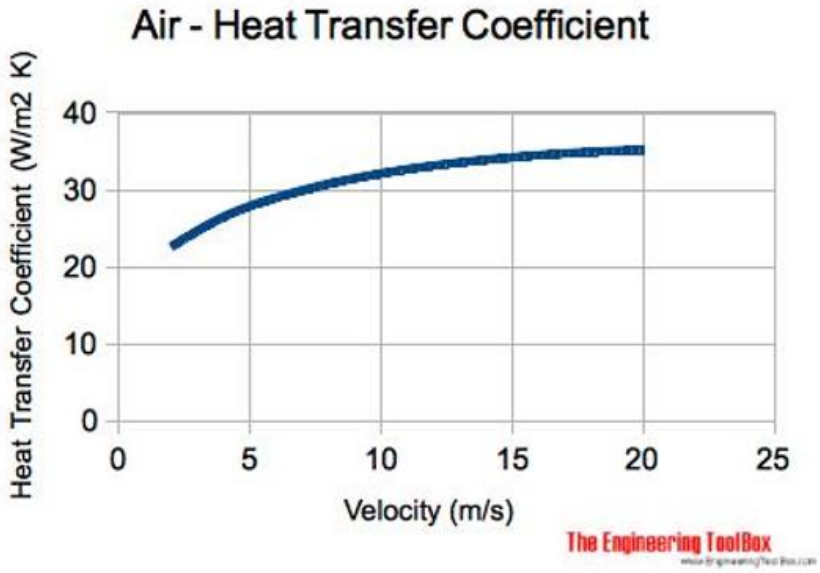

Fig. 47 Air laminar convection coefficient [78].

where v refers to the air speed. An alternative can be the famous Pohlhausen's relation on flat plate laminar convection coefficient [79]:

$$Nu = 0.664 \mathrm{Re}^{0.5} \mathrm{Pr}^{0.33} \tag{43}$$

The stator and winding are stationary and therefore a natural convection boundary condition applies to them. We use a simplified natural convection relation for winding and stator where $h \sim 5\ W/r2k$. Alternatively, we could use horizontal cylinder and vertical plate natural convection for stator and plate, yet given to the small dimensions and low

temperature gradients, these effects are minimal and can be safely dropped. These coefficients are provided as in-built functions in ANSYS Thermal solver.

5.3 Inside Ambient Temperature

Two end-caps will close the sides of motor, these caps are not modeled in this study. However, the caps have other fairly important impact on what is happening inside the motor. The air temperature inside the motor differs from the room temperature outside the motor because the air inside the motor is almost isolated from the outside air by end caps. The inside temperature of rotor can be determined using two methods*:*

a) One way is to assume the same temperature as outer temperature of rotor since the rotor is thin and separated from the winding. From conduction relation in a cylindrical wall we have [80]:

$$T = T_{r,out} + \frac{\dot{q}_{gen} r_{out}^2}{4k}\left(1 - \frac{r^2}{r_{out}^2}\right) - \left[\frac{\dot{q}_{gen} r_{out}^2}{4k}\left(1 - \frac{r_{in}^{\ 2}}{r_{out}^2}\right) + (T_{r,out} - T_{r,in})\right]\frac{In(r_{out}/r)}{In(r_{out}/r_{in})} \tag{44}$$

Which reduces to following relation because the internal generation is not present in rotor.

$$T = T_{r,out} + (T_{r,out} - T_{r,in})\frac{In(r_{out}/r)}{In(r_{out}/r_{in})} \tag{45}$$

Knowing that $r_{in} = 100\ mm$ and $r_{out} = 114\ mm$, then we are operating at ratio $r_{out}/r_{in} = 1.14$ which is very close to 1 and basically means $T_{r,in} = T_{r,out}$. We use balance of energy to estimate the air temperature inside neglecting radiation coming from stator:

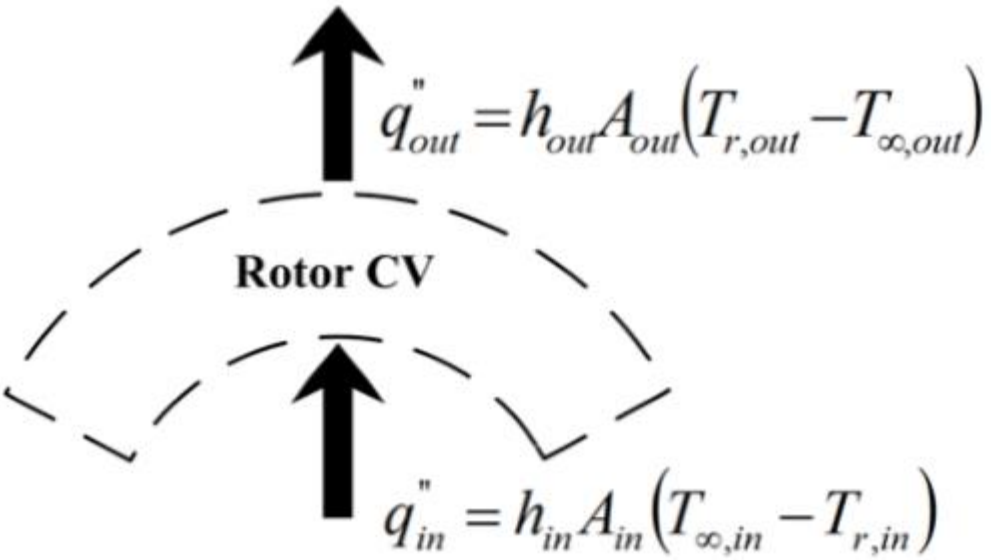

Fig. 48 Radiation distribution.

The balance of energy is written for unit length of the CV:

$$\ddot{q}_{in} - \ddot{q}_{out} - \dot{q}_{gen} = \rho c \frac{dT}{dt} \tag{46}$$

Since problem is steady and there is no heat generation in the rotor the equation simplifies to:

$$\begin{aligned} &\ddot{q}_{in} = \ddot{q}_{out} \rightarrow \\ &h_{out} A_{out} (T_{r,out} - T_{\infty,out}) = h_{in} A_{in} (T_{r,in} - T_{\infty,in}) \end{aligned} \tag{47}$$

In (47), both convection coefficients are known, as well as surface areas. Outside air temperature is known and outside rotor temperature is also known from thermal readings. Solving for inside ambient temperature:

$$T_{\infty,in} = T_{r,in} + \frac{R_{r,out}}{R_{r,in}} \frac{h_{out}(T_{r,out} - T_{\infty,out})}{h_{in}} \tag{48}$$

This option only works when winding temperature is low and radiosity does not cause deviation.

b) It can be found from a try and error procedure where inner ambient temperature is changed to match the outer rotor temperature from numerical simulation with experimental results. This approach is better suited for high temperature simulations.

5.4 Ohmic Heat Generation

As regards the heat source, the winding generates uniform volumetric heat. To find the correct density of heat generation it is crucial to know both Ohmic loss and the accurate volume of the winding. The efficiency of the motor is about 91% and the rated current and voltage are 60 A, 80 η, respectively; therefore, if we assume almost all of the loss relates to ohmic loss, we have:

$$\dot{Q}_{gen,w} = (1-\eta)IV = 432[W] \tag{49}$$

Also the Ohmic loss from Maxwell simulations are about 400 W which supports our assumption. But in laboratory condition it is not possible to work beyond 25 A and 20 η

and the generated power will be $\dot{Q}_{gen,w} = 45W$. The volume of the actual copper part of the winding is crucial to the modelling:

$$\dot{q}_{gen.new} = \frac{\dot{Q}_{gen,w}}{\forall}[W/m^3] \tag{50}$$

What is more, the actual CAD dimensions should not give a larger or smaller volume than reality, otherwise the total heat generation and its distribution will be altered. Current CAD modeling does not have accurate winding dimensions since winding assembly step has been done by the manufacturer. The estimation is about 723348 mm^3. Hence, for our test condition:

$$\dot{q}_{gen.new} = 62{,}210W/m^3 \tag{51}$$

5.5 Radiation

Radiation is automatically considered by the software wherever temperature is significant. It should be noted that radiation effects may not be dropped for stator surfaces where surface temperature is high and convection coefficient is fairly low. The following table shows how these fluxes compare together for our application.

Table 8 Radiation versus conversion [81]

T_{surf} [K] h [W/m^{2}K]	10	100	1000	2000
325	69.3%	6.9%	0.7%	0.3%
350	78.3%	7.8%	0.8%	0.4%
400	99.2%	9.9%	1.0%	0.5%
1000	803.4%	80.3%	8.0%	4.0%
2000	5333.7%	533.4%	53.3%	26.7%

From the Table it can be understood that in stator temperature range (T~$325-350K$) and stator convection coefficient range (h ~5 W/m^2K), radiation may be even more decisive than convection.

5.6 Viscous Dissipation

The heat generated by the rotor friction with air is minimal on the outer surface and neglected. After writing 2D polar N-S for a long rotating cylinder and simplifying axisymmetric terms we reach at:

$$\frac{\partial(ru_r)}{\partial r}=0\rightarrow u_r=\frac{C}{r}$$
$$\frac{\partial^2 u_\theta}{\partial r^2}+\frac{1}{r}\frac{\partial u_\theta}{\partial r}(1-\frac{C}{\nu})-\frac{u_\theta}{r^2}(1+C)=0 \quad (52)$$
$$\frac{\partial\rho}{\partial r}=\rho(\frac{u_\theta^2}{r}+\frac{C^2}{r^3})$$

At cylinder wall NR=0 therefore C=0 and Nr=0. Now our equations simplify to:

$$\frac{\partial^2 u_\theta}{\partial r^2}+\frac{1}{r}\frac{\partial u_\theta}{\partial r}-\frac{u_\theta}{r^2}=0$$
$$\frac{\partial\rho}{\partial r}=\rho(\frac{u_\theta^2}{r}) \quad (53)$$

The equation to be solved for $N\theta$ is a simple Euler-Cauchy equation and has the solution form:

$$u_\theta=Ar+\frac{B}{r} \quad (54)$$

Applying BCs at cylinder wall $u_{\theta,R}=R\omega$ and infinity $N_{\theta,\infty}$=0:

$$u_\theta=\frac{R^2\omega}{r} \quad (55)$$

The viscous dissipation in cylindrical coordinate is written as:

$$u\Phi_v = \mu\{2[(\frac{\partial u_r}{\partial r})^2 + (\frac{1}{r}\frac{\partial u_\theta}{\partial \theta} + \frac{u_r}{r})^2 + (\frac{\partial u_z}{\partial z})^2] + [r\frac{\partial}{\partial r}(\frac{u_\theta}{r}) + \frac{1}{r}\frac{\partial u_r}{\partial \theta}]^2 + (\frac{1}{r}\frac{\partial u_z}{\partial \theta} + \frac{\partial u_\theta}{\partial z})^2 + (\frac{\partial u_r}{\partial z} + \frac{\partial u_z}{\partial r})^2 - \frac{2}{3}(\nabla.u)^2\} \quad (56)$$

For current flow it reduces to:

$$u\Phi_v = \mu[r\frac{\partial}{\partial r}(\frac{u_\theta}{r})]^2 = 9\mu(\frac{R}{r})^4\omega^2 \quad (57)$$

Which is most significant at the cylinder surface $r=R$ and for air with dynamic viscosity $\mu=2\times10^{-5}\ Pa\,s$ the viscous dissipation for the outer side of rotor will be:

$$u\Phi_v = 9\times2\times10^{-5}\times20.94^2 \cong 0.08\frac{W}{m^3} \quad (58)$$

Which barely changes the temperature of surrounding air. For inside almost all the terms of dissipation remain; However, still air dynamic viscosity $\mu=2\times10-5\ Pa\,s$ is too small to generate appreciable heat at low rotational speed of 200 *rpm.*

5.7 Thermal Camera Readings

The thermal readings have been acquired using Fluke Ti45 thermal camera. The ambient temperature was read by lab thermostat $T_{\infty,\text{out}}=24°C$. The emissivity of gray-white background imaging is normally between 0.9−0.95. The metal box and laminated M19 steel have rough surfaces and have less reflectivity and should be treated as low temperature rough steel plate. Considering all these aspects emissivity was selected as 0.92 [82, 83]. The motor was working with voltage of 20 V and current of 25A and took almost 90 *minutes* to reach steady-state condition. The reading below was taken at stead-

state condition and shows the surface temperature of $T_{\infty,\text{out}}$=31.5°C. The box has been drawn to select a surface area that is normal to camera and then averaged to minimize the errors.

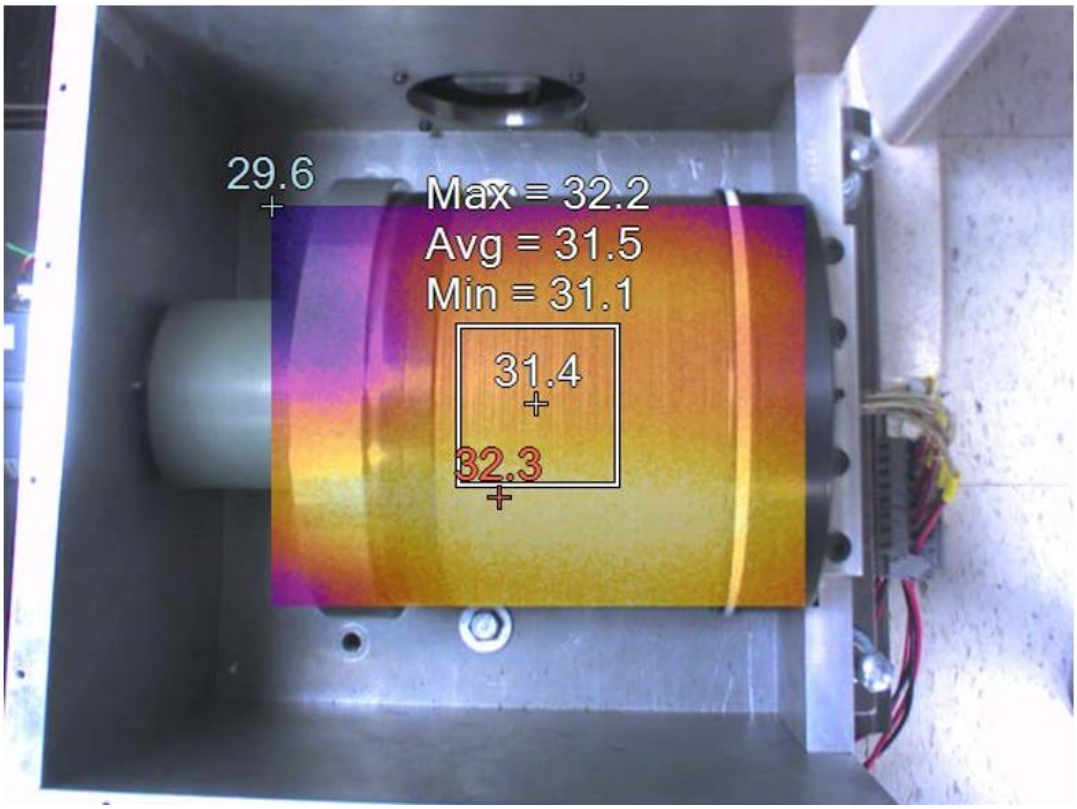

Fig. 49 Thermal camera reading.

5.8 Steady-State Thermal Simulation

The following automatic structured mesh has been generated for the domain. Further mesh refinement does not change the solution results. The cross section view confirms the quality of inside elements. This grid has a total nodes of 1,270,000 and total elements of 250,000.

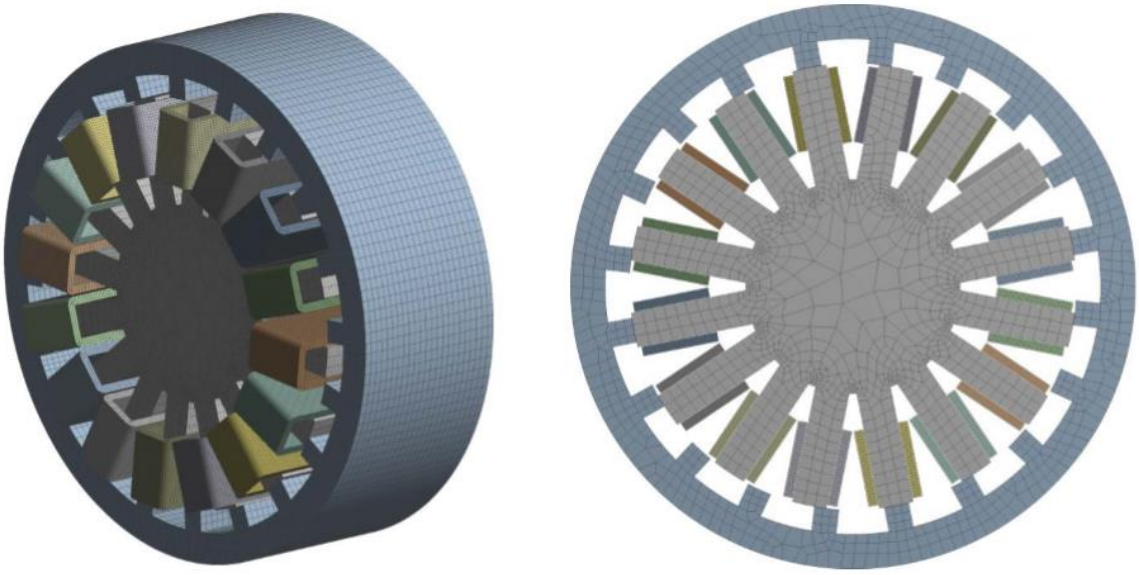

Fig. 50 Meshing on the motor.

The inside ambient temperature $T_{\infty,\text{out}}$=35°C was set by try and error to match the rotor external temperature with experiments. The estimation of air temperature inside motor neglecting radiation predicted $T_{\infty,\text{out}}$=40.9°C ∘C which implies radiation cannot be dropped inside motor. The steady state temperature is shown in Fig. 51.

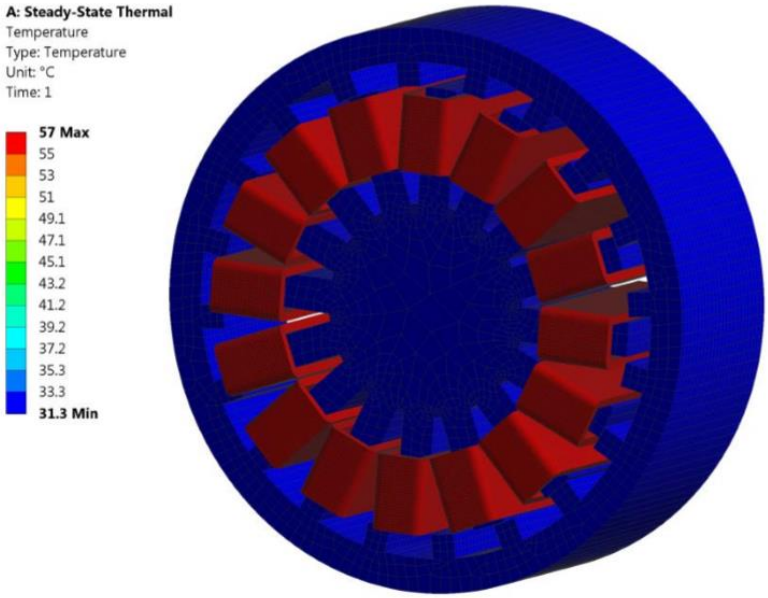

Fig. 51 Steady state thermal analysis.

Note that there is a large gap between winding and other parts' temperature, since convection and radiation are the only effective mechanisms here. A more realistic modelling requires information (thermal and geometrical) about the insulation paper between winding and stator. Adding that feature allows conduction heat flow between solid stationary parts. Although, if the insulation paper has a very low conductivity, the thermal distribution will not be affected much. To have a better vision on thermal distribution in parts other than winding separate contours have been plotted. The contours support the assumption of similar temperatures on the inside and outside surfaces of the rotor.

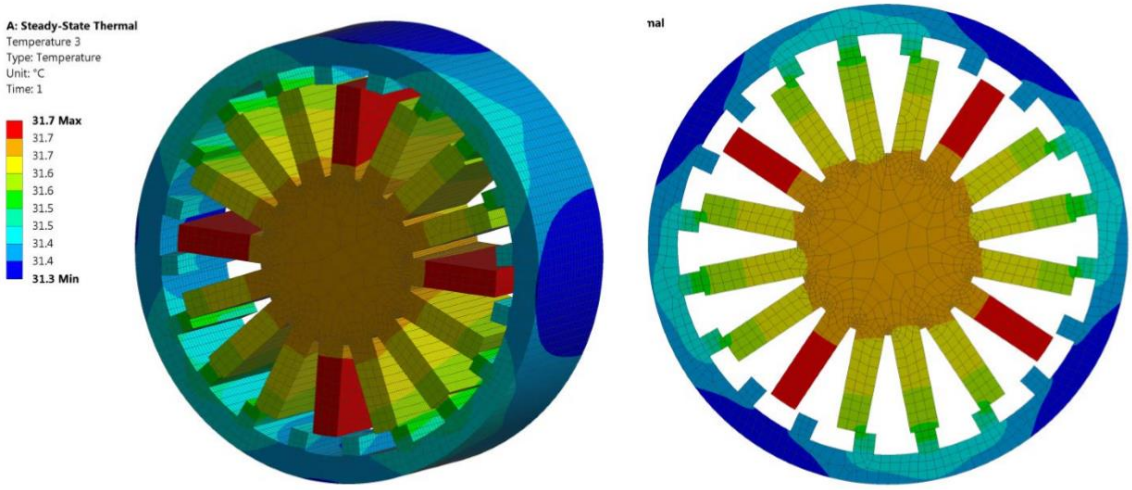

Fig. 52 Steady state thermal analysis.

5.9 Conclusion and Discussion

The motor steady state thermal analysis has been provided in this chapter. The experimental results as well as the simulation has been presented. To improve simulations following tasks can be done:

-Include the insulation layer between winding and stator poles. -Include end-caps in model. -Measuring ambient temperature inside the motor. -Transient simulations using coupled Maxwell-Thermal solver of ANSYS which updates load and thermal distribution at each time. The solution is more expensive but does not require knowledge of ambient temperature inside. $T_{\infty,\text{out}}$ can be updated by considering radiation effects from known winding temperature at the end of each iteration.

6 A CORELESS PERMANENT-MAGNET MACHINE FOR A MAGNETICALLY LEVITATED SHAFT-LESS FLYWHEEL[3]

6.1 Introduction and Motivation

This dissertation proposes a framework for the design and analysis of a coreless permanent magnet (PM) machine for a 100 kWh shaft-less high strength steel flywheel energy storage system (SHFES). The PM motor/generator is designed to meet the required specs in terms of torque-speed and power-speed characteristics given by the application. The design challenges of a motor/generator for this architecture include: the poor flux paths due to a large scale solid carbon steel rotor and zero-thermal convection of the airgap due to operation of the machine in vacuum. Magnetic flux in this architecture tends to be 3-D rather than constrained due to lack of core in the stator. In order to tackle these challenges, several other parameters such as a proper number of magnets and slots combination, wire thickness, number of turns in each coil, magnets with high saturated flux density and magnets size are carefully considered in the proposed design framework. Magnetic levitation allows the use of a coreless stator that is placed on a supporting structure. The proposed PM motor/generator comprehensive geometry, electromagnetic and mechanical dimensioning are followed by detailed 3-D finite element analysis (FEA). The torque, power, and speed determined by the FEA electromagnetic analysis are met by the application design requirements and constraints for both the charging and discharging

[3] Part of this section is reprinted with permission from B. Anvari, Xiaojun Li, Hamid A. Toliyat, Alan Palazzolo, Zhiyng Wang, and Xu Han, " A coreless permanent-magnet machine for a magnetically levitated shaft-less flywheel," 2017 IEEE International Electric Machines and Drives Conference (IEMDC), Miami, FL, 2017, pp. 1-7.

modes of operation. Furthermore, the design and analysis of the coil holding structures are discussed. Finally, the motor/generator static thermal analysis is discussed in order to validate the proposed cooling system functionality.

Fig. 53 The Texas A&M shaft-less flywheel-CAMB assembly.

Flywheel energy storage system (FESS) has reemerged as a viable solution to applications such as uninterruptable power supply (UPS), frequency regulation in power grids, electrified transportation, renewable energies and pulsed power loads [84]. Comparing to lithium-ion batteries, flywheels typically have much higher life cycles, depth of discharge, and lifetime of service [85]. They are less sensitive to ambient

temperatures and have minimal environmental impact [84]. In order to reduce any mechanical friction loss, FESS often includes an active magnetic bearing. An electrical machine and bi-directional converter are required to convert the electricity to mechanical energy and vice versa. Permanent-magnet machine is favorable option for flywheel motor/generator for their high efficiency. Texas A&M University is developing a coreless permanent-magnet motor/generator for a magnetically levitated shaft-less, large scale flywheel with a weight of 5443 kg [86]. The flywheel has a potential of double energy density comparing to conventional design. Fig. 53 demonstrates the developing flywheel system, as shown in Fig. 1, its large disk shape wheel is being levitated against the earth's gravity by permanent magnets (PM) magnetic field. Conventional magnetic bearing systems are not applicable to the shaft-less flywheel due to the fact that they need a shaft for operation. A novel combination magnetic bearing (CAMB) that can offer 5 axis levitation is designed to provide full magnetic suspension for the developing flywheel [86]. The key design parameters of the flywheel and its combination active magnetic bearing (CAMB) are given in Table 9.

PM motor/generator is the prevailing option for many applications such as wind turbine, pump, and flywheel applications due to its high torque density comparing to the other types of motors [87-94]. Using coreless PM machines has increased significantly in recent years particularly for large scale and variable speed applications [95-97]. A new methodology for the design of coreless PM machine is proposed in [98]. The proposed method includes comprehensive optimization of a coreless PM machine having concentric rotor and stator arrangement. For flywheel applications, in order to control the suspension

force, a coreless stator type bearing-less motor/generator is proposed in [99]. The Authors proposed an air-core PM motor/generator design with a new winding arrangement. However, it lacks thermal analysis which is crucial for PM motor/generator design for flywheel application due to operation of flywheel in vacuum.

Table 9 Flywheel and Magnetic Bearing Specifications

Parameter Name	Quantity	Unit
Flywheel outer diameter	2133	mm
Flywheel height	203	mm
Flywheel weight	5443	kg
Flywheel material	4340	-
Flywheel relative permeability	200	-
Magnetic bearing outer diameter	1106	mm
Magnetic bearing height	165	mm
Magnetic bearing weight	544	kg
Magnet bearing material (AISI)	1018	
Magnetic bearing relative permeability	1000	-
Magnetic bearing saturation flux density	0.7	T

This chapter presents the use of a coreless or ironless stator and a magnetic bearing levitated flywheel, thus the winding can be placed on a stationary structure. The propped

design is identical comparing to the existing coreless machines design structures for operation in vacuum and having the holding structure on the ground. The Fixed windings onto the base through holding structures located on the ground has high strength, reliability and simple mechanical design in terms of manufacturing and maintenance. The proposed design of PM motor/generator for an existing flywheel with specific requirements is presented in [100]. The cooling system functionality of the machine is presented in this chapter by adding thermal analysis of the machine.

6.2 Fundamentals of Flywheel Energy Storage

The power, speed and torque requirements are illustrated in Fig. 54. The rated speed (ω-rated) is 5000 rpm, the rated torque (T-rated) is 191 N.m, and the rated power (P-rated) is 100 kW. The required time for the flywheel to be charged up to the rated speed in the motoring mode is labeled by t1. During this period, the flywheel input power and speed are increasing to the rated power and rated speed of 5000 rpm. During t1 to an arbitrary time t2, the flywheel spins with the minimum power and torque, indicated by P1 and T1 respectively, in the vacuum at constant speed of 5000 rpm. The flywheel operates in the generating mode of operation during t2 to t3 and is discharged with constant power while its speed is decreasing from rated value down to ω1 rpm. Time intervals t1 and t3 can be easily found from rotational kinetic energy (ΔE) and the relation between power and energy as follows:

$$\Delta E = \frac{1}{2} J(\omega_1^{\,2} - \omega_2^{\,2}) \tag{3}$$

$$P_{average} = \frac{\Delta E}{(t_3 - t_2)} \tag{4}$$

where the moment of inertia J is 3089 kg.m^2, ω_1 and ω_2 represent the initial and final speeds respectively.

In an ideal case, the required time for the flywheel to get to 5000 rpm with the average power of 50 kW is 2 hours and 35 minutes which is labeled by $t1$ in Fig. 54. Thus, the rated energy of the proposed flywheel is 100 kWh and is demonstrated by the time sector $t3-t2$. The generators should supply constant power of 100kW; by using (3) and (4), the ω_1 is calculated to be 1928 rpm consequently. The proposed motor/generator is able to generate 100 kW constant power while the speed is decreasing from 5000 to 1928 rpm. Time $t2$ can be any arbitrary time according to energy storage requirement. Additionally, there might be some limitations on $t2$ due to the operation of the flywheel in vacuum condition.

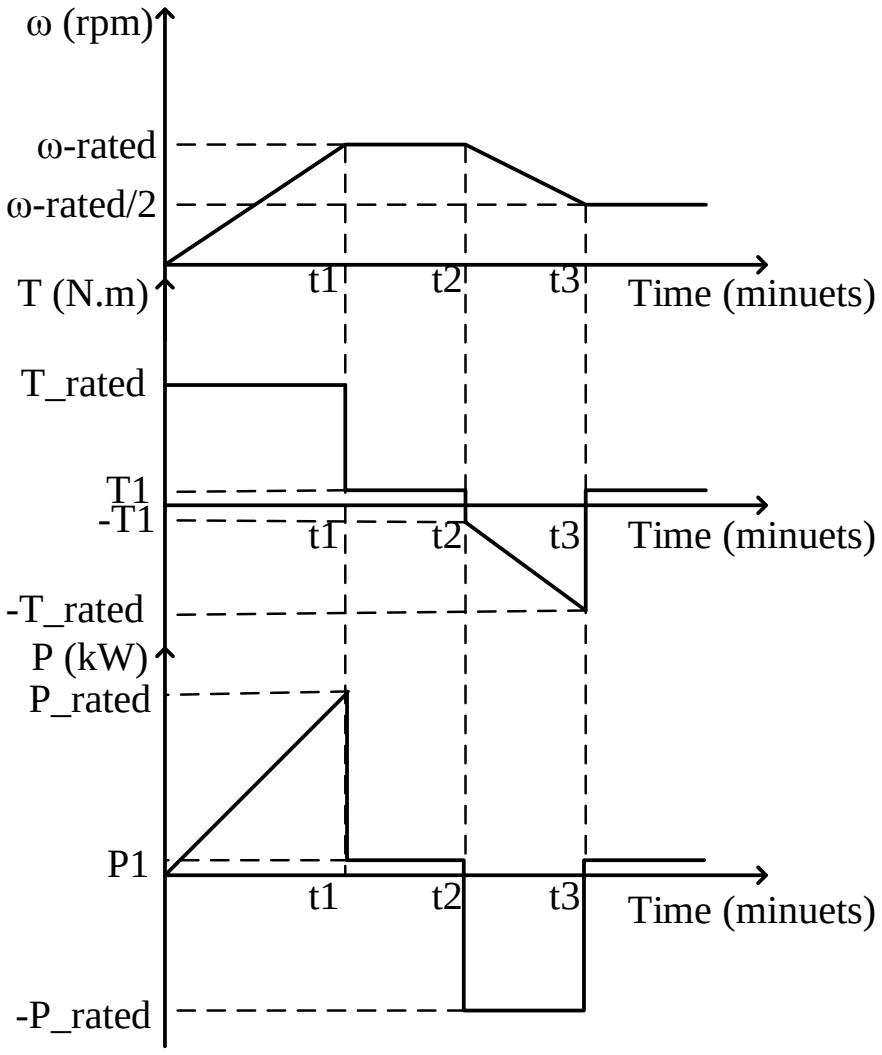

Fig. 54 Design requirements.

Fig. 55 displays only two poles of the proposed PM motor/generator in three dimensional (3D) FEA. The PM motor/generator is shaft-less and consists of a coreless stator. The motor/generator consists of a rotor with a groove of 50 mm height. The magnets, with 25 mm height and 15.54 mm width are mounted on the inner surface of the

groove and coreless windings are fixed onto the base through holding structures. The side view of the groove including magnet and coil are illustrated in Fig. 56.

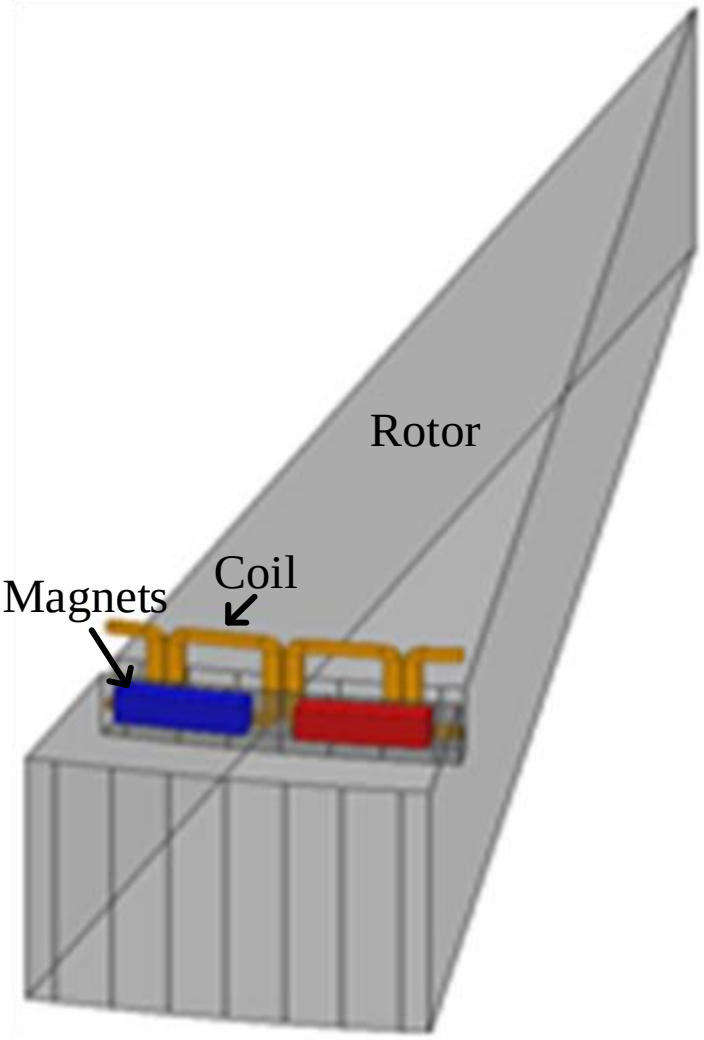

Fig. 55 Motor/Generator structure.

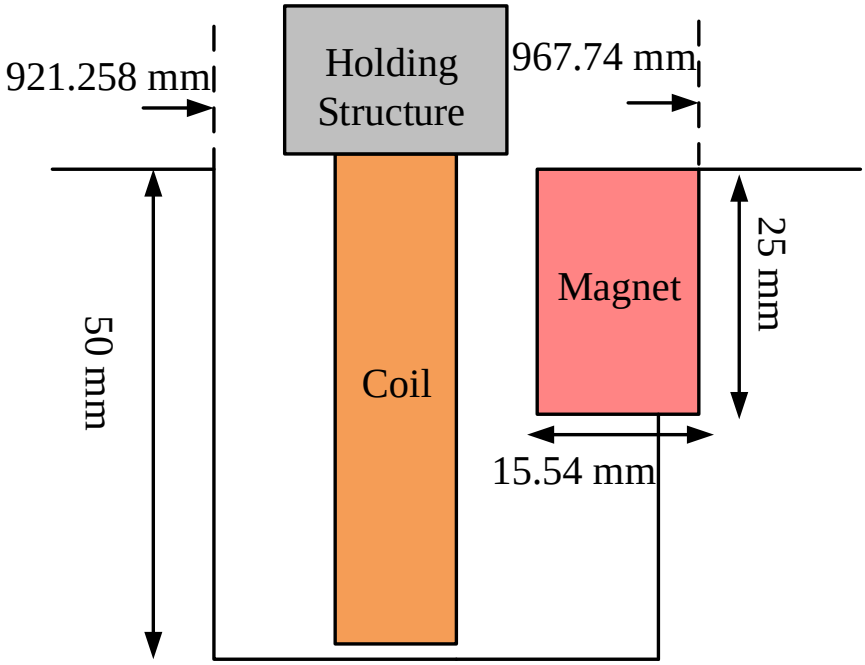

Fig. 56 Magnet, groove and coil geometry.

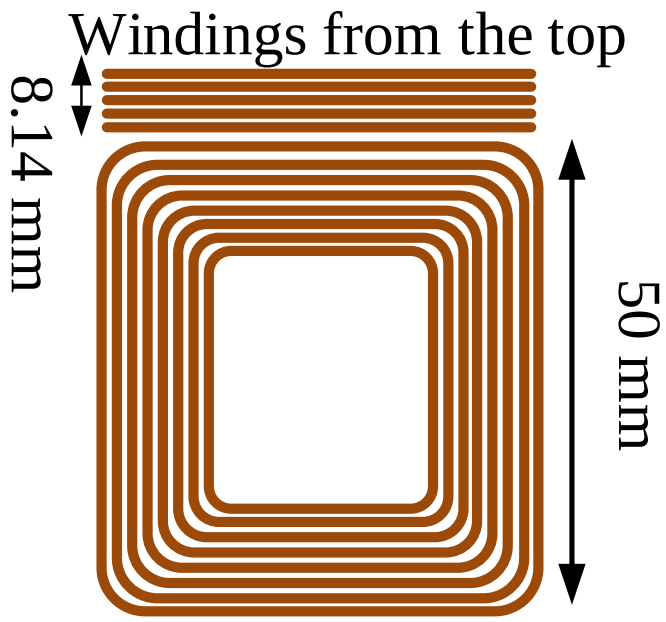

Fig. 57 Winding configuration.

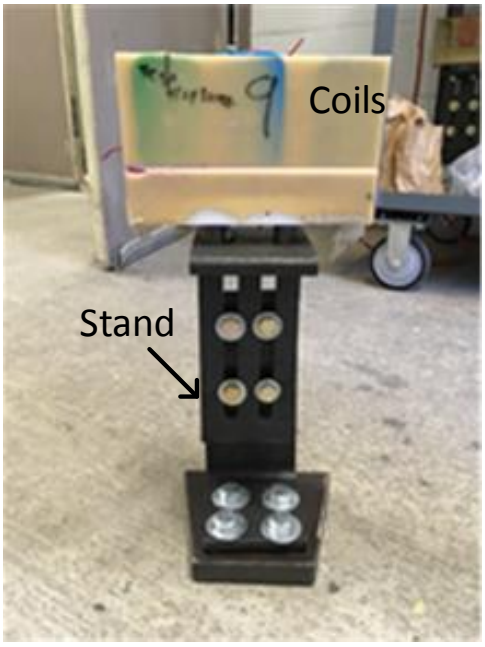

Fig. 58 The coil assembly and holding structure.

Considering the large size of the machine and limited winding space, a concentrated side by side type is used although lap winding may lead to achieve higher torque density. According to Fig. 56. the maximum allowable space for winding is 10 mm, thus 40 number of turns is used in order to achieve the required output torque. Magnet wire size of 14 AWG is used to accommodate the winding process by considering the current density limitation in vacuum. In each coil, 5 layers of winding exist where each layer has 8 turns as it is illustrated in Fig. 57. The top view in Fig. 57 shows the 5 layers of the winding and the bottom view illustrates the 8-turn arrangement in each layer. The fabrication of the coils is under development. Fig. 58 illustrates one set of three phase coils assembled as well as the developed holding structure.

Table 10 Motor/Generator electrical and mechanical specifications

Motor/Generator Mechanical Specifications		
Parameter	Quantity	Unit
Outer rotor diameter	2133.6	mm
Air-gap/groove stack height	50	mm
Motor/generator stack length	50	mm
Magnet height	25	mm
Air-gap/groove outer diameter	1904.4	mm
Air-gap/groove inner diameter	1842.5	mm
Winding height	50	mm
Magnet thickness	15.54	mm
Number of turns for each coil	40	-
Magnet type	NdFeB48	-
Magnet embrace	0.72	-
Cooling system	Air cooler	-
Motor/Generator Electrical Specifications		
Winding type	concentric	-
Number of phases	3	-
Parameter	Quantity	Unit
DC bus voltage	600	V
Maximum allowed current density	<5	A/mm2

Table 11 Average torque comparison of different combinations of number of poles and number of slots

Number of poles - Number of slots	Average Torque (N.m)
24 poles-36 slot	158
48 poles-72 slot	167
50 poles-75 slot	168
60 poles-90 slot	176
64 poles-96 slot	195

Table 12 Required current at different speeds

Speed (rpm)	Current (A)	Current density
5000 (rated)	210 (rated)	3
4000	220	3.3
3000	250	3.75
1928	300	4.5

The electrical and mechanical specifications of the motor/generator are given in Table 10. According to the geometry and constraints, several combinations of number of poles and number of slots were considered [101]: 24 poles - 36 slots, 48 poles - 72 slots, 50 poles - 75, 60 poles - 90 slots, and 64 poles - 96 slots. It is determined that a motor/generator with 64 poles and 96 slots gives the maximum average torque among all

these cases considering the requirements for this application. Table 11 compares all case studies average torque at rated speed. By having 96 slots, all coils are connected in parallel to the terminal in each phase. Table 12 provides the desired current that should be supplied at each speed to keep the output power constant and limit the current density bellow 5 A/mm^2.

6.3 FEA Electromagnetic Results

Fig. 59 illustrates the motor drive and control block diagram in conjunction with FEA. The motor/generator is supplied by a six-step current regulated converter with a hysteresis band of ± 10 A [102].

The schematic diagram of the two-level six-step current regulated voltage source inverter (VSI) fed PM motor/generator is shown in Fig. 60. According to Table II, V_{dc} is 600 V.

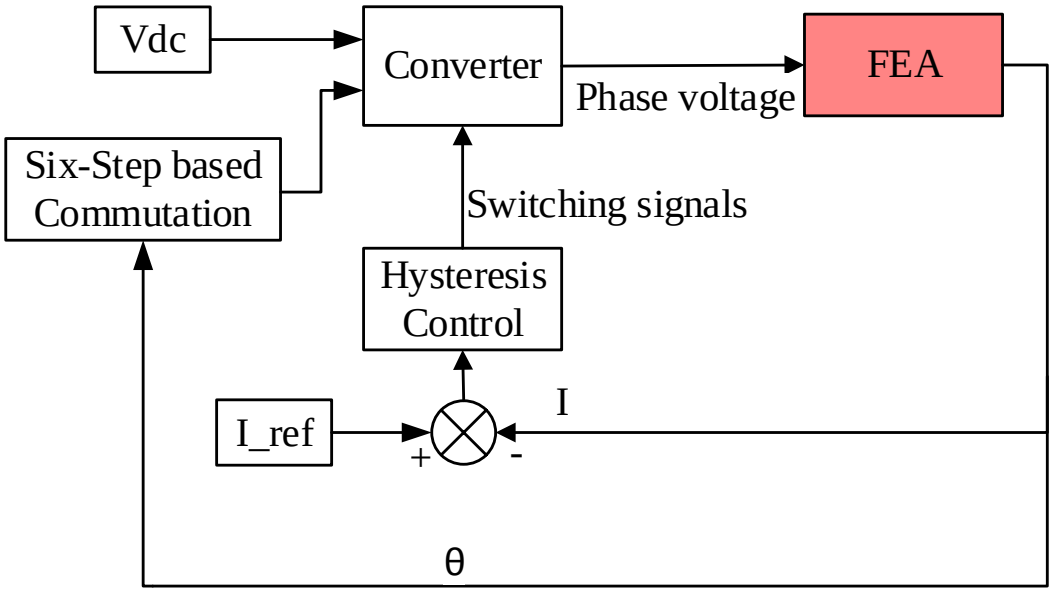

Fig. 59 The overall block diagram of the proposed PM motor/generator for FEA simulation in both generating and motoring modes of operation.

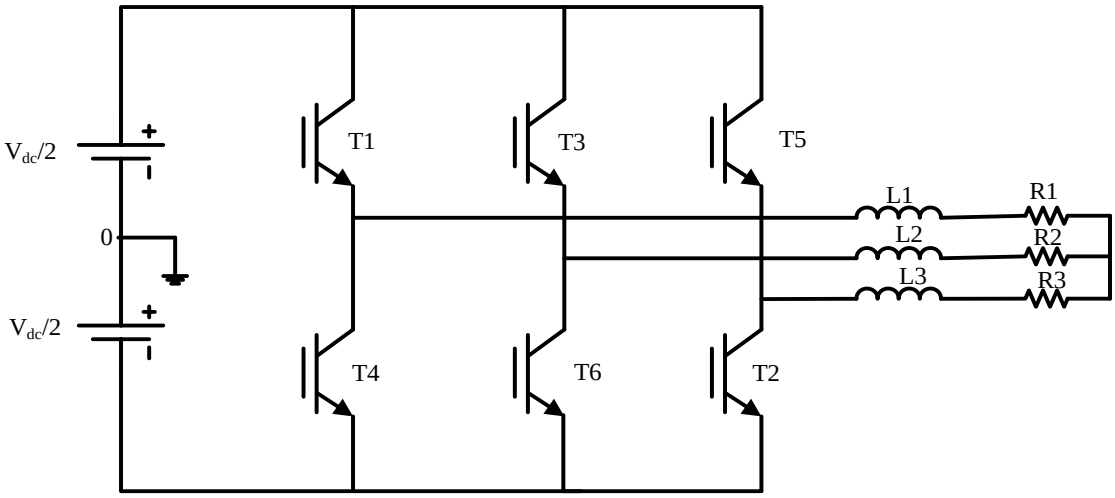

Fig. 60 Power electronics interface schematic of a two-level VSI fed PM motor/generator drive.

As aforementioned, during the charging mode of operation i.e. the constant torque region, the input current stays constant at rated current of 210 A as depicted in Fig. 61. Hence, the output power with the average of value 62.58 kW increases during speed up. On the contrary, during the discharging mode of operation i.e. the constant power region, by dropping the speed, the current supplied by the generator increases. Fig. 62 displays the input torque versus speed at constant output power of 100 kW. The desired current supplied at each speed is determined according to Table IV. Good agreements can be observed between the designed motor/generator torque-speed characteristics during both the charging and discharging modes of operations and the desired torque-speed characteristics as illustrated in Fig. 54.

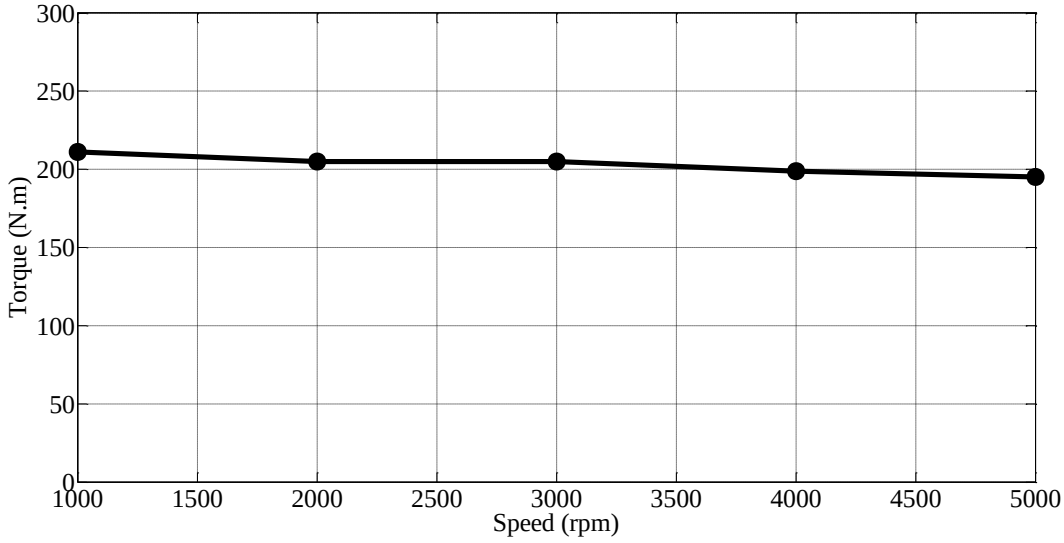

Fig. 61 The PM motor/generator torque during the charging mode of operation.

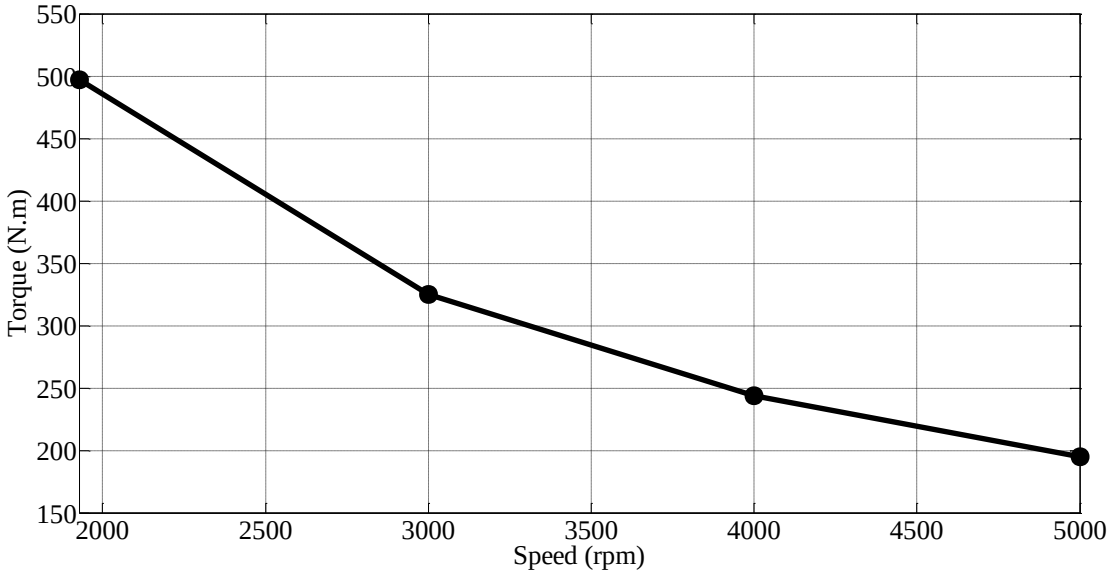

Fig. 62 The PM motor/generator output torque at rated speed of 5000 rpm during the motoring mode of operation.

Fig. 63 depicts the proposed motor/generator output torque waveform at the rated speed of 5000 rpm and rated current of 210 A. The average output torque is 195 N.m which is about 2% higher than the application requirement of 191 N.m. The torque ripple is relatively fair compared to the motor volume and weight. Fig. 64 depicts the three-phase current of the PM motor/generator at rated speed that are regulated at rated current of 210 A. The motor/generator winding flux linkages are shown in Fig. 65. From these flux linkages and the supplied current, the motor/generator self-inductance is determined to be around 6 μH per each phase.

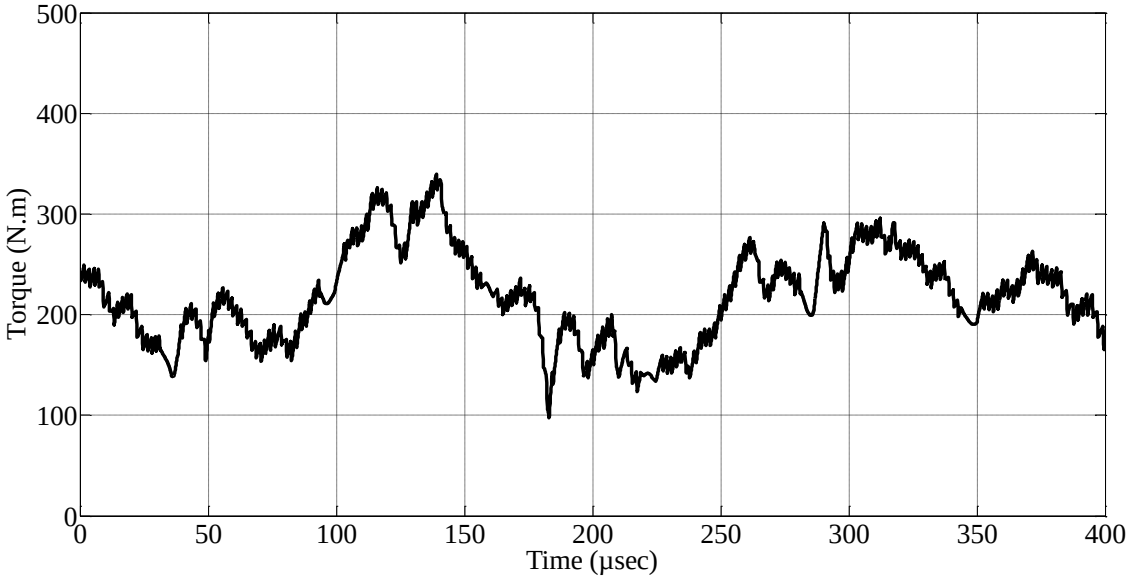

Fig. 63 The PM motor/generator torque during the discharging mode of operation.

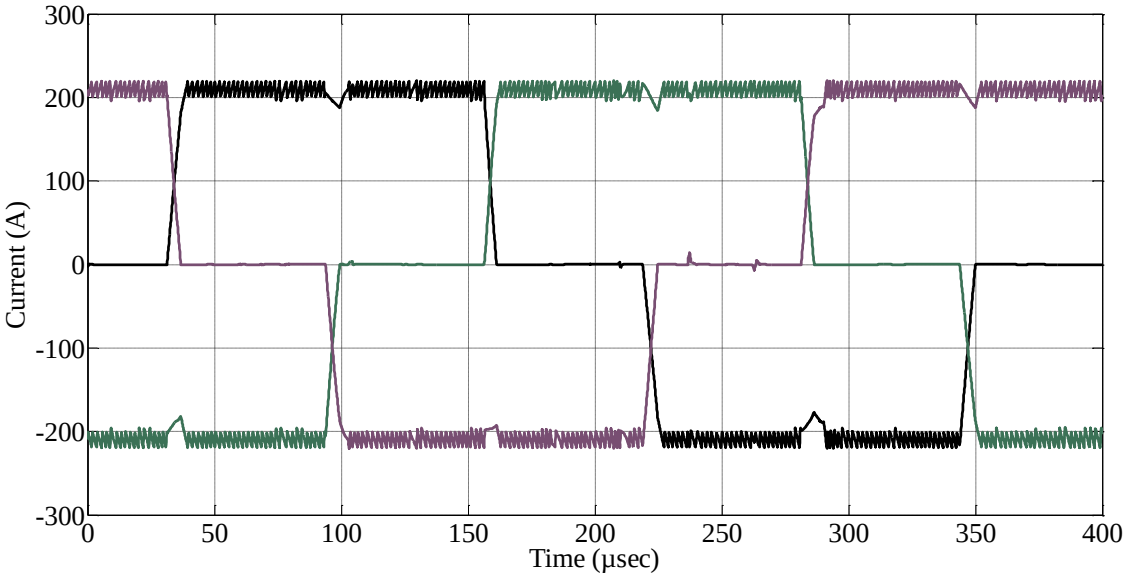

Fig. 64 The PM motor/generator current at rated speed of 5000 rpm during the motoring mode of operation.

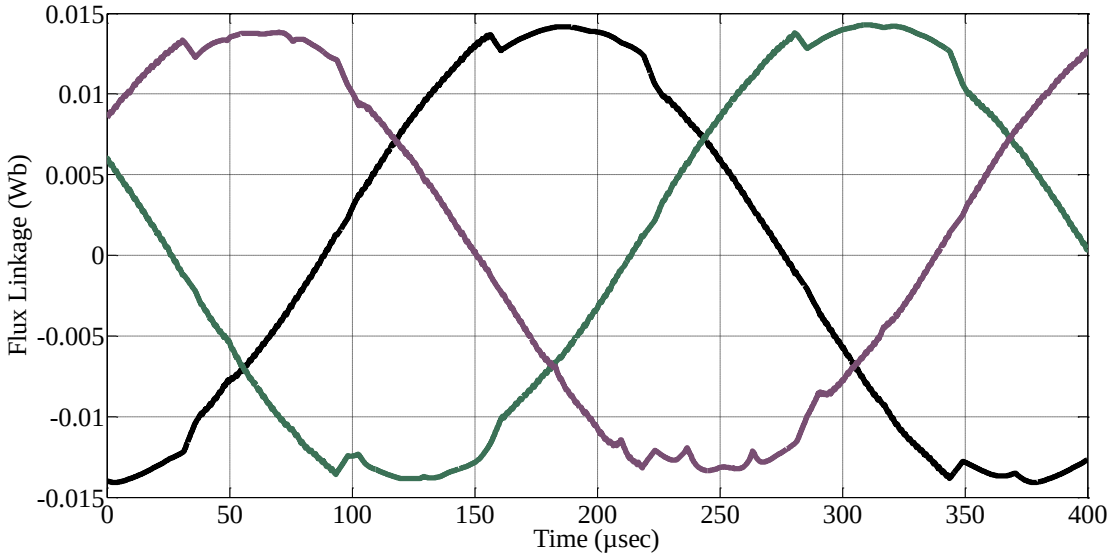

Fig. 65 The PM motor/generator flux linkage at rated speed of 5000 rpm in the motoring mode of operation.

Fig. 66 displays the flux density distribution when magnets are magnetized and stator carries its rated current of 210 A at rated speed of 5000 rpm; the maximum flux density is 0.92 T. Fig. 67 illustrates the flux plot while magnets are magnetized and stator current is 300 A at speed of 1928 rpm. As it is shown, flux density is larger in Fig. 66 and this is due to the larger current that is essential at 1928 rpm. In both cases, flux distribute mostly around the magnets and coils in the airgap. This is due to use of solid steel-4340 as the rotor material in order to have higher yield strength but it is suffering from poor magnetic characteristics. This leads the motor losses to appear mostly in the coils and magnets which are studied and presented in the next section.

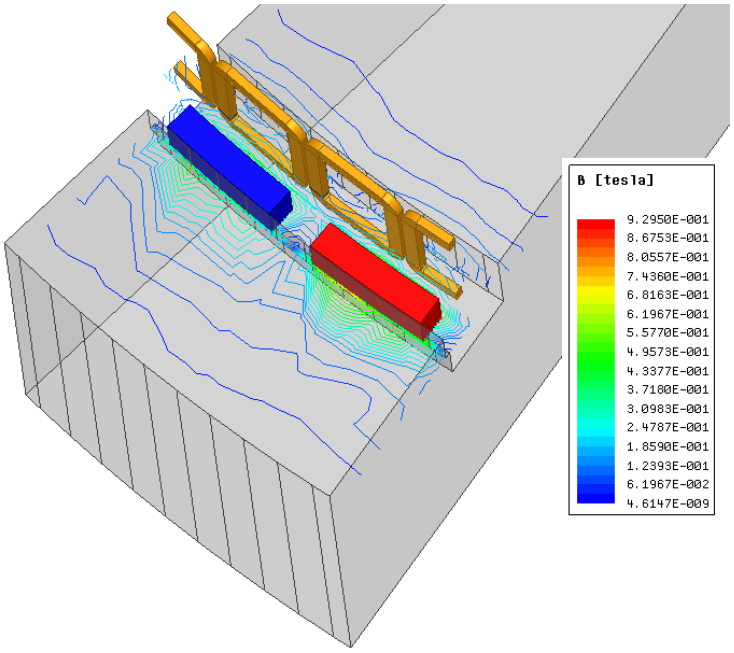

Fig. 66 Flux plot by magnets and stator current of 210 A in the motoring mode of operation.

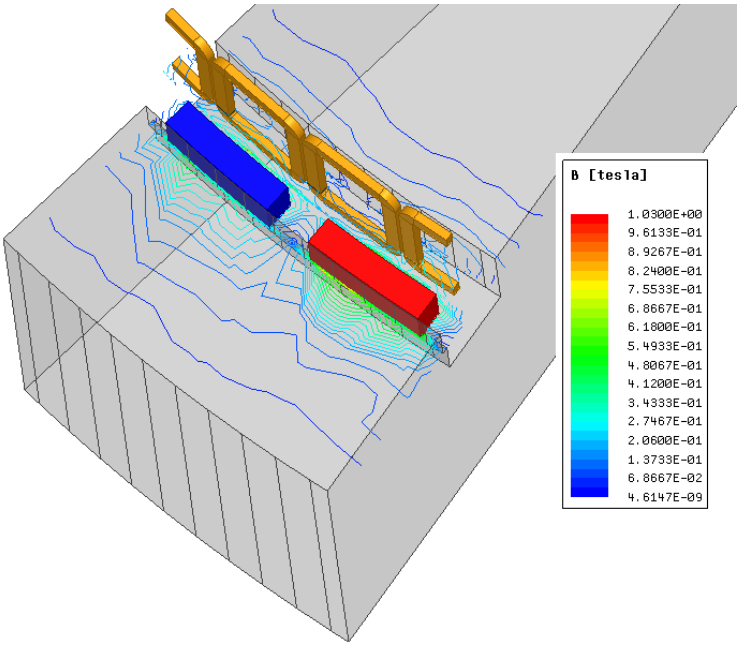

Fig. 67 Flux plot by magnets and stator current of 300 A in the motoring mode of operation.

6.4 The PM Motor/Generator Loss Analysis

The copper and core losses are the major losses of the motor. The core loss consists of eddy current loss, hysteresis loss and excess loss [103]. The employed magnets, NdFeB48, cause relatively low hysteresis loss, hence the hysteresis effect on the magnets are neglected in this study [104]. Eddy current loss of coils is neglected due to employing stranded coils. According to aforementioned discussion on the flux plot, the flux lines generated in the rotor core are limited. Hence, the core loss of the steel is neglected.

The copper loss calculated by FEA at rated current of 210 A is illustrated in Fig. 68 with average of 471 W. Eddy current loss caused by magnets at rated speed of 5000 rpm, with the frequency of 2.67 kHz, is relatively high with an average of 825 W as depicted in Fig. 69. Table 13 gives the average of copper and eddy current losses of the motor/generator during the motoring mode of operation. Due to operating at constant current, the copper loss stays constant as well. However, the eddy current loss increases with speed growth [105]. Hence, the maximum total losses appear at 5000 rpm.

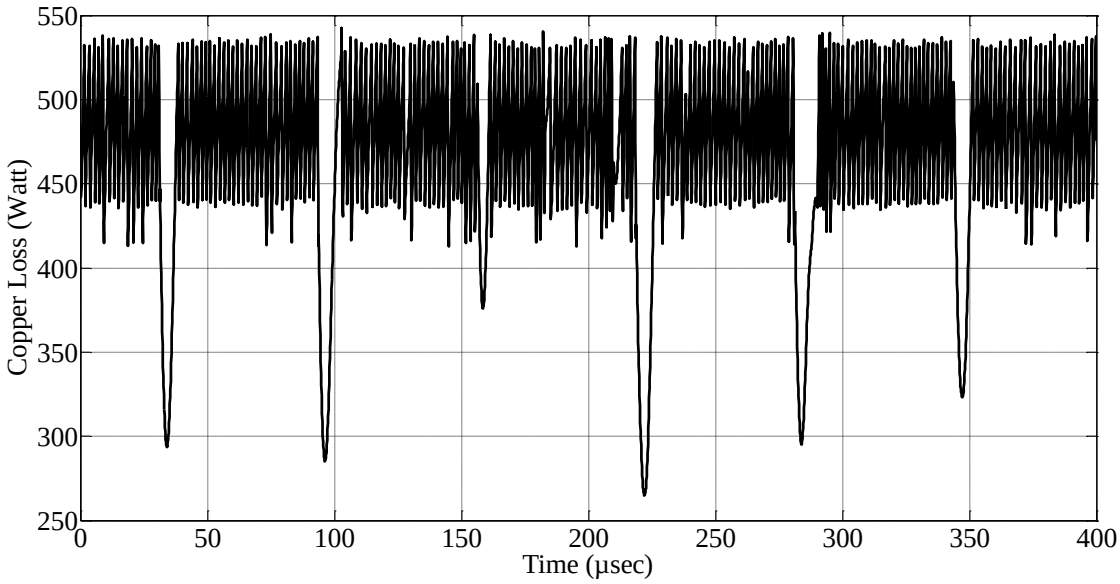

Fig. 68 Copper loss at rated speed of 5000 rpm and rated current of 250 A.

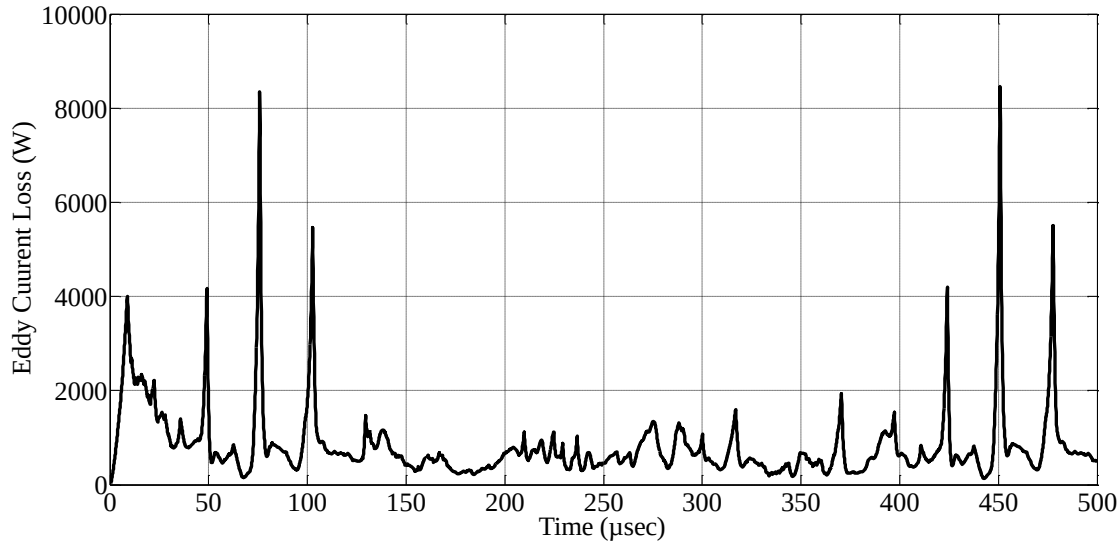

Fig. 69 Eddy current loss at rated speed of 5000 rpm and rated current of 250 A.

Table 13 The average of copper and magnet eddy current losses of the motor/generator during the charging mode of operation

Speed (rpm)	Current (A)	copper loss (W)	eddy current loss (W)	Total losses (W)
5000	210	471	825	1296
4000	210	471	657	1128
3000	210	471	582	1053
1928	210	471	531	1002

As given in Table 12, during the generating mode of operation, copper loss obviously would increase when the supplied current is higher. Eddy current losses rise with the increase of frequency or speed. In addition, the maximum total losses appear at lowest and highest speed, 1.5 kW at 1928 rpm and it is 1.3 kW at 5000 rpm.

Table 14 The average of copper and magnet eddy current loss during the discharging mode of operation

Speed (rpm)	Current (A)	copper loss (W)	eddy current loss (W)	Total losses (W)
5000	210	471	825	1296
4000	220	516	657	1173
3000	250	670	582	1252
1928	300	960	531	1491

Table 15 The average of input and output power of the motor/generator during the charging mode of operation

Speed (rpm)	Current (A)	Input power (kW)	Output power (kW)	Efficiency (%)
5000	210	103.3	102	98
4000	210	84.42	83.3	98
3000	210	65.3	64.3	98
1928	210	42.3	41.3	97
1000	210	22.5	22	97

Table 16 The average of input and output power of the motor/generator during the discharging mode of operation

Speed (rpm)	Current (A)	Input power (kW)	Output power (kW)	Efficiency (%)
5000	210	102	100	98 %
4000	220	103	101.9	98 %
3000	250	102	100.8	98 %
1928	300	103	101.5	98 %

In both the charging and discharging modes of operations, the total losses are relatively low comparing to the input power. The proposed motor/generator's efficiency in the

charging and discharging modes of operation are given in Table 15 and Table 16, respectively.

6.5 Analysis of Other Components

A: Coreless Winding Support Structure Analysis

Due to the coreless design, the force applied on the winding and its support must be examined to make an efficient, adjustable holding structure to prevent the magnetic field force from causing excessive deflections. The radial, tangential and vertical forces are calculated in FEA. Fig. 70 depicts the force applied on the winding in cylindrical coordinate system at rated current of 210 A. The applied force peak value is 100 N in the radial and is 120 N in the tangential directions. The force is also calculated at 1928 rpm where the highest current of 300 A is supplied as depicted in Fig. 71. In this case, the peak force in the radial and tangential directions are 200 N and 300 N, respectively. As shown in Fig. 58, a coil support structure consists of two L-shape brackets made of plain carbon steel. The upper bracket has four unthreaded holes for inserting the fasteners. The lower bracket has two slots with matched positions. The coils can be moved upward or downward by adjusting the amount of overlap between the two brackets and fixating their relative motion by the fasteners. Each of the coil holder supports three coils each of which is for a single phase. The three coils are potted together and fixed onto the top bracket.

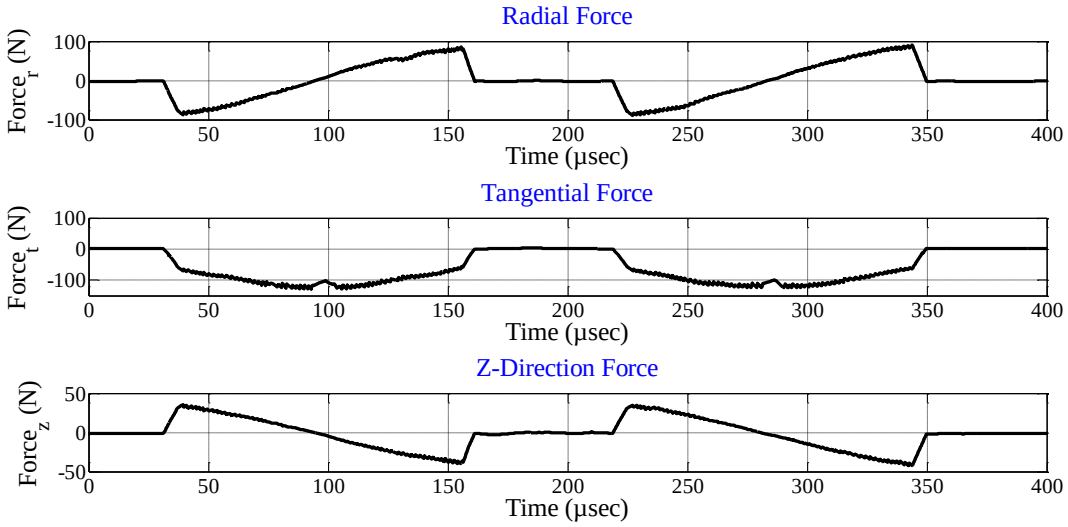

Fig. 70 Force applied to the coils at rated of 210 A.

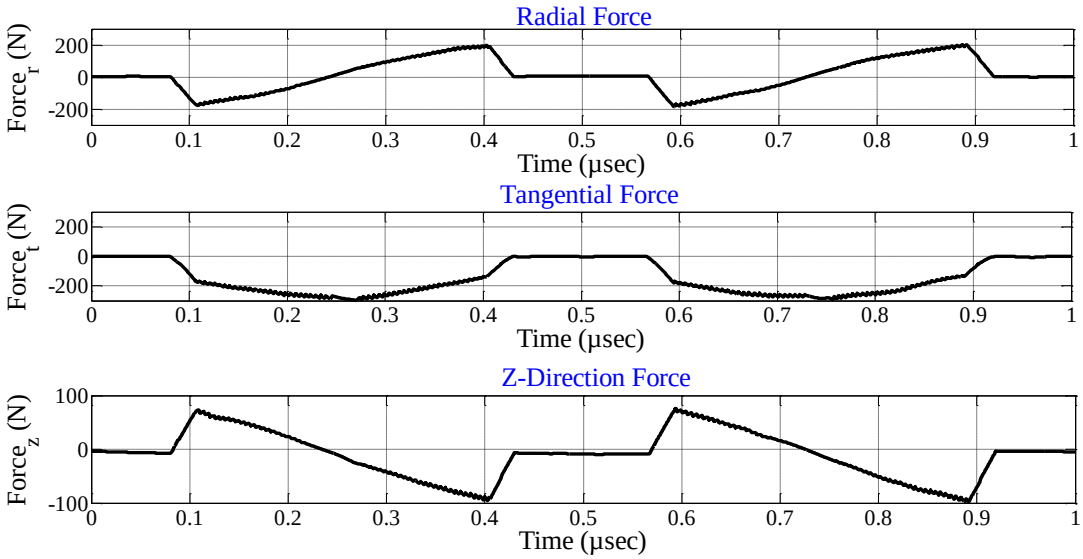

Fig. 71 Force applied to the coils at rated of 300 A.

As depicted in Fig. 72, Static FEA analysis shows that when the flywheel is operating at 1928 rpm, under the peak radial force of 200 N, the holder experiences 31 Mpa of stress

0.83 mm of deformation which is acceptable given the airgap of 10.5 mm. The stress level is under the material's yielding point which is typically 250 Mpa or higher. Since the structure is much stiffer in the tangential and vertical directions. The maximum Von Mises stress and deformation under peak current are only 27 Mpa/0.39 mm for tangential load and 5.3 Mpa/0.19 mm for axial load, respectively. When the flywheel is operating at 5000 rpm, due to the reduced current, the radial stress level and deformation drop to 14 Mpa and 0.39 mm which is only 3% of the airgap. The tangential and vertical loads cause 22 Mpa/0.32 mm and 8.5 Mpa/0.16 mm of maximum stress and deformation.

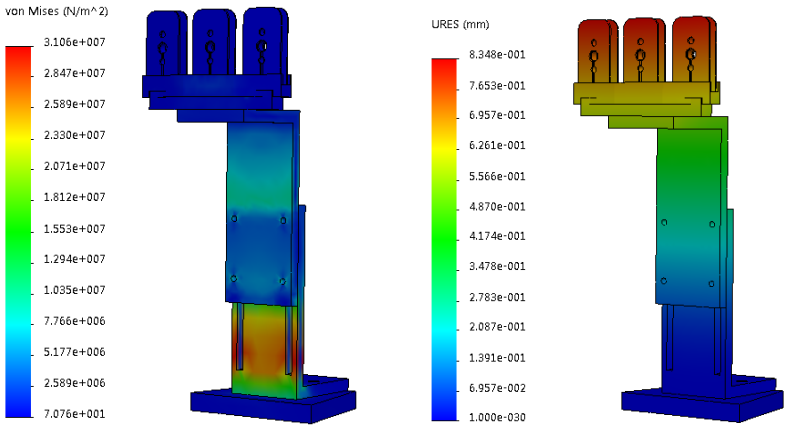

Fig. 72 Coil holder radial stress (left) and deformation (right) with motor current of 300 A.

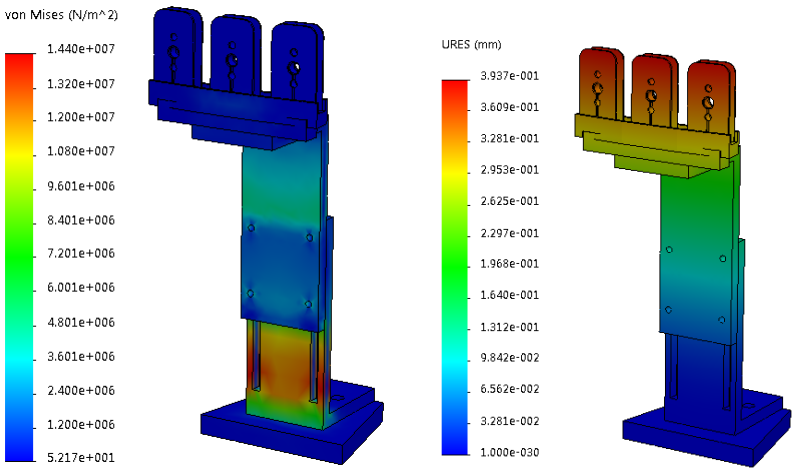

Fig. 73 Coil holder radial stress (left) and deformation (right) with motor current of 210 A.

B: Flywheel Thermal Analysis

Aforementioned, the PM motor/generator operates in a vacuum chamber. It brings up a concern of the heat dissipation. For the flywheel, which is being magnetic levitated without any physically contact and rotating in a vacuum space, there is no convective dissipation. In the meantime, heat generated by copper loss does not transfer from the coils to the magnets and rotor. Hence, eddy current is the only major sources that generates heat whereas radiation is the only heat dissipation. The employing of a large rotor may reduce the opportunity of localized heat concentrations. Nevertheless, the steady-state temperature of the flywheel is investigated. An axial-symmetric model is used in static thermal FEA of the flywheel and motor magnets. The boundary conditions are set to radiation only. According to the loss estimations that are summarized in Table V, the highest PM-related power loss is about 825W. In addition to the motor loss, rotational

relative motion between the flywheel and AMB also brings eddy current loss, it was estimated by [106] that the AMB-related loss is around 315W at 5000 RPM. As depicted in Fig. , the steady state magnet temperature does not exceed 52 Celsius, which is well below the max operating temperature for N48 neodymium magnets. Under such temperature, its thermal expansion is also not significant. The maximum and minimal temperature results under different emissivity are summarized in Table 17.

Table 17 The average of input and output power of the motor/generator during the discharging mode of operation

Initial Temperature (Celsius)	Minimal Temperature (Celsius)	Maximum Temperature (Celsius)	Flywheel Emissivity
22	40.36	54.35	0.95
22	42.65	55.25	0.9
22	44.82	57.32	0.8
22	50.98	63.17	0.6

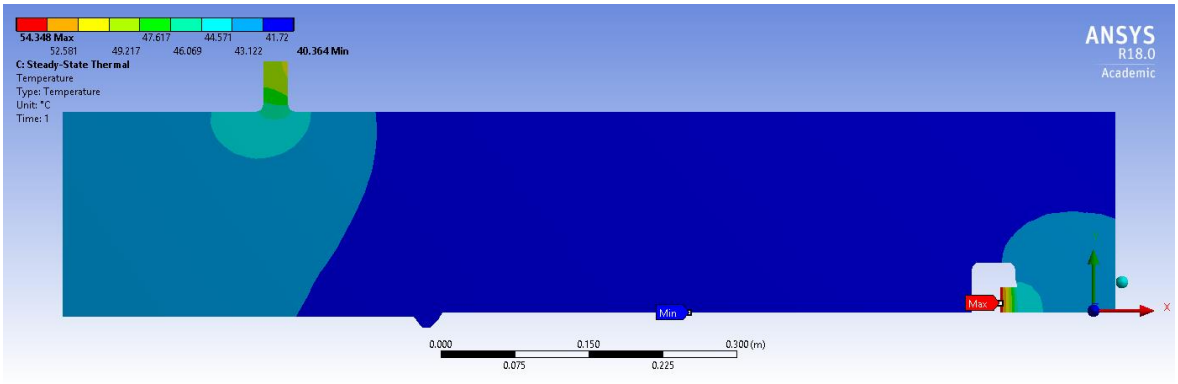

Fig. 74 Static analysis of the vacuum-enclosed- flywheel subjected to motor and magnetic bearing loss.

6.6 Conclusion and Discussion

A coreless PM motor/generator's design for a 5443 kg shaft-less energy storage flywheel system is proposed in this paper. Since flywheel is designed to operate in vacuum for reducing parasitic loss, the motor design was optimized in terms of geometry as well as utilized components to avoid generating excessive heat. FEA outcomes such as torque-speed and power-speed characteristics in the both charging and discharging modes are in a good agreement with the proposed flywheel architecture demand. The energy storage flywheel is capable of storing 422 MJ and the PM motor/generator is designed to supply constant power of 100 kW over an hour with speed drops from 5000 rpm to 1928 rpm. The motor/generator has high efficiency of 98% in both motoring and generating modes of operation. Due to owning coreless windings, the holder strength must be adequate to avoid excessive deformation. The force applied on coils is calculated in electromagnetic FEA for both high and low currents. Afterward, the holder was analyzed under the

measured forces in mechanical FEA with satisfactory results. The proposed PM motor/generator is under development in terms of winding the coils and placing the permanent magnets. Static thermal analysis showed promising results with the proposed cooling system. For future work, the machine will be tested in motoring / discharging mode with the grid or renewable energy sources to examine its functionality.

7 SUMMARY AND FUTURE WORK

This dissertation includes two parts: A Switched Reluctance Machine Design and Drive for Electric Vehicle Application, and A Coreless Permanent-Magnet Machine for a Magnetically Levitated Shaft-Less Flywheel.

The dissertation presented a constrained multi-objective optimization framework for design and control of a SRM based on a non-dominated sorting genetic algorithm II (NSGA-II). The proposed methodology optimizes SRM operation for high volume traction applications by considering multiple criteria including efficiency, average torque, and torque ripple. Several constraints were defined by the considered application, such as the motor stack length, outer diameter, minimum operating power, minimum desired efficiency, rated speed, rated current, and supply voltage. The outcome of this optimization includes an optimal geometry, outlining variables such as air gap length, rotor inner diameter, stator pole arc angle, rotor pole arc angle, rotor back iron, stator pole height, and stator inner diameter as well as optimal turn-on and turn-off firing angles. Comprehensive finite element analysis (FEA) and experimental results are provided to validate the theoretical findings.

In the present study, a surrogate based procedure for optimization of firing angles was proposed in order to minimize the torque ripple of the SRM having dynamic loads. Neural network models were used as the surrogate model to replace torque and flux lookup tables which provided good agreement with FEA outputs. The turn on angle θ_{on} was calculated from an equation depending on the motor geometry, the dc bus voltage, the reference current and the motor speed. Through a two-dimensional exhaustive search, an

optimal θ_{off} was explored for any load by scanning the whole load-speed space. The explored optimized firing angles were then represented using a highly correlated neural network model to expedite and simplify the real-time control of the SRM. The theoretical analysis was verified by simulation as well as experiments.

Steady state thermal analysis of the SRM was also presented in this dissertation both in simulation and experiment.

As of future work for SRM:

a. General optimization of SRM can be considered which includes all design variables.
b. Turn-on angle can be optimized by NN model to increase the accuracy of the firing angles models.
c. Transient thermal analysis can be done to get promising results.
d. Running the motor at rated mode of operation which requires a developed setup.

The dissertation proposed a framework for the design and analysis of a coreless permanent magnet (PM) machine for a 100 kWh shaft-less high strength steel flywheel energy storage system (SHFES). The PM motor/generator was designed to meet the required specs in terms of torque-speed and power-speed characteristics given by the application. The proposed PM motor/generator comprehensive geometry, electromagnetic and mechanical dimensioning are followed by detailed 3-D finite element analysis (FEA). The torque, power, and speed determined by the FEA electromagnetic analysis were met by the application design requirements and constraints for both the charging and discharging modes of operation. Furthermore, the design and analysis of the coil holding

structures were discussed. Finally, the motor/generator static thermal analysis was discussed in order to validate the proposed cooling system functionality.

As of future work for SRM:

a. Using and optimization algorithm to design the motor although it is a large scale project but optimization would give precise results.
b. Using a transient thermal analysis.
c. Developing the motor/generator manufacturing and testing the machine.

REFERENCES

[1] R. Krishnan, Switched Reluctance Motor Drives: Modeling, Simulation, Analysis, Design, and Applications: CRC Press, 2001.

[2] T. J. E. Miller, Electronic Control of Switched Reluctance Machines: Newnes, 2001.

[3] K. Vijayakumar, R. Karthikeyan, S. Paramasivam, R. Arumugam, and K. N. Srinivas, "Switched Reluctance Motor Modeling, Design, Simulation, and Analysis: A Comprehensive Review," Magnetics, IEEE Transactions on, vol. 44, pp. 4605-4617, 2008.

[4] Z. Jinhui and A. V. Radun, "A New Method to Measure the Switched Reluctance Motor's Flux," in Applied Power Electronics Conference and Exposition, 2005. APEC 2005. Twentieth Annual IEEE, 2005, pp. 1994-1999 Vol. 3.

[5] N. H. Fuengwarodsakul, S. Bauer, O. Tsafak, and R. W. De Doncker, "Characteristic Measurement System for Automotive Class Switched Reluctance Machines," in Power Electronics and Applications, 2005 European Conference on, 2005, pp. 10 pp.-P.10.

[6] L. Kaiyuan, P. O. Rasmussen, and A. E. Ritchie, "Investigation of Flux-Linkage Profile Measurement Methods for Switched-Reluctance Motors and Permanent-Magnet Motors," Instrumentation and Measurement, IEEE Transactions on, vol. 58, pp. 3191-3198, 2009.

[7] R. Saxena, B. Singh, and Y. Pahariya, "Measurement of Flux Linkage and Inductance Profile of Srm," International Journal of Computer and Electrical Engineering, vol. 2, p. 5, 2010.

[8] J. Mahdavi, G. Suresh, B. Fahimi, and M. Ehsani, "Dynamic Modeling of Nonlinear Srm Drive with Pspice," in Industry Applications Conference, 1997. Thirty-Second IAS Annual Meeting, IAS '97., Conference Record of the 1997 IEEE, 1997, pp. 661-667 vol.1.

[9] G. Hongwei, F. R. Salmasi, and M. Ehsani, "Inductance Model-Based Sensorless Control of the Switched Reluctance Motor Drive at Low Speed," Power Electronics, IEEE Transactions on, vol. 19, pp. 1568-1573, 2004.

[10] J. Dang, "Switched Reluctance Machine Electromagnetic Design and Optimization," Ph.D. Dissertation, Dept. of Electrical and Computer Engineering, Georgia Institute of Technology, Atlanta, GA, 2015.

[11] M. Balaji and V. Kamaraj, “Design Optimization of Switched Reluctance Machine Using Particle Swarm Optimization,” in Electrical Energy Systems (ICEES), 2011 1st International Conference on, 2011, pp. 164-169.

[12] J. W. Jiang, B. Bilgin, B. Howey, and A. Emadi, “Design Optimization of Switched Reluctance Machine Using Genetic Algorithm,” in Electric Machines & Drives Conference (IEMDC), 2015 IEEE International, 2015, pp. 1671-1677.

[13] X. Wang, “Modeling and Implementation of Controller for Switched Reluctance Motor with Ac Small Signal Model,” M.S. Thesis, Dept. of Electrical Engineering, Virginia Polytechnic Institute and State University, Blacksburg, VT, 2001.

[14] S. K. Sahoo, S. K. Panda, and X. Jian-Xin, “Indirect Torque Control of Switched Reluctance Motors Using Iterative Learning Control,” IEEE Transactions on Power Electronics, vol. 20, pp. 200-208, 2005.

[15] P. V. N. P. P.Srinivas, “Pwm Control of Asymmetrical Converter Fed Switched Reluctance Motor Drive ”, 2015.

[16] B. Blanque, J. I. Perat, P. Andrada, and M. Torrent, “Improving Efficiency in Switched Reluctance Motor Drives with Online Control of Turn-on and Turn-Off Angles,” in Power Electronics and Applications, 2005 European Conference on, 2005, pp. 9 pp.-P.9.

[17] J. Ye, “Advanced Control Methods for Torque Ripple Reduction and Performance Improvement in Switched Reluctance Motor Drives,” Ph.D. Dissertation, Dept. of Electrical and Computer Engineering, McMaster University, Hamilton, Canada, 2014.

[18] H.-K. Bae, “Control of Switched Reluctance Motors Considering Mutual Inductance,” 2000.

[19] B. Anvari and H. A. Toliyat, " Simultaneous Optimization of Geometry and Firing Angles of In-Wheel Switched Reluctance Motor," The Ninth Annual IEEE Energy Conversion Congress and Exposition (ECCE 2017), Cincinnati, OH, 2017.

[20] Yongqi Li, “Real-Time Torque Ripple Minimization of Outer Rotor Switched Reluctance Motor,” Thesis, Texas A&M University, 2016.

[21] B. Anvari, H. A. Toliyat and B. Fahimi, "Simultaneous Optimization of Geometry and Firing Angles for In-Wheel Switched Reluctance Motor Drive," in IEEE Transactions on Transportation Electrification, vol. PP, no. 99, pp. 1-1.

[22] B. Bilgin, A. Emadi, and M. Krishnamurthy, “Comprehensive Evaluation of the Dynamic Performance of a 6/10 Srm for Traction Application in Phevs,” Industrial Electronics, IEEE Transactions on, vol. 60, pp. 2564-2575, 2013.

[23] B. Anvari, Y. Li, and H. Toliyat, “Comparison of Outer Rotor Permanent Magnet and Magnet-Less Generators for Direct-Drive Wind Turbine Applications,” in Electric Machines & Drives Conference (IEMDC), 2015 IEEE International, 2015, pp. 181-186.

[24] D. A. Torrey, “Switched Reluctance Generators and Their Control,” IEEE Transactions on Industrial Electronics, vol. 49, pp. 3-14, 2002.

[25] R. Cardenas, R. Pena, M. Perez, J. Clare, G. Asher, and P. Wheeler, “Control of a Switched Reluctance Generator for Variable-Speed Wind Energy Applications,” IEEE Transactions on Energy Conversion, vol. 20, pp. 781-791, 2005.

[26] R. Arumugam, J. F. Lindsay, and R. Krishnan, “Sensitivity of Pole Arc/Pole Pitch Ratio on Switched Reluctance Motor Performance,” in Industry Applications Society Annual Meeting, 1988., Conference Record of the 1988 IEEE, 1988, pp. 50-54 vol.1.

[27] B. Akin and M. Bhardwaj, “Trapezoidal Control of Bldc Motors Using Hall Effect Sensors,” Texas Instruments, Application Note SPRABQ6, July 2013.

[28] M. T. DiRenzo, “Switched Reluctance Motor Control–Basic Operation and Example Using the Tms320f240,” Texas Instruments, Application Report SPRA420A, Feb. 2000.

[29] C. Lin and B. Fahimi, "Optimization of commutation angles in SRM drives using FRM," 2012 IEEE Transportation Electrification Conference and Expo (ITEC), Dearborn, MI, 2012, pp. 1-6.

[30] B. Fahimi, A. Emadi and R. B. Sepe, "A switched reluctance machine-based starter/alternator for more electric cars," in IEEE Transactions on Energy Conversion, vol. 19, no. 1, pp. 116-124, March 2004.

[31] M. Abbasian, M. Moallem and B. Fahimi, "Double-Stator Switched Reluctance Machines (DSSRM): Fundamentals and Magnetic Force Analysis," in IEEE Transactions on Energy Conversion, vol. 25, no. 3, pp. 589-597, Sept. 2010.

[32] P. Asadi, "Development and application of an advanced switched reluctance generator drive," Ph.D. dissertattion, Texas A&M University, College Station, USA, 2006.

[33] T. J. E. Miller, "Optimal design of switched reluctance motors," in IEEE Transactions on Industrial Electronics, vol. 49, no. 1, pp. 15-27, Feb 2002.

[34] J. H. Fisch, Yun Li, P. C. Kjaer, J. J. Gribble and T. J. E. Miller, "Pareto-optimal firing angles for switched reluctance motor control," Second International Conference On Genetic Algorithms In Engineering Systems: Innovations And Applications, Glasgow, 1997, pp. 90-96.

[35] I. Husain and M. Ehsani, "Torque ripple minimization in switched reluctance motor drives by PWM current control," in IEEE Transactions on Power Electronics, vol. 11, no. 1, pp. 83-88, Jan 1996.

[36] M. Rodrigues, P. J. Costa Branco and W. Suemitsu, "Fuzzy logic torque ripple reduction by turn-off angle compensation for switched reluctance motors," in IEEE Transactions on Industrial Electronics, vol. 48, no. 3, pp. 711-715, Jun 2001.

[37] T. Raminosoa, B. Blunier, D. Fodorean and A. Miraoui, "Design and Optimization of a Switched Reluctance Motor Driving a Compressor for a PEM Fuel-Cell System for Automotive Applications," in IEEE Transactions on Industrial Electronics, vol. 57, no. 9, pp. 2988-2997, Sept. 2010.

[38] M. Ćosović, S. Smaka, I. Salihbegović and Š. Mašić, "Design optimization of 8/14 switched reluctance machine for electric vehicle," 2012 XXth International Conference on Electrical Machines, Marseille, 2012, pp. 2654-2659.

[39] X. D. Xue, K. W. E. Cheng, T. W. Ng and N. C. Cheung, "Multi-Objective Optimization Design of In-Wheel Switched Reluctance Motors in Electric Vehicles," in IEEE Transactions on Industrial Electronics, vol. 57, no. 9, pp. 2980-2987, Sept. 2010.

[40] B. Anvari, Y. Li and H. A. Toliyat, "Design of multiphase exterior rotor switched reluctance motor for traction applications," 2016 IEEE 25th International Symposium on Industrial Electronics (ISIE), Santa Clara, CA, 2016, pp. 161-166.

[41] V. Rallabandi and B. G. Fernandes, "Design procedure of segmented rotor switched reluctance motor for direct drive applications," in IET Electric Power Applications, vol. 8, no. 3, pp. 77-88, March 2014.

[42] A. Messac, A. Ismail-Yahaya, and C. A. Mattson, "The normalized normal constraint method for generating the Pareto frontier," in Structural and multidisciplinary optimization, vol. 25, pp. 86-98, 2003.

[43] T. J. E. Miller, Switched reluctance motors and their control: Magna Physics Pub., PP.45, 1993.

[44] I. Husain, "Minimization of torque ripple in SRM drives," IEEE Transactions on Industrial Electronics, vol. 49, pp. 28-39, 2002.

[45] P. C. Desai, M. Krishnamurthy, N. Schofield and A. Emadi, "Novel Switched Reluctance Machine Configuration With Higher Number of Rotor Poles Than Stator Poles: Concept to Implementation," in IEEE Transactions on Industrial Electronics, vol. 57, no. 2, pp. 649-659, Feb. 2010.

[46] K. Deb, A. Pratap, S. Agarwal and T. Meyarivan, "A fast and elitist multiobjective genetic algorithm: NSGA-II," in IEEE Transactions on Evolutionary Computation, vol. 6, no. 2, pp. 182-197, Apr 2002.

[47] H. Li and Q. Zhang, "Multiobjective Optimization Problems With Complicated Pareto Sets, MOEA/D and NSGA-II," in IEEE Transactions on Evolutionary Computation, vol. 13, no. 2, pp. 284-302, April 2009.

[48] M. D. Hennen, R. W. D. Doncker, N. H. Fuengwarodsakul, and J. O. Fiedler, "Single-Phase Switched Reluctance Drive With Saturation-Based Starting Method," IEEE Transactions on Power Electronics, vol. 26, pp. 1337-1343, 2011.

[49] R. J. Malak and C.J.J. Paredis, "Using Parameterized Pareto Sets to Model Design Concepts," Journal of Mechanical Design, vol. 132, 2010.

[50] E. Zitzler and L. Thiele, "Multiobjective optimization using evolutionary algorithms - A comparative case study," presented at the Conference on Parallel Problem Solving from Nature, Amsterdam, 1998.

[51] G. Ying, S. Lei, and Y. Pingjing, "Study on multi-objective genetic algorithm," in 3rd World Congress on Intelligent Control and Automation, 2000. , 2000, pp. 646-650 vol.1.

[52] K. Deb, Multi-Objective Optimization using Evolutionary Algorithms. Chichester: Wiley & Sons, 2001.

[53] P. C. Fishburn, “Utility theory for decision making,” DTIC Document, 1970.

[54] R. L. Keeney, Decisions with Multiple Objectives: Preferences and Value Trade-Offs. Cambridge, U.K.: Cambridge Univ. Press, 1993.

[55] S. Song, M. Zhang and L. Ge, "A New Fast Method for Obtaining Flux-Linkage Characteristics of SRM," in IEEE Transactions on Industrial Electronics, vol. 62, no. 7, pp. 4105-4117, July 2015.

[56] B. Akin and M. Bhardwaj, "Trapezoidal control of BLDC motors using hall effect sensors," Texas instruments, 2010.

[57] G. Currie, Fundamental mechanics of fluids: CRC Press, 2012.

[58] Y. K. Choi, H. S. Yoon, and C. S. Koh, "Pole-Shape Optimization of a Switched-Reluctance Motor for Torque Ripple Reduction," IEEE Transactions on Magnetics, vol. 43, pp. 1797-1800, 2007.

[59] D. H. Lee, T. H. Pham, and J. W. Ahn, "Design and Operation Characteristics of Four-Two Pole High-Speed SRM for Torque Ripple Reduction," IEEE Transactions on Industrial Electronics, vol. 60, pp. 3637-3643, 2013.

[60] C. Sahin, A. E. Amac, M. Karacor, and A. Emadi, "Reducing torque ripple of switched reluctance machines by relocation of rotor moulding clinches," IET Electric Power Applications, vol. 6, pp. 753-760, 2012.

[61] D. H. Lee, Z. G. Lee, J. Liang, and J. W. Ahn, "Single-Phase SRM Drive with Torque Ripple Reduction and Power Factor Correction," IEEE Transactions on Industry Applications, vol. 43, pp. 1578-1587, 2007.

[62] D. H. Lee, J. Liang, Z. G. Lee, and J. W. Ahn, "A Simple Nonlinear Logical Torque Sharing Function for Low-Torque Ripple SR Drive," IEEE Transactions on Industrial Electronics, vol. 56, pp. 3021-3028, 2009.

[63] C. Lin and B. Fahimi, "Reduction of torque ripple in Switched Reluctance Motor drives using Field Reconstruction Method," in IEEE Vehicle Power and Propulsion Conference, 2011, pp. 1-5.

[64] C. Mademlis and I. Kioskeridis, "Optimizing Performance in Current-Controlled Switched Reluctance Generators," IEEE Transactions on Energy Conversion, vol. 20, pp. 556-565, 2005.

[65] W. R. H. Araújo, C. A. Ganzaroli, W. P. Calixto, A. J. Alves, G. P. Viajante, M. R. C. Reis, et al., "Firing angles optimization for Switched Reluctance Generator using Genetic Algorithms," in 13th International Conference on Environment and Electrical Engineering (EEEIC), 2013, pp. 217-222.

[66] H. Chen, C. Sun, and Q. Wang, "Analysis of Flux-Linkage Characteristics of Switched Reluctance Linear Generator," IEEE Transactions on Applied Superconductivity, vol. 24, pp. 1-5, 2014.

[67] H. Chen, W. Yan, and Q. Wang, "Electromagnetic Analysis of Flux Characteristics of Double-Sided Switched Reluctance Linear Machine," IEEE Transactions on Applied Superconductivity, vol. 26, pp. 1-7, 2016.

[68] H. Chen, G. Han, W. Yan, S. Lu, and Z. Chen, "Modeling of a Switched Reluctance Motor Under Stator Winding Fault Condition," IEEE Transactions on Applied Superconductivity, vol. 26, pp. 1-6, 2016.

[69] S. Song, L. Ge, S. Ma, M. Zhang, and L. Wang, "Accurate Measurement and Detailed Evaluation of Static Electromagnetic Characteristics of Switched Reluctance Machines," IEEE Transactions on Instrumentation and Measurement, vol. 64, pp. 704-714, 2015.

[70] S. D. Huang, G. Z. Cao, Z. Y. He, J. F. Pan, J. A. Duan, and Q. Q. Qian, "Nonlinear Modeling of the Inverse Force Function for the Planar Switched Reluctance Motor Using Sparse Least Squares Support Vector Machines," IEEE Transactions on Industrial Informatics, vol. 11, pp. 591-600, 2015.

[71] E. El Tabach, L. Lancelot, I. Shahrour, and Y. Najjar, "Use of artificial neural network simulation metamodelling to assess groundwater contamination in a road project," Mathematical and computer modelling, vol. 45, pp. 766-776, 2007.

[72] M. T. Hagan, H. B. Demuth, and M. Beale, "Neural network design, 1996," Boston, PWS Pub.

[73] F. D. Foresee and M. T. Hagan, "Gauss-Newton approximation to Bayesian learning," in Neural Networks, 1997., International Conference on, 1997, pp. 1930-1935.

[74] T. J. E. Miller, Switched reluctance motors and their control: Magna Physics Pub., 1993.

[75] D. J. C. MacKay, “Bayesian Interpolation,” Neural Computation, vol. 4, pp. 415-447,1992.

[76] B. Akin and M. Bhardwaj, "Trapezoidal control of BLDC motors using hall effect sensors," Texas instruments, 2010.

[77] Arbab, Nasim, Wei Wang, Chenjie Lin, Joseph Hearron, and Babak Fahimi. "Thermal Modeling and Analysis of a Double-Stator Switched Reluctance Motor." IEEE Transactions on Energy Conversion 30, no. 3 (2015): 1209-1217.

[78] http://www.engineeringtoolbox.com/convective-heat-transfer-d_430.html

[79] Pohlhausen, E. "Der Wärmeaustausch zwischen festen Körpern und Flüssigkeiten mit kleiner Reibung und kleiner Wärmeleitung." ZAMM- Journal of Applied Mathematics and Mechanics/Zeitschrift für Angewandte Mathematik und Mechanik 1, no. 2 (1921): 115-121.

[80] Bergman, Theodore L., Frank P. Incropera, David P. DeWitt, and Adrienne S. Lavine. Fundamentals of heat and mass transfer. John Wiley & Sons, 2011.

[81] Lau, S. Intermediate Heat Transfer class notes, Texas A&M University, 2014.

[82] http://support.fluke.com/findsales/Download/Asset/3038318_6251_ENG_A_W.PDF

[83] http://wwweng.lbl.gov/~dw/projects/DW4229_LHC_detector_analysis/calculations/emissivity2.pdf

[84] Z. Wang, A. Palazzolo, and J. Park, "Hybrid Train Power with Diesel Locomotive and Slug Car–Based Flywheels for NOx and Fuel Reduction," Journal of Energy Engineering, vol. 138, pp. 215-236, 2012.

[85] B. Bolund, H. Bernhoff, and M. Leijon, "Flywheel energy and power storage systems," Renewable and Sustainable Energy Reviews, vol. 11, pp. 235-258, 2007.

[86] X. Li, A. Palazzolo, D. Tingey, X. Han, P. McMullen, and Z. Wang, "Shaft-Less Energy Storage Flywheel," in 9th International ASME Conference on Energy Sustainability, 2015, pp. 1-6.

[87] V. V. Athani and J. G. Mundhada, "High-Performance Translator for a High-Torque PM Stepping Motor," IEEE Transactions on Industrial Electronics and Control Instrumentation, vol. IECI-25, pp. 343-346, 1978.

[88] T. M. Mulcahy, J. R. Hull, K. L. Uherka, R. G. Abboud, and J. J. Juna, "Test results of 2-kWh flywheel using passive PM and HTS bearings," IEEE Transactions on Applied Superconductivity, vol. 11, pp. 1729-1732, 2001.

[89] D. Kowal, P. Sergeant, L. Dupré, and L. Vandenbossche, "The Effect of the Electrical Steel Properties on the Temperature Distribution in Direct-Drive PM Synchronous Generators for 5 MW Wind Turbines," IEEE Transactions on Magnetics, vol. 49, pp. 5371-5377, 2013.

[90] T. Reichert, T. Nussbaumer, and J. W. Kolar, "Split Ratio Optimization for High-Torque PM Motors Considering Global and Local Thermal Limitations," IEEE Transactions on Energy Conversion, vol. 28, pp. 493-501, 2013.

[91] K. H. Kim, H. I. Park, S. M. Jang, and J. Y. Choi, "Comparison of Characteristics of Double-Sided Permanent-Magnet Synchronous Motor/Generator According to Magnetization Patterns for Flywheel Energy Storage System Using an Analytical Method," IEEE Transactions on Magnetics, vol. 51, pp. 1-4, 2015.

[92] Y. Xu, N. Maki, and M. Izumi, "Performance Comparison of 10-MW Wind Turbine Generators With HTS, Copper, and PM Excitation," IEEE Transactions on Applied Superconductivity, vol. 25, pp. 1-6, 2015.

[93] S. J. Arand and M. Ardebili, "Multi-objective design and prototyping of a low cogging torque axial-flux PM generator with segmented stator for small-scale direct-drive wind turbines," IET Electric Power Applications, vol. 10, pp. 889-899, 2016.

[94] Z. Xiang, L. Quan, and X. Zhu, "A New Partitioned-Rotor Flux-Switching Permanent Magnet Motor With High Torque Density and Improved Magnet Utilization," IEEE Transactions on Applied Superconductivity, vol. 26, pp. 1-5, 2016.

[95] W. Rong-Jie, M. J. Kamper, K. V. d. Westhuizen, and J. F. Gieras, "Optimal design of a coreless stator axial flux permanent-magnet generator," IEEE Transactions on Magnetics, vol. 41, pp. 55-64, 2005.

[96] H. A. Hussain, B. Anvari and H. A. Toliyat, "A control method for linear permanent magnet electric submersible pumps in a modified integrated drive-motor system," 2017 IEEE International Electric Machines and Drives Conference (IEMDC), Miami, FL, 2017, pp. 1-7.

[97] P. Roshanfekr, S. Lundmark, B. Anvari and T. Thiringer, "Investigation of pole number selection in a synchronous reluctance generator for wind applications," 2017 IEEE International Electric Machines and Drives Conference (IEMDC), Miami, FL, 2017, pp. 1-6.

[98] Stamenkovic, N. Milivojevic, N. Schofield, M. Krishnamurthy, and A. Emadi, "Design, Analysis, and Optimization of Ironless Stator Permanent Magnet Machines," IEEE Transactions on Power Electronics, vol. 28, pp. 2527-2538, 2013.

[99] M. Ooshima, S. Kitazawa, A. Chiba, T. Fukao, and D. G. Dorrell, "Design and Analyses of a Coreless-Stator-Type Bearingless Motor/Generator for Clean Energy Generation and Storage Systems," IEEE Transactions on Magnetics, vol. 42, pp. 3461-3463, 2006.

[100] B. Anvari, X. Li, H. A. Toliyat, A. Palazzolo, Z. Wang and X. Han, "A coreless permanent-magnet machine for a magnetically levitated shaft-less flywheel," 2017 IEEE International Electric Machines and Drives Conference (IEMDC), Miami, FL, 2017, pp. 1-7.

[101] J. R. Hendershot, "Brushless DC Motor Phase, Pole and Slot Configurations," in Proceedings of 9th International Symposium on Incremental Motion Control Systems and Devices, 1990, pp. 146-159.

[102] D. W. Novotny and T. A. Lipo, "Vector control and dynamics of AC drives." vol. 41, ed: Oxford university press, 1996, pp. 142-150.

[103] D. Lin, P. Zhou, W. N. Fu, Z. Badics, and Z. J. Cendes, "A dynamic core loss model for soft ferromagnetic and power ferrite materials in transient finite element analysis," IEEE Transactions on Magnetics, vol. 40, pp. 1318-1321, 2004.

[104] G. S. Buja and M. P. Kazmierkowski, "Direct torque control of PWM inverter-fed AC motors - a survey," IEEE Transactions on Industrial Electronics, vol. 51, pp. 744-757, 2004.

[105] X. Li, B. Anvari, A. Palazzolo, Z. Wang and H. A. Toliyat, "A Utility Scale Flywheel Energy Storage System with a Shaft-less, Hub-less, High Strength Steel Rotor," IEEE Transactions on Industrial Electronics, accpeted, 2017.

[106] Wang, Z. A Novel Flywheel and Operation Approach for Energy Recovery and Storage. Diss. PhD thesis, Texas A&M University, College Station, TX, 2011.

APPENDIX A

SOLID WORK MODEL OF SRM TEST-BED

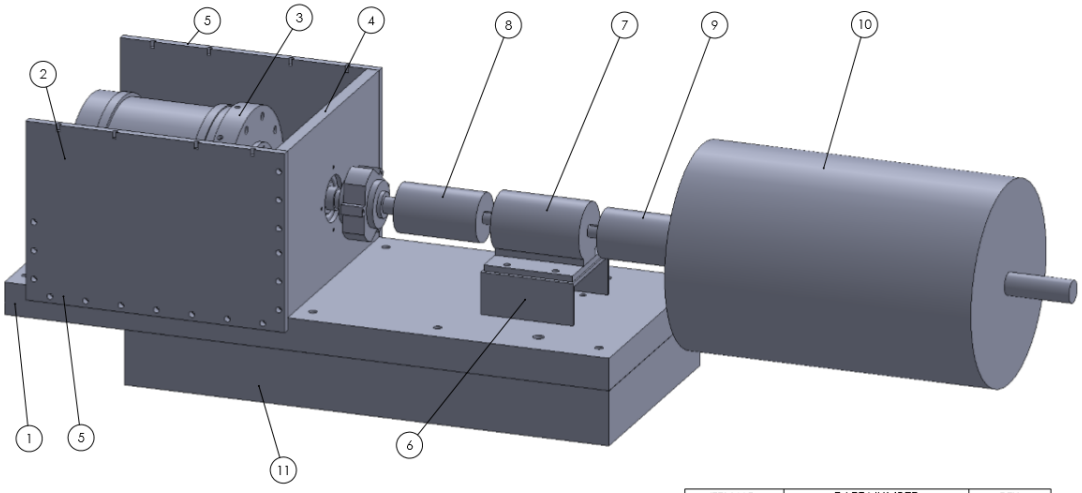

ITEM NO.	PART NUMBER	QTY.
1	SRM plate	1
2	Left wall	1
3	SRM-Cup assembly	1
4	Right wall Assembly	1
5	Front-back wall	2
6	Torquemeter riser	1
7	Torquemeter	1
8	TM-Cup coupling PFA300	1
9	TM-DC coupling PFS250	1
10	DC motor	1
11	Main bed	1

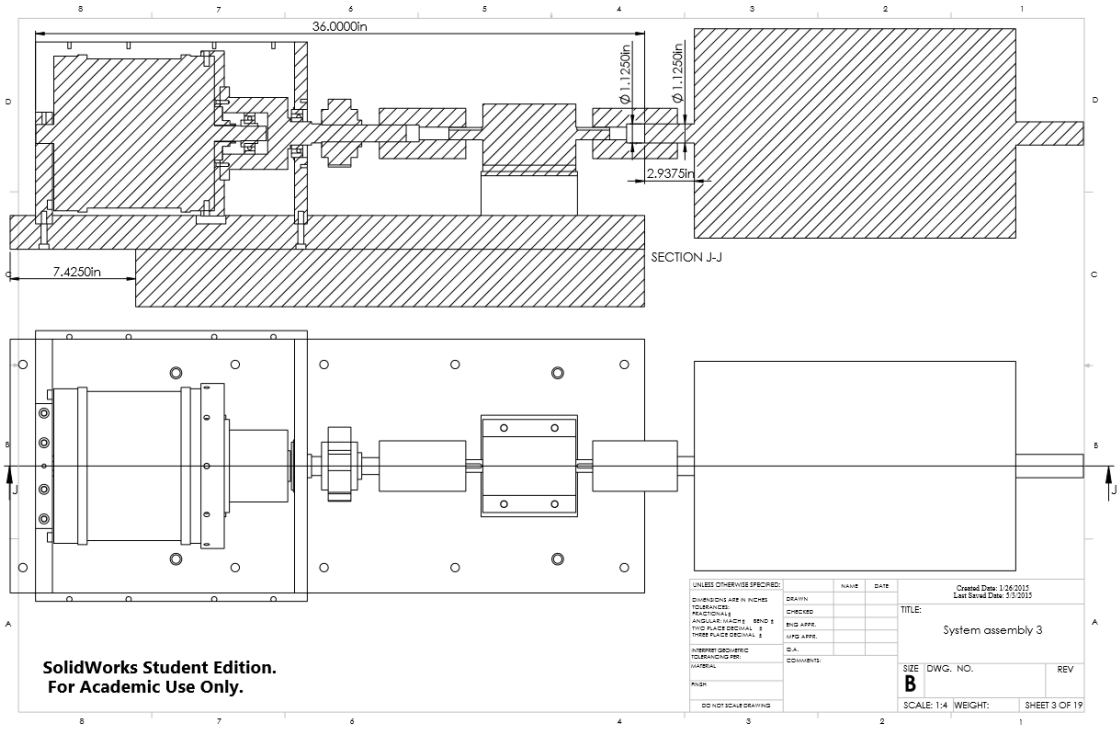
36.0000in
Ø1.1250in
Ø1.1250in
2.9375in
SECTION J-J
7.4250in
SolidWorks Student Edition.
For Academic Use Only.
Created Date: 1/26/2015
Last Saved Date: 5/5/2015
TITLE:
System assembly 3
SIZE B
DWG. NO.
REV
SCALE: 1:4
WEIGHT:
SHEET 3 OF 19

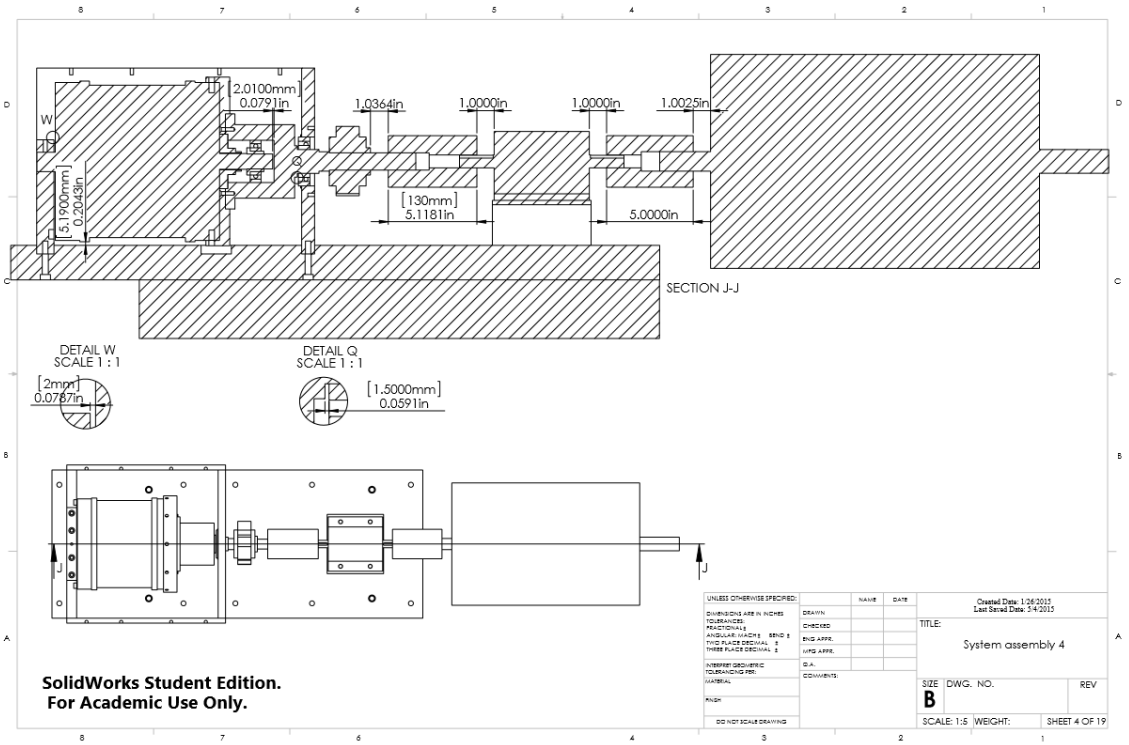
2.0100mm
0.0791in
1.0364in
1.0000in
1.0000in
1.0025in
W
Q
5.1900mm
0.2043in
[130mm]
5.1181in
5.0000in
SECTION J-J
DETAIL W
SCALE 1 : 1
[2mm]
0.0787in
DETAIL Q
SCALE 1 : 1
[1.5000mm]
0.0591in
SolidWorks Student Edition.
For Academic Use Only.
Created Date: 1/26/2015
Last Saved Date: 5/4/2015
TITLE:
System assembly 4
SIZE B
DWG. NO.
REV
SCALE: 1:5
WEIGHT:
SHEET 4 OF 19

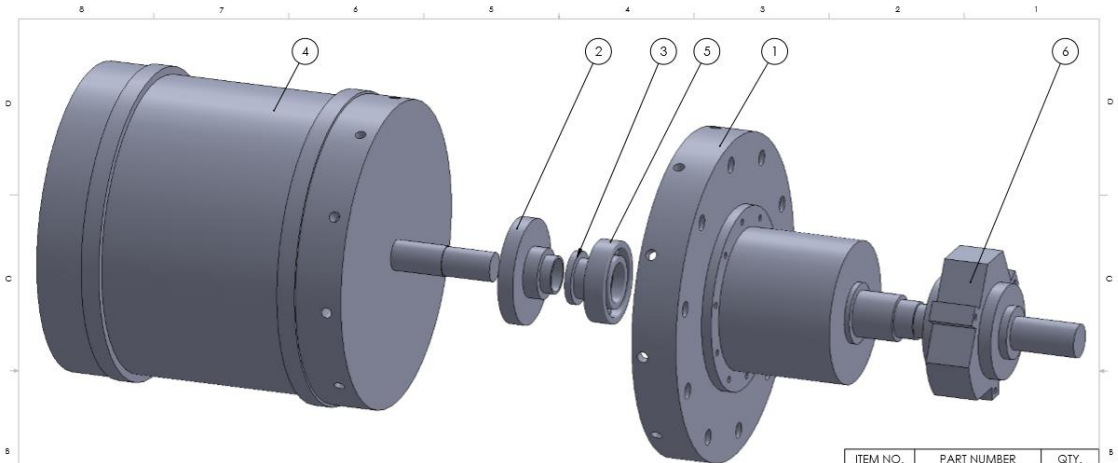

ITEM NO.	PART NUMBER	QTY.
1	Cup	1
2	Cup locator	1
3	Sleeve on SRM shaft	1
4	SRM	1
5	Bearing-in-cup	1
6	Encoder (Hohner)	1

UNLESS OTHERWISE SPECIFIED: DIMENSIONS ARE IN INCHES; TOLERANCES: FRACTIONAL ± ; ANGULAR: MACH ± BEND ± ; TWO PLACE DECIMAL ± ; THREE PLACE DECIMAL ± ; INTERPRET GEOMETRIC TOLERANCING PER: ; MATERIAL ; FINISH ; DO NOT SCALE DRAWING

NAME | DATE
DRAWN
CHECKED
ENG APPR.
MFG APPR.
Q.A.
COMMENTS:

Created Date: 1/26/2015
Last Saved Date: 5/4/2015

TITLE: Cup assembly

SIZE B | DWG. NO. | REV

SCALE: 1:2 | WEIGHT: | SHEET 5 OF 19

SolidWorks Student Edition.
For Academic Use Only.

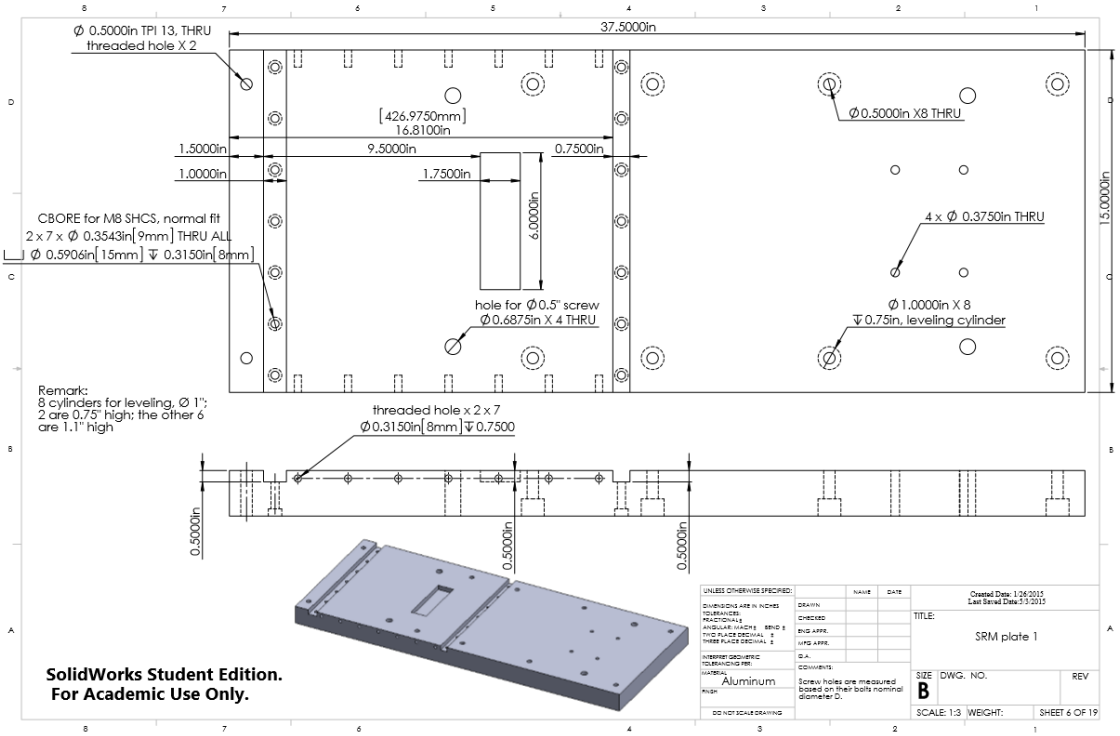

UNLESS OTHERWISE SPECIFIED: DIMENSIONS ARE IN INCHES; TOLERANCES: FRACTIONAL ± ; ANGULAR: MACH ± BEND ± ; TWO PLACE DECIMAL ± ; THREE PLACE DECIMAL ± ; INTERPRET GEOMETRIC TOLERANCING PER: ; MATERIAL Aluminum ; FINISH ; DO NOT SCALE DRAWING

NAME | DATE
DRAWN
CHECKED
ENG APPR.
MFG APPR.
Q.A.
COMMENTS:
Screw holes are measured based on their bolts nominal diameter D.

Created Date: 1/26/2015
Last Saved Date:5/5/2015

TITLE: SRM plate 1

SIZE B | DWG. NO. | REV

SCALE: 1:3 | WEIGHT: | SHEET 6 OF 19

SolidWorks Student Edition.
For Academic Use Only.

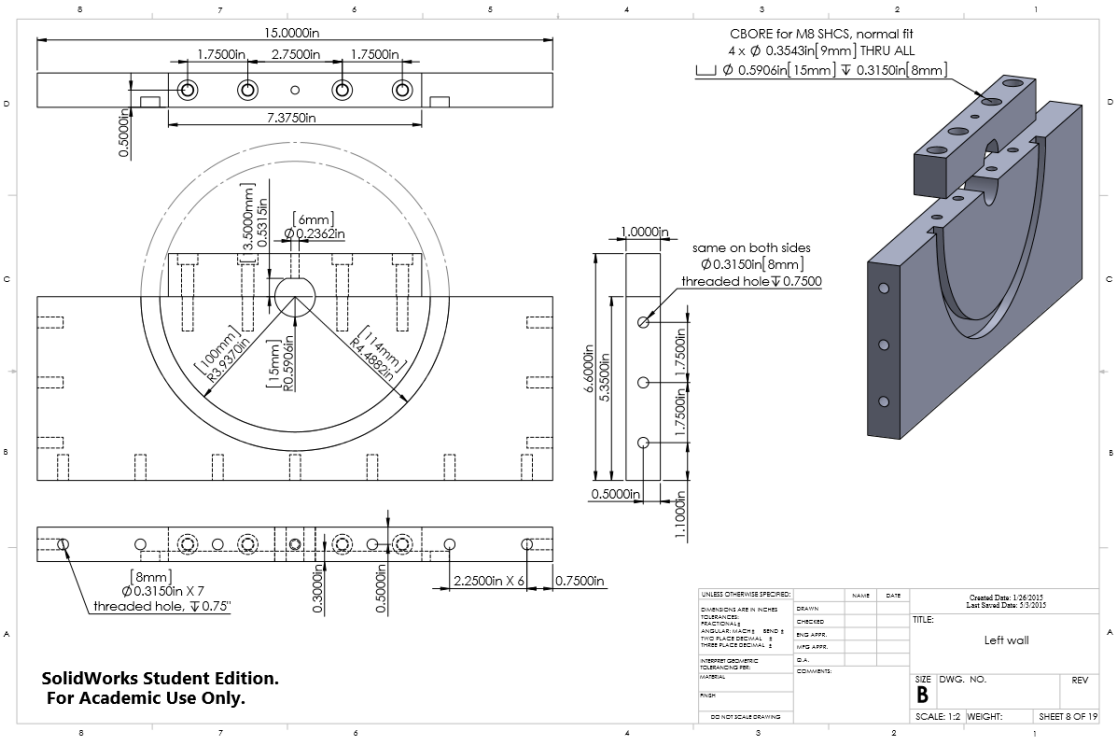
15.0000in
1.7500in
2.7500in
1.7500in
7.3750in
0.5000in
3.5000mm
0.5315in
[6mm]
Ø0.2362in
[100mm]
R3.9370in
[15mm]
R0.5906in
[114mm]
R4.4882in
CBORE for M8 SHCS, normal fit
4 x Ø 0.3543in[9mm] THRU ALL
Ø 0.5906in[15mm] ↧ 0.3150in[8mm]
1.0000in
same on both sides
Ø0.3150in[8mm]
threaded hole ↧0.7500
6.6000in
5.3500in
1.7500in
1.7500in
0.5000in
1.1000in
[8mm]
Ø0.3150in X 7
threaded hole, ↧0.75"
0.3000in
0.5000in
2.2500in X 6
0.7500in
SolidWorks Student Edition.
For Academic Use Only.
UNLESS OTHERWISE SPECIFIED:
DIMENSIONS ARE IN INCHES
TOLERANCES:
FRACTIONAL ±
ANGULAR: MACH ± BEND ±
TWO PLACE DECIMAL ±
THREE PLACE DECIMAL ±
INTERPRET GEOMETRIC TOLERANCING PER:
MATERIAL
FINISH
DO NOT SCALE DRAWING
NAME
DATE
DRAWN
CHECKED
ENG APPR.
MFG APPR.
Q.A.
COMMENTS:
Created Date: 1/26/2015
Last Saved Date: 3/3/2015
TITLE:
Left wall
SIZE
B
DWG. NO.
REV
SCALE: 1:2
WEIGHT:
SHEET 8 OF 19

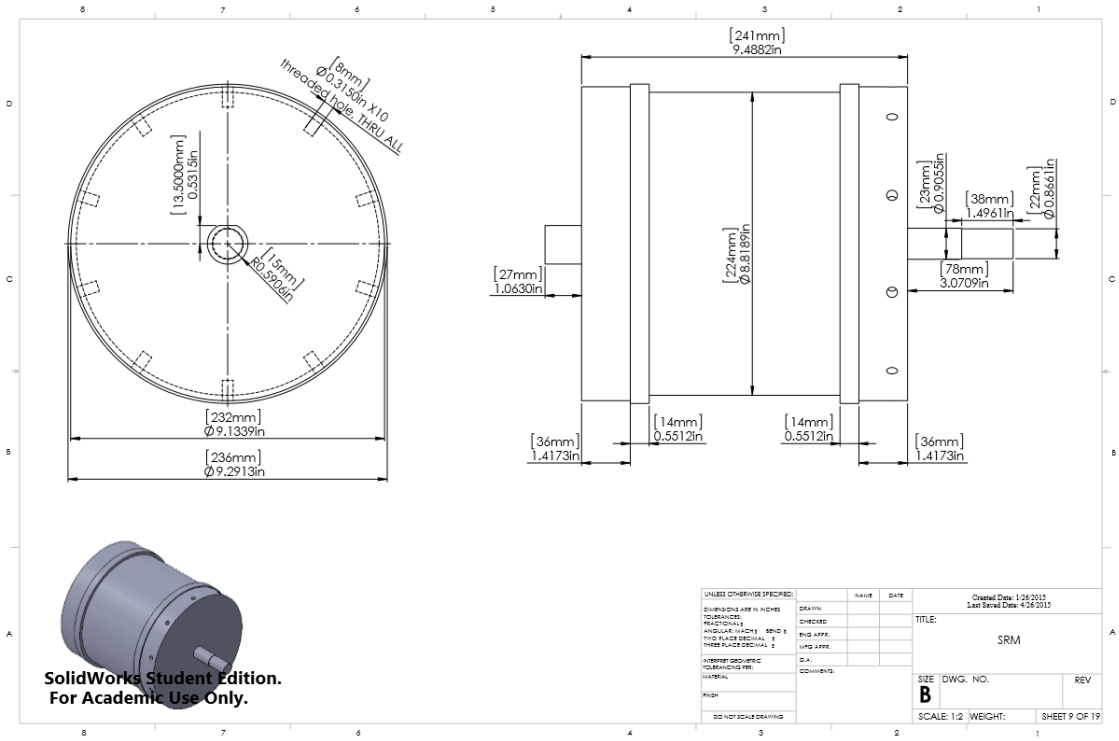
[8mm]
Ø0.3150in X10
threaded hole, THRU ALL
[13.5000mm]
0.5315in
[15mm]
R0.5906in
[232mm]
Ø9.1339in
[236mm]
Ø9.2913in
[241mm]
9.4882in
[23mm]
Ø0.9055in
[38mm]
1.4961in
[22mm]
Ø0.8661in
[224mm]
Ø8.8189in
[27mm]
1.0630in
[78mm]
3.0709in
[36mm]
1.4173in
[14mm]
0.5512in
[14mm]
0.5512in
[36mm]
1.4173in
SolidWorks Student Edition.
For Academic Use Only.
UNLESS OTHERWISE SPECIFIED:
DIMENSIONS ARE IN INCHES
TOLERANCES:
FRACTIONAL ±
ANGULAR: MACH ± BEND ±
TWO PLACE DECIMAL ±
THREE PLACE DECIMAL ±
INTERPRET GEOMETRIC TOLERANCING PER:
MATERIAL
FINISH
DO NOT SCALE DRAWING
NAME
DATE
DRAWN
CHECKED
ENG APPR.
MFG APPR.
Q.A.
COMMENTS:
Created Date: 1/26/2015
Last Saved Date: 4/26/2015
TITLE:
SRM
SIZE
B
DWG. NO.
REV
SCALE: 1:2
WEIGHT:
SHEET 9 OF 19

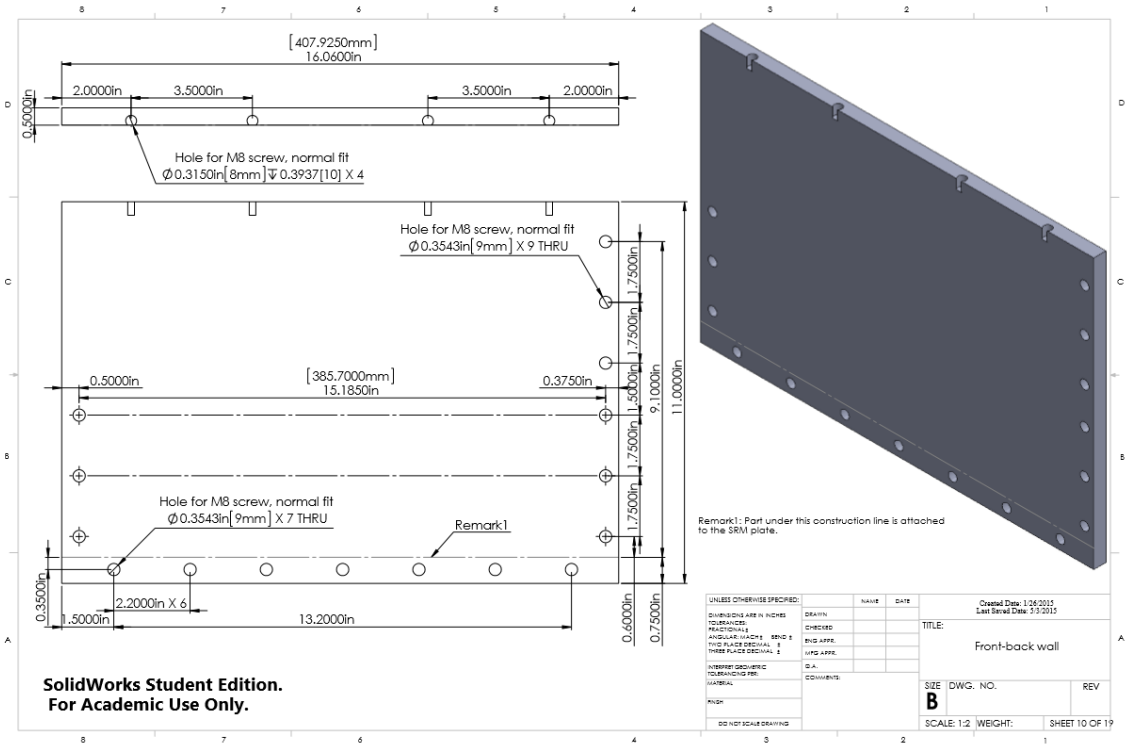
[407.9250mm]
16.0600in
2.0000in
3.5000in
3.5000in
2.0000in
0.5000in
Hole for M8 screw, normal fit
Ø0.3150in[8mm]↧0.3937[10] X 4
Hole for M8 screw, normal fit
Ø0.3543in[9mm] X 9 THRU
1.7500in
1.7500in
1.5000in
9.1000in
11.0000in
1.7500in
1.7500in
0.5000in
[385.7000mm]
15.1850in
0.3750in
Hole for M8 screw, normal fit
Ø0.3543in[9mm] X 7 THRU
Remark1
0.3500in
2.2000in X 6
1.5000in
13.2000in
0.6000in
0.7500in
Remark1: Part under this construction line is attached to the SRM plate.
UNLESS OTHERWISE SPECIFIED:
NAME
DATE
DRAWN
CHECKED
ENG APPR.
MFG APPR.
Q.A.
COMMENTS:
Created Date: 1/26/2015
Last Saved Date: 3/3/2015
TITLE:
Front-back wall
SIZE
DWG. NO.
REV
B
SCALE: 1:2
WEIGHT:
SHEET 10 OF 19
SolidWorks Student Edition.
For Academic Use Only.

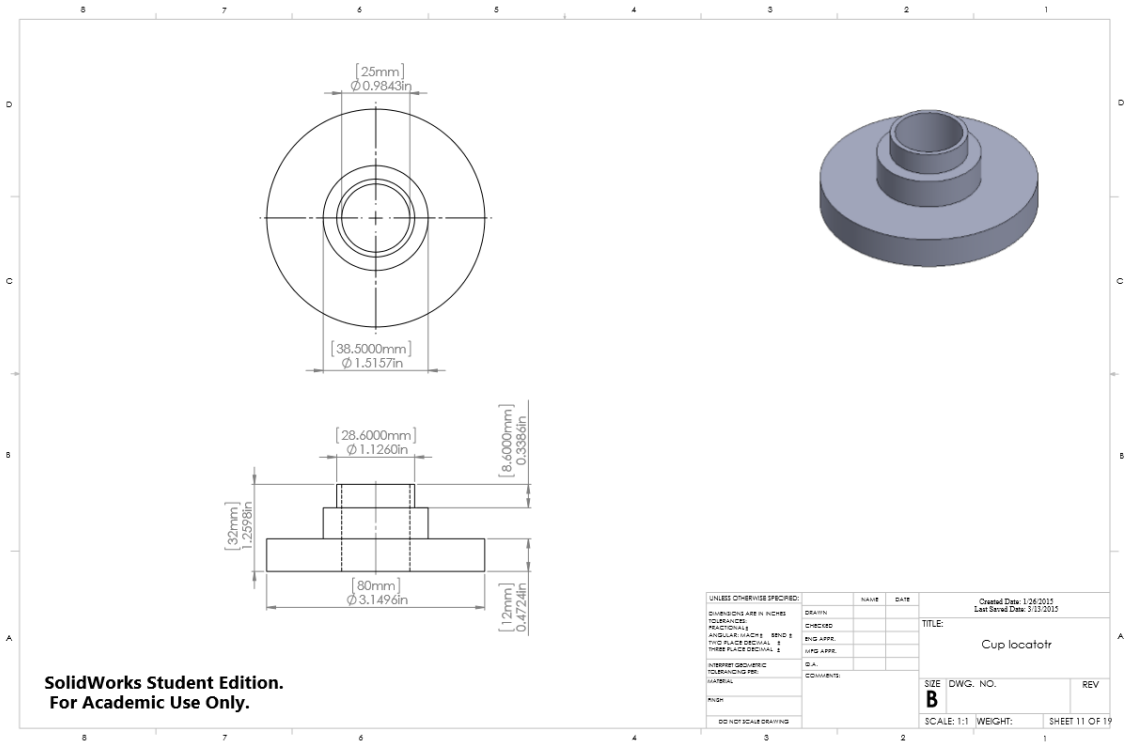
[25mm]
Ø0.9843in
[38.5000mm]
Ø1.5157in
[28.6000mm]
Ø1.1260in
[8.6000mm]
0.3386in
[32mm]
1.2598in
[80mm]
Ø3.1496in
[12mm]
0.4724in
UNLESS OTHERWISE SPECIFIED:
NAME
DATE
DRAWN
CHECKED
ENG APPR.
MFG APPR.
Q.A.
COMMENTS:
Created Date: 1/26/2015
Last Saved Date: 3/13/2015
TITLE:
Cup locatotr
SIZE
DWG. NO.
REV
B
SCALE: 1:1
WEIGHT:
SHEET 11 OF 19
SolidWorks Student Edition.
For Academic Use Only.

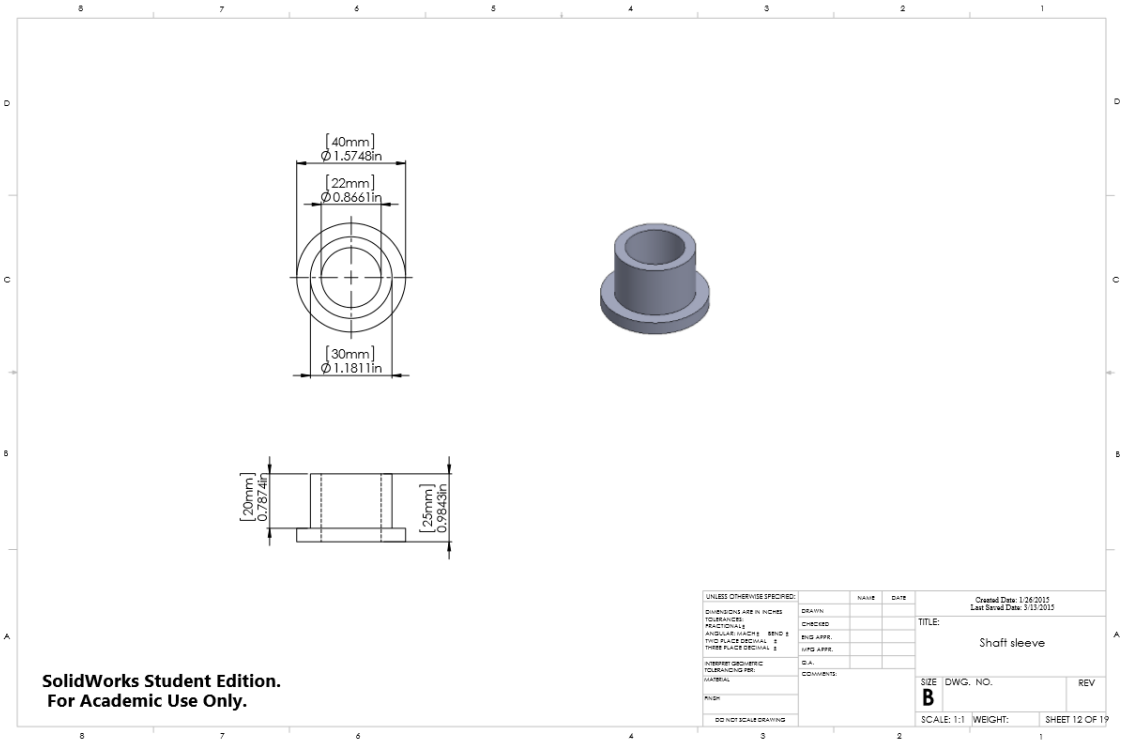
[40mm]
Ø1.5748in
[22mm]
Ø0.8661in
[30mm]
Ø1.1811in
[20mm]
0.7874in
[25mm]
0.9843in
SolidWorks Student Edition.
For Academic Use Only.
UNLESS OTHERWISE SPECIFIED:
DIMENSIONS ARE IN INCHES
TOLERANCES:
FRACTIONAL ±
ANGULAR: MACH ± BEND ±
TWO PLACE DECIMAL ±
THREE PLACE DECIMAL ±
INTERPRET GEOMETRIC TOLERANCING PER:
MATERIAL
FINISH
DO NOT SCALE DRAWING
NAME
DATE
DRAWN
CHECKED
ENG APPR.
MFG APPR.
Q.A.
COMMENTS:
Created Date: 1/26/2015
Last Saved Date: 3/13/2015
TITLE:
Shaft sleeve
SIZE
B
DWG. NO.
REV
SCALE: 1:1
WEIGHT:
SHEET 12 OF 19

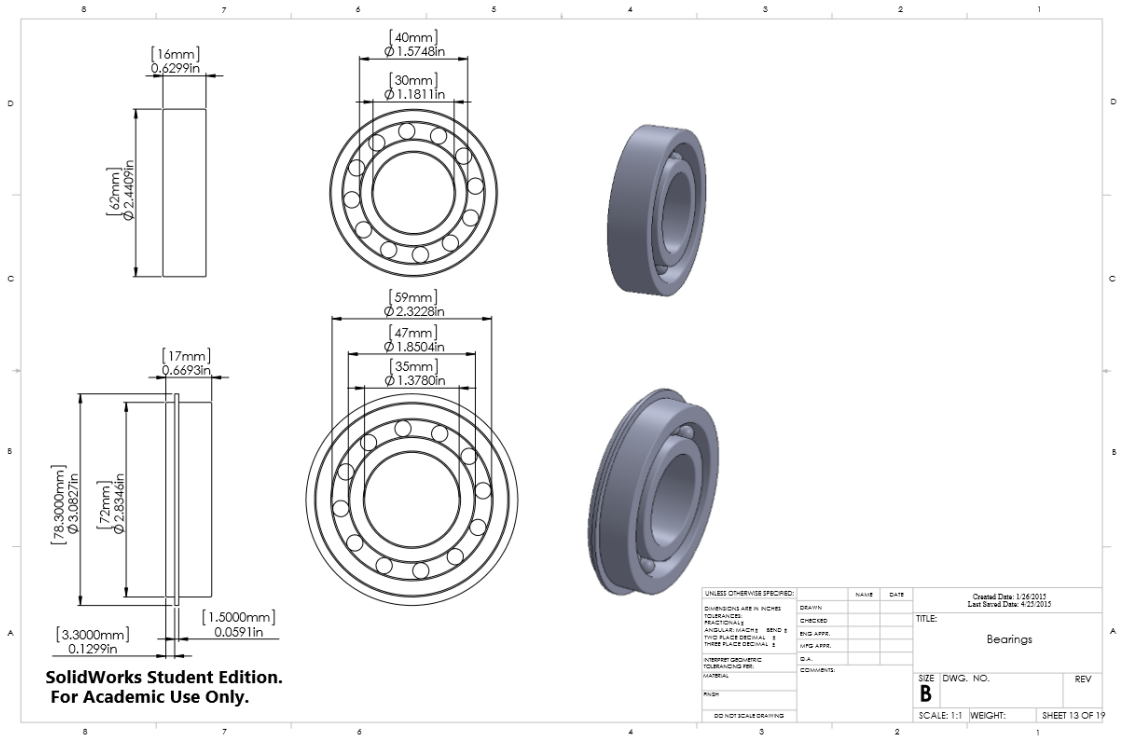
[16mm]
0.6299in
[62mm]
Ø2.4409in
[40mm]
Ø1.5748in
[30mm]
Ø1.1811in
[59mm]
Ø2.3228in
[47mm]
Ø1.8504in
[35mm]
Ø1.3780in
[17mm]
0.6693in
[78.3000mm]
Ø3.0827in
[72mm]
Ø2.8346in
[1.5000mm]
0.0591in
[3.3000mm]
0.1299in
SolidWorks Student Edition.
For Academic Use Only.
UNLESS OTHERWISE SPECIFIED:
DIMENSIONS ARE IN INCHES
TOLERANCES:
FRACTIONAL ±
ANGULAR: MACH ± BEND ±
TWO PLACE DECIMAL ±
THREE PLACE DECIMAL ±
INTERPRET GEOMETRIC TOLERANCING PER:
MATERIAL
FINISH
DO NOT SCALE DRAWING
NAME
DATE
DRAWN
CHECKED
ENG APPR.
MFG APPR.
Q.A.
COMMENTS:
Created Date: 1/26/2015
Last Saved Date: 4/25/2015
TITLE:
Bearings
SIZE
B
DWG. NO.
REV
SCALE: 1:1
WEIGHT:
SHEET 13 OF 19

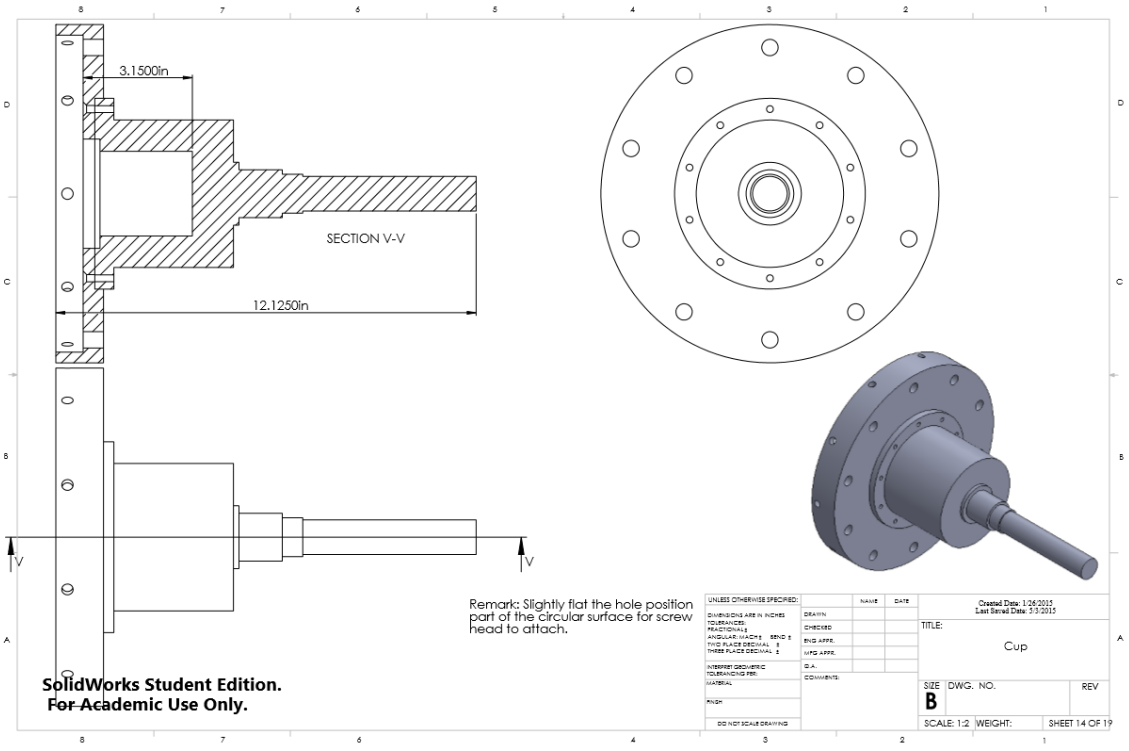
3.1500in
SECTION V-V
12.1250in
V
V
Remark: Slightly flat the hole position part of the circular surface for screw head to attach.
SolidWorks Student Edition.
For Academic Use Only.
Created Date: 1/26/2015
Last Saved Date: 5/3/2015
TITLE:
Cup
SIZE
B
DWG. NO.
REV
SCALE: 1:2
WEIGHT:
SHEET 14 OF 19

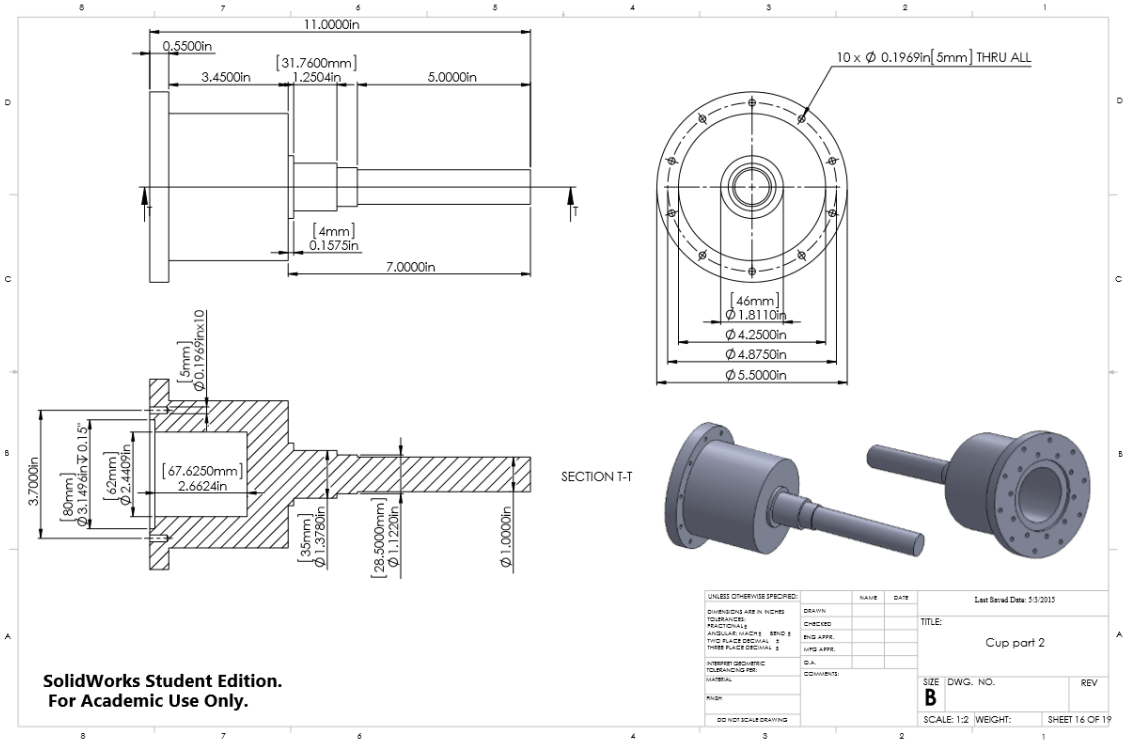
11.0000in
0.5500in
3.4500in
[31.7600mm]
1.2504in
5.0000in
[4mm]
0.1575in
7.0000in
T
10 x Ø 0.1969in[5mm] THRU ALL
[46mm]
Ø1.8110in
Ø4.2500in
Ø4.8750in
Ø5.5000in
[5mm]
Ø0.1969in×10
3.7000in
[80mm]
Ø3.1496in∓0.15"
[62mm]
Ø2.4409in
[67.6250mm]
2.6624in
[35mm]
Ø1.3780in
[28.5000mm]
Ø1.1220in
Ø1.0000in
SECTION T-T
SolidWorks Student Edition.
For Academic Use Only.
Last Saved Date: 5/3/2015
TITLE:
Cup part 2
SIZE
B
DWG. NO.
REV
SCALE: 1:2
WEIGHT:
SHEET 16 OF 19

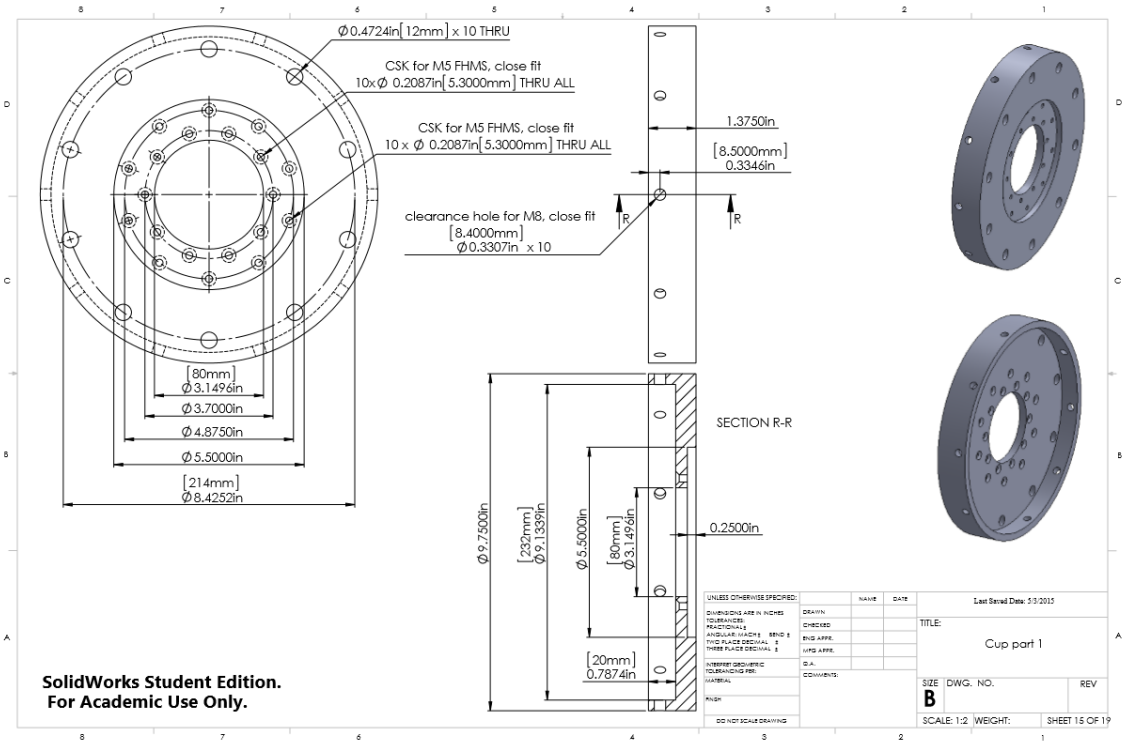
Ø0.4724in[12mm] x 10 THRU
CSK for M5 FHMS, close fit
10xØ 0.2087in[5.3000mm] THRU ALL
CSK for M5 FHMS, close fit
10 x Ø 0.2087in[5.3000mm] THRU ALL
clearance hole for M8, close fit
[8.4000mm]
Ø0.3307in x 10
1.3750in
[8.5000mm]
0.3346in
R
R
[80mm]
Ø3.1496in
Ø3.7000in
Ø4.8750in
Ø5.5000in
[214mm]
Ø8.4252in
SECTION R-R
Ø9.7500in
[232mm]
Ø9.1339in
Ø5.5000in
[80mm]
Ø3.1496in
0.2500in
[20mm]
0.7874in
SolidWorks Student Edition.
For Academic Use Only.
UNLESS OTHERWISE SPECIFIED:
DIMENSIONS ARE IN INCHES
TOLERANCES:
FRACTIONAL ±
ANGULAR: MACH ± BEND ±
TWO PLACE DECIMAL ±
THREE PLACE DECIMAL ±
INTERPRET GEOMETRIC TOLERANCING PER:
MATERIAL
FINISH
DO NOT SCALE DRAWING
NAME
DATE
DRAWN
CHECKED
ENG APPR.
MFG APPR.
Q.A.
COMMENTS:
Last Saved Date: 5/3/2015
TITLE:
Cup part 1
SIZE
DWG. NO.
REV
B
SCALE: 1:2
WEIGHT:
SHEET 16 OF 19

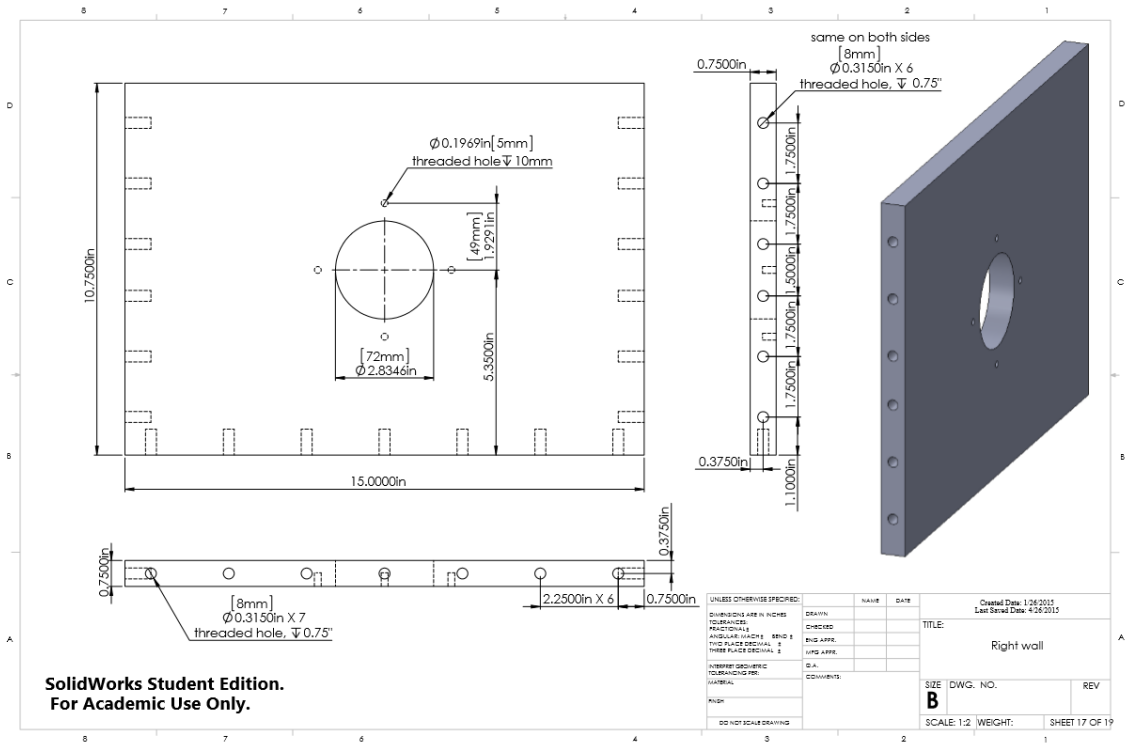
same on both sides
[8mm]
Ø0.3150in X 6
threaded hole, ↧ 0.75"
0.7500in
Ø0.1969in[5mm]
threaded hole↧10mm
[49mm]
1.9291in
10.7500in
[72mm]
Ø2.8346in
5.3500in
15.0000in
1.7500in
1.7500in
1.5000in
1.7500in
1.7500in
0.3750in
1.1000in
0.3750in
0.7500in
[8mm]
Ø0.3150in X 7
threaded hole, ↧0.75"
2.2500in X 6
0.7500in
SolidWorks Student Edition.
For Academic Use Only.
UNLESS OTHERWISE SPECIFIED:
DIMENSIONS ARE IN INCHES
TOLERANCES:
FRACTIONAL ±
ANGULAR: MACH ± BEND ±
TWO PLACE DECIMAL ±
THREE PLACE DECIMAL ±
INTERPRET GEOMETRIC TOLERANCING PER:
MATERIAL
FINISH
DO NOT SCALE DRAWING
NAME
DATE
DRAWN
CHECKED
ENG APPR.
MFG APPR.
Q.A.
COMMENTS:
Created Date: 1/26/2015
Last Saved Date: 4/26/2015
TITLE:
Right wall
SIZE
DWG. NO.
REV
B
SCALE: 1:2
WEIGHT:
SHEET 17 OF 19

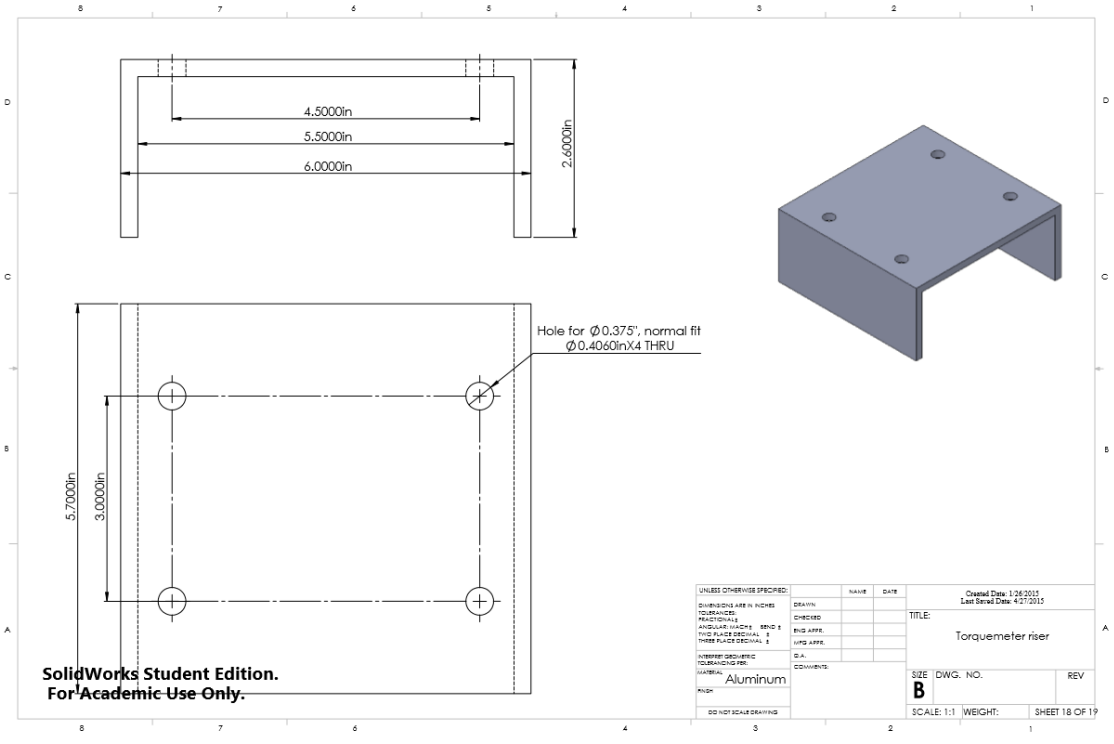
4.5000in
5.5000in
6.0000in
2.6000in
Hole for Ø0.375", normal fit
Ø0.4060inX4 THRU
5.7000in
3.0000in
SolidWorks Student Edition.
For Academic Use Only.
Created Date: 1/26/2015
Last Saved Date: 4/27/2015
TITLE:
Torquemeter riser
Aluminum
SIZE B
DWG. NO.
REV
SCALE: 1:1
WEIGHT:
SHEET 18 OF 19

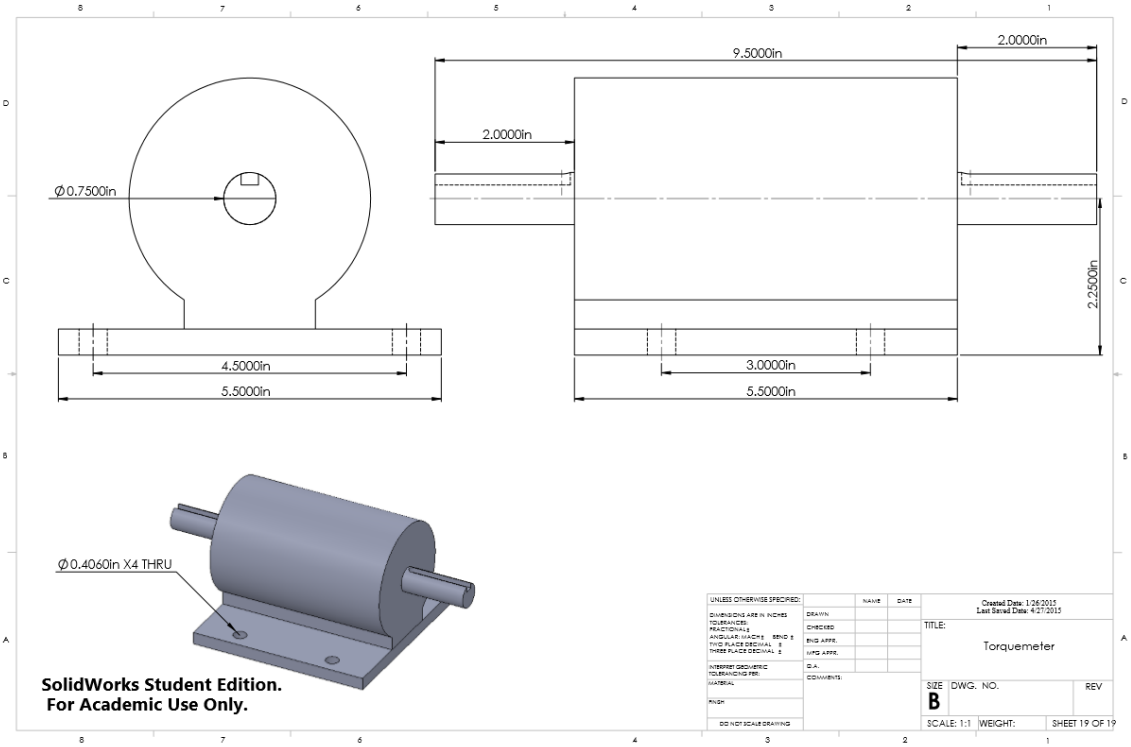
9.5000in
2.0000in
2.0000in
Ø0.7500in
2.2500in
4.5000in
5.5000in
3.0000in
5.5000in
Ø0.4060in X4 THRU
SolidWorks Student Edition.
For Academic Use Only.
Created Date: 1/26/2015
Last Saved Date: 4/27/2015
TITLE:
Torquemeter
SIZE B
DWG. NO.
REV
SCALE: 1:1
WEIGHT:
SHEET 19 OF 19